

NASA TECHNICAL NOTE

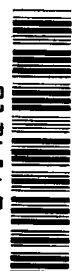


NASA IN D-8469 *2.1*

NASA TN D-8469

LOAN COPY: RET
AFWL TECHNICAL
KIRTLAND AFB,

0134142



TECH LIBRARY KAFB, NM

GEOLOGICAL APPLICATIONS OF NIMBUS RADIATION DATA IN THE MIDDLE EAST

Lewis J. Allison

*Goddard Space Flight Center
Greenbelt, Md. 20771*



0134142

1. Report No. TND-8469		2. Government Accession No.		3. Recipient's Catalog No.	
4. Title and Subtitle Geological Applications of Nimbus Radiation Data in the Middle East		5. Report Date April 1977		6. Performing Organization Code 901	
		8. Performing Organization Report No. G7702-F6		10. Work Unit No. 175-50-40	
7. Author(s) Lewis J. Allison		9. Performing Organization Name and Address Goddard Space Flight Center Greenbelt, Maryland 20771		11. Contract or Grant No.	
12. Sponsoring Agency Name and Address National Aeronautics and Space Administration Washington, D.C. 20546		13. Type of Report and Period Covered Technical Note			
		14. Sponsoring Agency Code			
15. Supplementary Notes					
16. Abstract Large plateaus of Eocene limestone and exposed limestone escarpments, in Egypt and Saudi Arabia, respectively, were indicated by cool brightness temperatures (T_B) (< 240 to 265 K) recorded by the Nimbus-5 electrically scanning microwave radiometer (ESMR), over a 2-year period. Nubian sandstone, desert eolian sand, and igneous-metamorphic rock of the Pliocene, Miocene, Oligocene, and Cretaceous periods were differentiated from these limestone areas by warm T_B values (> 265 to 300 K). These brightness temperature differences are a result of seasonal in-situ ground temperatures and differential emissivity of limestone (0.7) and sand, sandstone and granite (0.9), whose dielectric constants are (6 to 8.9) and (2.9 and 4.2 to 5.3), respectively, at 19.35 GHz. Cool T_B values in the form of a "V" were found oriented N/S over broad areas of the Nile Valley, southward to Lake Nasser and NW/SE from the Kharga Oasis to the Baharia Oasis in the Western Desert of central Egypt. Surface moisture from subsurface leakage from the Aswan Dam and the Western Desert oases could be a secondary cause for this T_B value drop. Similar cool T_B values were shown over limestone-dolomitic hills of the Interior Homocline and the Hadramawt Plateau of Saudi Arabia. Nimbus-5 and -6 ESMR T_B values selectively identified intermediate, dense rock types (limestone versus sandstone/granite) in the Lake Nasser region whose thermal inertia ranged from 0.035 to $0.06 \text{ cal cm}^{-2} \text{ C}^\circ \text{ sec}^{-1/2}$. Space albedo was determined from spatially averaged (1-km resolution) Landsat-1, MSS-7 (0.8 to $1.1 \mu\text{m}$) data, and day-night ground brightness temperature differences from Nimbus-5 temperature-humidity infrared radiometer (THIR) $11 \mu\text{m}$ data (9-km resolution) under clear sky conditions.					
17. Key Words (Selected by Author(s)) Geological research, Middle Eastern deserts, Nimbus satellite applications, Water resources, Ground radiation characteristics			18. Distribution Statement Unclassified—Unlimited		
19. Security Classif. (of this report) Unclassified	20. Security Classif. (of this page) Unclassified	21. No. of Pages 79	22. Price* \$5.00		

This document makes use of international metric units according to the Systems International d'Unites (SI). In certain cases, utility requires the retention of other systems of units in addition to the SI units. The conventional units stated in parentheses following the computed SI equivalents are the basis of the measurements and calculations reported.

CONTENTS

	<i>Page</i>
ABSTRACT.	i
INTRODUCTION	1
ELECTRICALLY SCANNING MICROWAVE RADIOMETER (ESMR)	1
TEMPERATURE - HUMIDITY INFRARED RADIOMETER (THIR).	2
CASE STUDIES	3
Eygpt	3
Saudi Arabia	10
CONCLUSION	12
ACKNOWLEDGMENTS	12
REFERENCES	75

GEOLOGICAL APPLICATIONS OF NIMBUS RADIATION DATA IN THE MIDDLE EAST

Lewis J. Allison
Goddard Space Flight Center
Greenbelt, Maryland

INTRODUCTION

Early television pictures of the Middle East recorded by Television Infrared Observation Satellite-1 to -5 (TIROS-1 to -5) (References 1 and 2) and geophysical observations by Nimbus-1 to -4 and Gemini-4 provided the first detailed satellite images of geological interest* (References 3 to 8). With the flight of Landsat-1 in July 1972, more sophisticated rock-type discrimination techniques were developed, using computer-enhanced images recorded in the 0.5- to 1.1- μ m region (References 9 and 10.)

The Nimbus-5 and -6 meteorological satellites, which were launched on December 12, 1972, and June 12, 1975, respectively, carried the electrically scanning microwave radiometer (ESMR) and the temperature-humidity infrared radiometer (THIR), which recorded useful complementary data.

The purpose of this document is to study the geological features of selected Middle East regions, using the combination of Nimbus-5 and -6, ESMR, and THIR primarily, with supportive data from Landsat-1, National Oceanic and Atmospheric Administration-2 and -4 (NOAA-2 and -4), U.S. Air Force Defense Meteorological Satellite Program (DMSP) images, and U.S. Geological Survey (USGS) geological charts and reports. The following sections contain a brief description of the two radiometers used in this study.

ELECTRICALLY SCANNING MICROWAVE RADIOMETER (ESMR)

The Nimbus-5 and -6 were flown in near-polar (81° retrograde), Sun-synchronous circular orbits of about 1100 km (600 nmi). Each orbit crossed the Equator with an approximate 27° longitude separation and a period of 107 minutes (References 11 and 12). The basic physics behind the Nimbus-5 and -6 ESMR are the same, although the scanning geometry and operating wavelengths are different.

*J. Pouquet, *Geopedological Features Derived from Satellite Measurements in the 3.4 to 4.2 and 0.7 to 1.3 μ Spectral Regions*, NASA/GSFC X-622-69-437, 1969, p. 27.

The Nimbus-5 ESMR measures the Earth and atmospheric radiation in a 250-MHz band centered at 19.35 GHz (1.55 cm), with a noise equivalent temperature difference (NE Δ T) of approximately 2 K (figure 1a). It scans the Earth every 4 seconds from 50° to the left through nadir to 50° to the right in 78 steps with some overlap. The scanning process is controlled by an onboard computer and scans a region approximately 30° of longitude wide at 30°N. The half-power beamwidth of the antenna is 1.4° or 22 km at nadir, and 2.2° or 45 by 160 km at the 50°nadir angle edges. The instrument is discussed in References 13 through 17.

The Nimbus-6 ESMR receives thermal radiation from the Earth in a 250-MHz band centered at 37 GHz (0.81 cm) (figure 1b). Each electrically scanned sweep records brightness temperatures at 71 steps over a 5.3-second period and scans a region approximately 13° of longitude wide at 30° N. The antenna beam scans ahead of the spacecraft along a conical surface with a constant 45° angle with respect to the antenna axis, and delineates a 15° to 30° by 60-km field of view at the Earth's surface with an NE Δ T of 1 K. The Nimbus-5 ESMR measures only the horizontally polarized component and the Nimbus-6 ESMR measures the horizontal and vertical components by using two radiometer channels. A full description of this instrument has been discussed in Reference 18.

The microwave brightness temperature (T_b) of the Earth's surface is mainly affected by surface emissivity and temperature, atmospheric water vapor, and liquid water droplets. Cloud ice crystals (cirrus) have little effect on microwave radiation and are essentially transparent at the Nimbus wavelengths. Molecular oxygen absorption can also be neglected (References 19 and 20). The emissivity of the surface may vary due to the change in dielectric constant. Since the dielectric constant of water can be 80 and dry soil as low as 3 to 5, water content of soil can have a strong effect at microwave frequencies (References 21 to 23). The resulting soil emissivity can vary from 0.5 (wet) to 0.9 (dry) (Reference 24). The emissivity of nonvegetating surfaces can vary from 0.85 to > 0.95 and, depending on the soil moisture content, the occurrence of dew, the surface temperature, and receiver polarization, can indicate microwave brightness temperatures between 205 to > 310 K. Surface microwave radiation can be affected by roughness, topographic slope, stratigraphy (layering of different materials), density of rocks, vegetation cover, receiver wavelengths, and angle of incidence observed (References 25 to 27). Ocean surfaces have a low emissivity of approximately 0.40 and a resulting cold microwave brightness temperature of 120 to 170 K (horizontal polarization), and 190 to 220 K (vertical polarization).

TEMPERATURE-HUMIDITY INFRARED RADIOMETER (THIR)

The Nimbus-5 and -6 satellites carried the THIR, a two-channel radiometer which had proven its reliable performance by recording several years of day-night data indicating cloud heights and ground and sea temperature, and providing a qualitative estimate of mid-tropospheric humidity under clear sky conditions (Reference 15).

The two THIR detectors consist of germanium-immersed thermistor bolometers which have peak spectral responses in the 10.5- to 12.5- μ m "window" region and the 6.3- to 7.25- μ m water vapor absorption region (figure 2). A cutaway of the radiometer, shown

in figure 3, includes the scan mirror, a Sun shield, a 5-inch folded optical Cassegranian telescope, a dichroic beam splitter, an electronics module, and two detectors.

The elliptically-shaped plane scan mirror, inclined at 45° to the optical axis of the instrument, rotates at 48 rpm and scans through a 360° angle in the plane perpendicular to the direction of motion of the satellite. Figure 4 shows the 7.7- by 7.7-km (4.1- by 4.1-nmi) ground resolution (scan spot) of the $11\text{-}\mu\text{m}$ channel at zero degree nadir increasing to an elongated 14- by 31.8-km scan spot at 50° nadir, at an 1112-km (600-nmi) orbital altitude. Similarly, the ground resolution of the $6.7\text{-}\mu\text{m}$ channel at the subsatellite point was 22.6 km, while at 50° nadir it was 41.1 km by 93.5 km.

A sample Nimbus-5 THIR ($11\text{-}\mu\text{m}$) scan sequence is shown in figure 5. The two detectors simultaneously view the housing; A at spacecraft zenith, (zero seconds). Seven synchronous pulses start at C, followed by six 1-volt calibration steps. A space scan starts at D to G, followed by an Earth scan (117° wide) to I, a space scan to K, a housing scan to M, and then back to zenith. The entire sequence lasts 1.23 seconds. The space and housing-viewed parts of the scan serve as part of the inflight check of calibration. Note the small noise ripple on the housing and space scans (Reference 28). The NE Δ T for the $11\text{-}\mu\text{m}$ channel is approximately 1.5 K at 185 K and 0.28 K at 300 K. Corrections of 2 to 7 K must be added for losses due to atmospheric water vapor. A correction of < 1 K may be disregarded for extremely dry desert atmospheres, which was the case in this study.

CASE STUDIES

Two areas of the Middle East were examined using the Nimbus-5 and -6 ESMR and THIR data in order to explain the recurrence of distinctive cool microwave surface brightness patterns, on successive cloud-free days and nights over a 2-year period.

Egypt

A light gray "V" structure was noted in the Nimbus-6 ESMR pictures in the region of north-central Egypt (figure 6). A computer-produced grid print map (1:2 million, Mercator) of this scene (figure 7) shows cool brightness values of < 240 to 265 K overlaying the Nile Valley and Lake Nasser, and extending northwestward along a line of known oases in the Western Desert. A review of all Nimbus-5 and -6 ESMR pictures over Egypt was made from December 1972 to June 1976. This "V" structure appeared consistently in the imagery both day and night under cloud-free conditions. Two geological maps of Egypt (figures 8 and 9) delineate the Eocene limestone (Reference 29) and Nubian sandstone (Reference 30). These rock formations, together with large sand areas in the Western Desert and igneous-metamorphic rock formations along the Red Sea, outline and coincide with the "V" structure shown in figures 6 and 7. A more detailed geological analysis of the Nile Valley in the Aswan Dam area was made from Landsat-1 data by El Shazly et al. (References 31 and 32), who confirmed the limestone, sandstone, and granitic deposits.

Since surface and subsurface soil moisture can lower microwave brightness temperatures in the salt deserts (Reference 33), a literature search was made of Egypt to find some evidence of subsurface water seepage from prominent surface water systems, such as the Nile or Lake Nasser.

Figures 10a through d show the preflood and flood stage of the Lake Nasser Reservoir in 1969 on Nimbus-3 and Landsat-2 images, respectively. A New York Times article (Reference 34) reported that Lake Nasser had been filling up more slowly than expected since 1969, and that only 5 to 6 of 12 available hydroelectric turbines were being utilized in the Aswan Dam due to the lack of water storage. Drs. Farouk El Baz and Abdel-Hady* confirmed the possibility that underground water seepage could occur in the extensive Egyptian limestone and sandstone deposits in the Lake Nasser and Nile Valley region. Surface drilling was attempted in 1976 in Egypt to measure the extent of water loss.

Microwave Physics Relationships

Previous field work by Edgerton and Trexler (Reference 35), Kennedy et al. (Reference 36), and later by Edgerton et al. (Reference 37), using truck-mounted microwave-sensing equipment (figure 11), showed that limestone had a low computed and measured brightness temperature (high dielectric constant) when compared with other minerals of lower dielectric constants (high brightness values) (figure 12). Note that the emissivity decreases more rapidly for the Brewster angle ($> 60^\circ$), resulting in a drop in brightness values. The dielectric constant of a material is defined as the ratio of the capacitance of a condenser filled with the material to the capacity of the condenser when a vacuum exists between its plates (Reference 25).

The dielectric constants of selected solid rocks measured at 35 GHz can range from 2 to 10 (References 38 to 40). Tables 1, 2, and 3 contain a partial list of the physical characteristics of ground materials relevant to this study (References 35, 38, and 41 to 43).

The physical constants in the tables which appear to be similar are enclosed by a bracket. The use of thermal inertia mapping to discriminate geological units in the United States and Oman indicated that limestone, dolomite, sandstone, and granite fall into a thermal inertia class interval of 0.03 to $0.06 \text{ cal cm}^{-2} \text{ }^\circ\text{C}^{-1} \text{ sec}^{-1/2}$ (References 43 to 47). Any microwave radiation technique which could more selectively identify any of these minerals within this class interval would be of value† (Reference 50).

The following parameters affect the Nimbus-5 ESMR (19.35 GHz) brightness values (T_B) of a smooth desert surface‡ (Reference 48).

$$\hat{T}_B = \tau [\epsilon T_g + (1 - \epsilon) T_d] + T_u$$

*Private communication, 1975.

†H. A. Pohn, private communication, 1976.

‡F. T. Ulaby, private communication, 1975.

where:

τ = atmospheric transmittance

ϵ = emissivity

T_g = ground temperature, K

T_d = downward emitted atmospheric temperature, K

T_u = upward emitted atmospheric temperature, K

For two fields of view with different emissivities, but the same ground temperature, the difference in T_B is:

$$\Delta T_B = \tau (T_g - T_d) (\epsilon_2 - \epsilon_1)$$

For a dry desert atmosphere, a ground temperature of 310 K, $\tau \approx 0.95$, and $T_d \approx 10$ K, the emissivity is:

$$\epsilon = 1 - \left(\frac{\sqrt{K} - 1}{\sqrt{K} + 1} \right)^2$$

where:

K = dielectric constant

Thus:

	Limestone	Sand
Dielectric constant:	8.4	2.9
Emissivity:	0.763	0.932

These emissivities give:

Sand: $T_B = 285$ K

Limestone: $T_B = 237$ K

$\Delta T_B = 48$ K

The effect of roughness is minimal for a high emissivity material such as sand, but roughness in limestone, a lower emissivity material, may warm the T_B by 20 K or more at 19.35 GHz.

From the basic thermodynamic relationship:

$$\text{Emissivity} = 1 - \text{Reflectivity}$$

The reflectivity of a rough surface is smaller than a smooth surface since multiple reflections tend to reduce the total amount of incident radiation reflected. Therefore, the emissivity

Table 1
Selected Physical Characteristics of Ground Materials

Surface Materials	Dielectric Constant (Real Part)	Emissivity (at 37 GHz)	Density (gm cm ⁻³)	Porosity (%)
Desert Sand (quartz, dry; medium fine)	2.9	0.93	1.4 to 1.93	39 to 46
Sandstone	4.2 to 4.8	0.93	2.2 to 2.7	0.7 to 20
Granite	4 to 5.3	0.90	2.5 to 2.8	0
Limestone	6 to 8.9	0.75	2.65 to 2.8	0.5 to 5

Table 2
Thermal Characteristics of Ground Materials

Surface Materials	Thermal Inertia (cal cm ⁻² °C sec ^{-½})	Thermal Conductivity (cal cm ⁻¹ sec ⁻¹ °C ⁻¹)
Desert Sand	0.01 to 0.02	0.00063
Sandstone	0.030 to 0.058	0.0062
Granite	0.036 to 0.066	0.0065
Limestone	0.04 to 0.06	0.0048

Table 3
Thermal Characteristics of Ground Materials

Surface Materials	Thermal Diffusivity (cm ² sec ⁻¹)	Volumetric Heat Capacity (cal cm ⁻³ °C ⁻¹)
Desert Sand	0.0020	0.314
Sandstone	0.0113	0.546
Granite	0.0127	0.511
Limestone	0.0081	0.594

is greater and the T_B value warmer. Conversely, high soil moisture content can cause an increase in dielectric constant, which results in higher reflectivity or lower emissivity, causing the T_B to decrease. A 1-percent change in soil moisture content can result in a 4-K change in brightness temperature (Reference 37).

Nile Delta—Nile River Valley

An excellent cloud-free, visible picture (0.5 to 0.7 μm) of the Nile Valley was taken on October 23, 1974, by NOAA-2 very high resolution radiometer (VHRR) (1-km ground resolution) (figure 13). The darker heart-shaped region to the southwest of the present Nile Delta is labeled the "Old Nile Delta." According to a hypothesis of the "Urnil", this area (Reference 49) was the region where the Nile River exited to the Mediterranean Sea at 29°E, southwest of Alexandria, and may have produced an "old" delta, which consists of fluvial and fluvio-marine sediments deposited during the lower and middle Miocene periods. This sand and shale region, which logically could have moved eastward, according to current theory, to the present delta location, appears warmer in all the Nimbus-5 and -6 ESMR analyses, to be discussed later. Figures 14, 15, and 16, which cover the Nile Delta, show an Operational Navigation Chart (ONC) H-5, 1:1 million base map for reader reference, a NOAA-4, VHRR (10.5- to 12.5- μm) (1-km resolution) day, unrectified thermal IR map of June 28, 1975, and a typical Landsat-1, band 7 (0.8- to 1.1- μm) (80-meter resolution) picture of the region. The irrigated farmland in the delta, which extends from Port Said westward to Rosetta and southward to Cairo, appears 4 to 8 K cooler in the IR (figure 15) than the nearby desert sand. A wedge of cooler T_B values, indicating high soil moisture in the delta, is also shown on Nimbus-5 THIR (11- μm) day, on July 16, 1974 (figure 17). The Red Sea hills and mountains of Jordan and Saudi Arabia are generally the warmest (> 315 K), followed by large portions of the Western Desert (310 to 315 K) and the coastal strip and Nile Valley (< 310 K). The water-land interface shows up well in the daytime, but there is little coastal, hill, or low-land definition at night (293 to 303 K) (figure 18).

Thermal Inertia Relationships

The thermal inertia of a material is determined by its volumetric heat capacity, thermal conductivity, thermal diffusivity, specific heat, and density. Figure 19 shows the variations of surface temperature as a function of thermal inertia. Optimum surface heating and cooling occurs at 1:30 p.m. and 2:30 a.m. The temperature variations are caused by atmospheric cooling and heating at 35°N, heat loss by thermal emission, and heat gain by solar energy absorption (References 44 and 50). The greater the diurnal surface temperature variation of a material, the smaller the inferred thermal inertia, and, conversely, the smaller the temperature variation, the larger the thermal inertia.*†

A previous study (Reference 43) used Nimbus-3 high resolution infrared radiometer (HIRR) (0.8- to 1.1- μm) daytime data for measuring surface reflectivity and Nimbus-4 THIR (11- μm)

*J. Shutt, *An Approach to Thermal Property and Temperature Determination from Spacecraft*, NASA/GSFC X-923-75-84, 1975, p. 31.

†J. Price, *Thermal Inertia Mapping, a New View of the Earth*, NASA/GSFC X-913-76-121, 1976, p. 38.

data for day-night temperature differences to derive a thermal inertia map of geological units in Oman. A similar visible band (MSS-7, 0.8 to 1.1 μm) from Landsat-1, on November 9, 1972, was used in this study to obtain space albedo over the Lake Nasser region and Nimbus-5 THIR for day-night differences. The Landsat-1 80-m resolution elements were averaged to 1-km elements in order to permit comparison with the larger scan spots covered by the THIR data.

Space reflectivity (R_7), from MSS-7 on Landsat-1, was derived as follows (Reference 51):

$$R_7 = \frac{\pi N_7}{S_7 \cos \theta_o}$$

$$R_7(\%) = 1.3795 \times C_7$$

where:

- N_7 = nadir radiance
- S_7 = solar constant for MSS-7
- θ_o = Sun zenith angle
- C_7 = Landsat digital count for MSS-7

A 1-km element represents an average of 16 columns and 12 rows of the full resolution (80-m) Landsat digital data printout.

Figures 20a and 20b show the Landsat-1 MSS-7 image and the 1-km averaged Cal-Comp line-drawn analysis for November 9, 1972, respectively. Large limestone areas indicated by space reflectivities of 50 to 65 percent are shown to the left of column 1600 (top), and the Nubian sandstone (graystone) and granite areas are 35 to 45 percent and < 35 percent, respectively. Figures 21 and 22 are included to show the large limestone units described by El Shazly et al. (Reference 31) for the same Landsat picture. Otterman and Frazer (Reference 51) had reported space reflectivities of 54 to 57 percent for Libyan desert sand from Landsat-2 MSS-7. A laboratory spectrographic analysis of Sinai desert sand indicated 49 to 54 percent total diffusive reflectances for this wavelength (figure 23), which makes the above space reflectivities more credible.

Day-night temperature differences for July 16, 1974, were obtained using Nimbus-5 (11- μm) data under clear sky conditions (figure 24). A radiosonde run at Aswan, Egypt, on July 16, 1974, 1200 Greenwich mean time (GMT) (figure 25) indicated a dry atmosphere; therefore, no atmospheric corrections were made to the 11- μm analyses. The southern Sinai Peninsula, the Red Sea hills, the mountains of Jordan and Saudi Arabia, and portions of the Western Desert show the largest diurnal temperature difference (20 to 35 K), and the limestone deposits in the Nile Valley and coastal deserts indicate 5 to 20 K. The Red Sea, Mediterranean Sea, and Nile Delta show a smaller ΔT_B of 3 and 5 to 10 K, respectively.

Pohn et al. (Reference 43) developed a least-square fit of thermal inertia versus day-night temperature difference for different albedos (figure 26). By overlaying a portion of the day-night temperature difference chart (figure 24) on the reflectivity chart of the Lake Nasser region (figure 20), the range of thermal inertia ($\text{cal cm}^{-2} \text{ }^{\circ}\text{C sec}^{-1/2}$) shown in table 4 was derived.

Table 4
Thermal Inertia Relationships

	Space Reflectivity (%)	Day-night 11- μm T_B differences (K)	Thermal Inertia
Granite	20 to 35	20 to 25	0.038 to 0.058
Sandstone	35 to 45	16 to 20	0.040 to 0.060
Limestone	50 to 65	12 to 16	0.035 to 0.058

The thermal inertia values for the three materials above range from 0.035 to 0.060 $\text{cal cm}^{-2} \text{ }^{\circ}\text{C sec}^{-1/2}$, which is in agreement with published values in the literature, as shown in table 2. The use of microwave data to further differentiate these materials will be discussed in the next section.

Microwave and Infrared Brightness Temperature Relationships

In order to compare the Nimbus-5 ESMR (19.35-GHz) and THIR (11- μm) brightness temperatures, four cross sections (box 1, 2, 3, and 4) were drawn through the area of interest (figures 27, 28, and 29). Coincidental data was used for the night of July 16, 1974, but a 10-day separation occurred for the day comparison (July 16 to July 25, 1974) due to satellite instrument processing problems.

Individual Landsat-1 and -2 frames with box-area limits in black are shown for ready reference of geological formations (figures 30, 31, 34, 37, and 40).

Averages of IR and ESMR brightness values were plotted within a half degree of latitude from 24°N in the four regions to 29°30', using the respective Nimbus grid print map (1:2 million, Mercator). The IR brightness data was uncorrected due to negligible atmospheric moisture content.

An analysis of the cross-sectional data in figures 32, 33, 35, 36, 38, 39, 41, and 42 shows the following relationships:

- The Nimbus-5 11- μm brightness values over the igneous-metamorphic rocks in the Red Sea hills and southern Sinai Peninsula were the warmest ($320 \text{ K} \pm 2 \text{ K}$) during the day, and the cooler nighttime T_B gradients appear rather flat ($296^{\circ} \pm 4^{\circ}\text{C}$) over most ground surfaces.

- The Nimbus-5 ESMR 19.35-GHz brightness values were warmest (270 to 282 K, day; 260 to 265 K, night) over the igneous-metamorphic rocks and sandstone, and coolest (250 to 263 K day; 240 to 251 K, night) over limestone. The average day or night difference between the above materials was approximately 15 to 30 K.
- The THIR-ESMR brightness difference is largest for the Red Sea (> 100 K), followed by limestone (48 to 52 K, day; 42 to 45 K, night), igneous-metamorphic rocks (38 to 47 K, day; 26 to 40 K, night), and sandstone (35 to 41 K, day; 28 to 37 K, night). A second areal average of THIR-ESMR brightness temperature difference between limestone and igneous-metamorphic rocks and sandstone was 14 K, night and 10 K, day. Sandstone and igneous-metamorphic rocks are similar in dielectric constants, density, and thermal inertia, but have different porosity and surface roughness (tables 1 and 2).

Nimbus-6 ESMR (37-GHz) data were also analyzed for selected days in July and August 1975. The dotted "V" structure in the horizontal polarization data of July 28, 1975 (figure 43) appears cooler (T_B : < 250 to 260 K), and the sandstone and igneous-metamorphic rocks are warmer (T_B : 270 to > 300 K). The cool "V" structure in the vertical polarization data appears to be < 280 to 290 , and the sandstone and granitic hilly areas are warmer: 300 to 318 K (figure 44). When horizontal polarization data are subtracted from the vertical polarization data of August 14, 1975, large 70- to 80-K T_B differences occur over the sea, and 40- to 50-K T_B differences occur in the Western Desert and the An Nafud Desert (figure 45). These differences may have been caused by scattering from smooth sand-dune surfaces which have scattering characteristics similar to those of the 10° to 15° slope of a "low-wind" sea surface.* A similar effect was noted in the sands of the Rub Al Khali Desert (Empty Quarter) of southern Saudi Arabia (figure 59). Smaller T_B differences (< 20 K) appear in the hilly regions bordering the Red Sea, the Sinai Peninsula, and Israel.

Saudi Arabia

Several Nimbus-5 and -6 ESMR and THIR orbits over Saudi Arabia were selected in order to study the patterns of microwave and infrared brightness temperatures over an adjacent, cloud-free, desert-mountainous region. This area does not have an established river system flowing through it like the Nile in Egypt, which could have underground water seepage possibly changing the surface microwave emissivity patterns of the desert.

Figure 46a shows an excellent U.S. Air Force DMSP visible picture of the region (Reference 52) on February 14, 1975, and figure 46b indicates the main geological features as described by Powers et al. (Reference 53).

The Arabian Shield consists mainly of igneous and metamorphic rocks which have been tectonically stable since the Precambrian period and are locally overlain by Cenozoic volcanics, Quaternary alluvial, and Eolian sediments (dark and light tones) (Reference 54).

*W. H. Peake, private communication, 1975.

The Interior Homocline falls away from the shield (figure 47) and consists of eroded limestone, dolomite, shale, and sandstone, which appear in a stripe pattern in the central Arabian arch area. Extensive low-lying wind-blown Eolian sands occur in the An Nafud and Rub Al Khali Deserts to the north and south, respectively. The Hadramawt Plateau along the south coast is a high, dissected plateau with a dominant east-west drainage system; make-up of limestone, shale, and marl strata. Figure 48 shows all areas containing large units of limestone obtained from the U.S. Geological Survey/Arabian American Oil Co. 1963 geologic map of the Arabian Peninsula and the U.S. Geological Survey Miscellaneous Geological Inventory Map I-270A. Note the similarity in the light-gray areas in the Interior Homocline (central portion) and south coast of Saudi Arabia in the Nimbus-5 ESMR image (figure 49) and the limestone deposits in figure 48.

Cool microwave brightness temperatures at night (240 to 260 K) on September 18, 1973, clearly outline these areas (figure 50). The Arabian Shield (granitic rock) is progressively warmer (> 260 to 270 K), and the Rub Al Khali Desert is the warmest (> 270 K). However, in a day analysis over the same area on September 24, 1973 (figure 51), a 2 to 4° of longitude-wide strip of hills in the Arabian Shield from 40°E to 45°E indicate warmer T_B values (280 to > 290 K) than those of the sands of the Rub Al Khali Desert. A similar pattern showing this temperature reversal is found on July 16, 1974, day (figure 53). A distinctively warm T_B pattern (> 270 K, night; > 280 K, day) was found over the Kuwait oilfields (Reference 55) in all Nimbus-5 ESMR analyses. This area was mixed with chalk, limestone and quartz gravel, marly sandstone, sandy marl, sandy limestone, and calcareous silty sandstone (figure 48, Reference 53). Figure 52, which shows another view of the region at night on March 8, 1975, indicates a pattern similar to figure 50, but overall ESMR brightness values are lower by 10 to 20 K due to seasonal temperature changes. Analyses of Nimbus-5 ESMR and THIR (figures 53 and 54) for July 16, 1974, day were made, on which a half-degree latitude cross section through the Arabian Shield, the Interior Homocline, and Platform was performed (figure 55). Large differences (52 to 61 K) were found between the 11- μ m and ESMR T_B values over limestone and dolomite hills, and smaller differences (38 to 43 K) were found over igneous-metamorphic rocks and sandstone. The limestone-dolomite structures in the Interior Homocline are generally 20 to 30 K cooler than the granitic rocks in the Arabian Shield and 10 to 20 K cooler than the eolian sand in the Rub Al Khali and An Nafud Desert at 19.35 GHz.

Nimbus-6 ESMR (37-GHz) vertical and horizontal polarization data for August 16, 1975 (figures 56 and 57), showed a similar night temperature pattern, as did the Nimbus-5 analyses (figures 50 and 52); i.e., the eolian sand appeared warmest in both polarizations. When horizontal was subtracted from vertical polarization data, large (40 to 60 K) T_B values were noted to be located over the sands of the Empty Quarter (figures 58 and 59). This may be caused by a surface scattering effect of the sand dunes at 37 GHz.*

*W. H. Peake, private communication.



CONCLUSION

The microwave brightness temperatures from Nimbus-5 and -6 ESMR and THIR have been used to identify large units of limestone-dolomite against a background of igneous-metamorphic rock, sandstone, and eolian sand in the Middle Eastern deserts. Nimbus-G, Seasat, and Shuttle, to be launched in the 1978 to 1981 time period, will carry multifrequency passive and infrared radiometers, which hold great promise for further geological exploration from space.

ACKNOWLEDGMENTS

The author wishes to acknowledge the assistance of Dr. Robert Frazer and Dr. O. Bahethi in processing the Landsat data and to Dr. Joseph Otterman for initiating this study over the deserts of the Middle East.

Goddard Space Flight Center
National Aeronautics and Space Administration
Greenbelt, Maryland March 1977

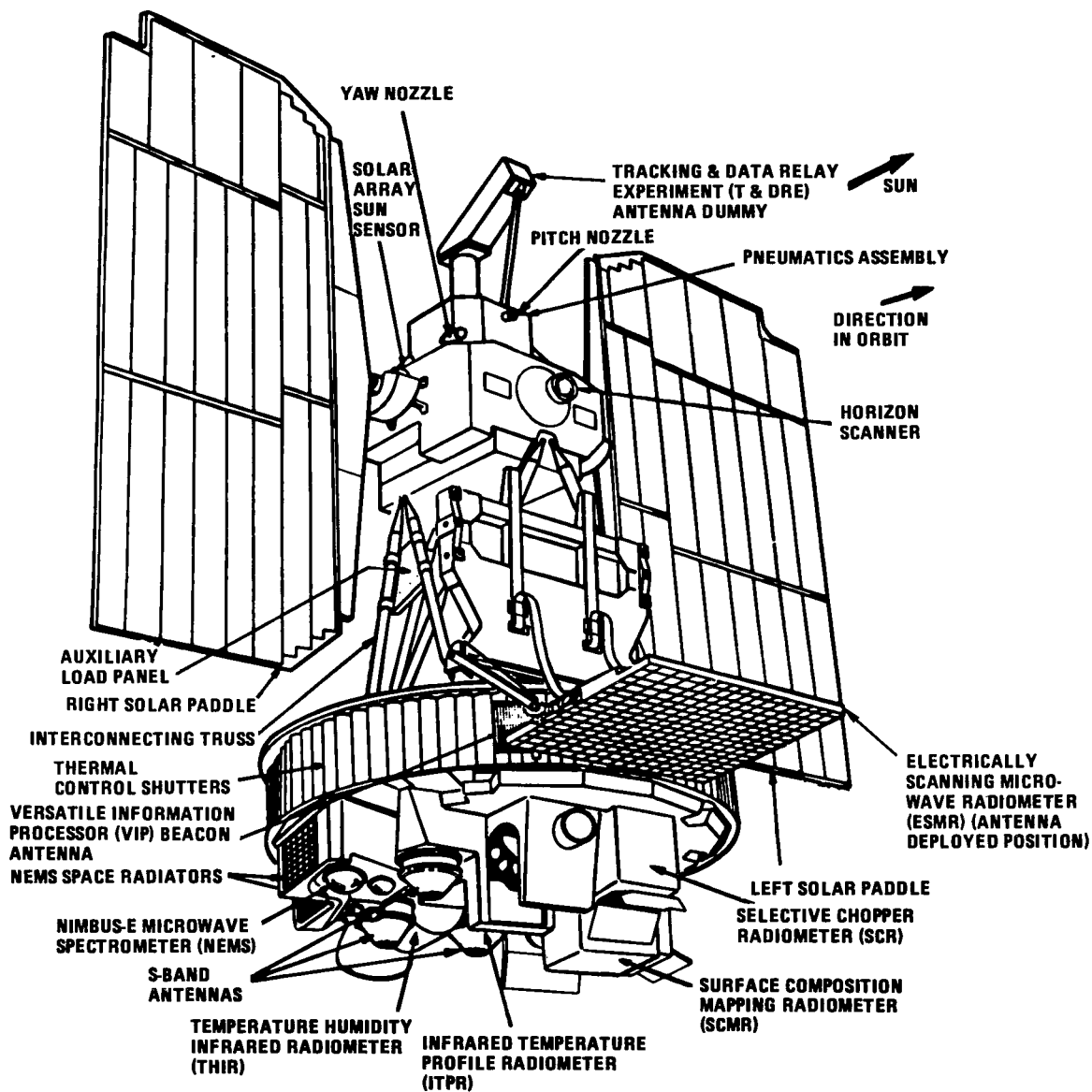


Figure 1a. Nimbus-5 spacecraft with associated experiments.

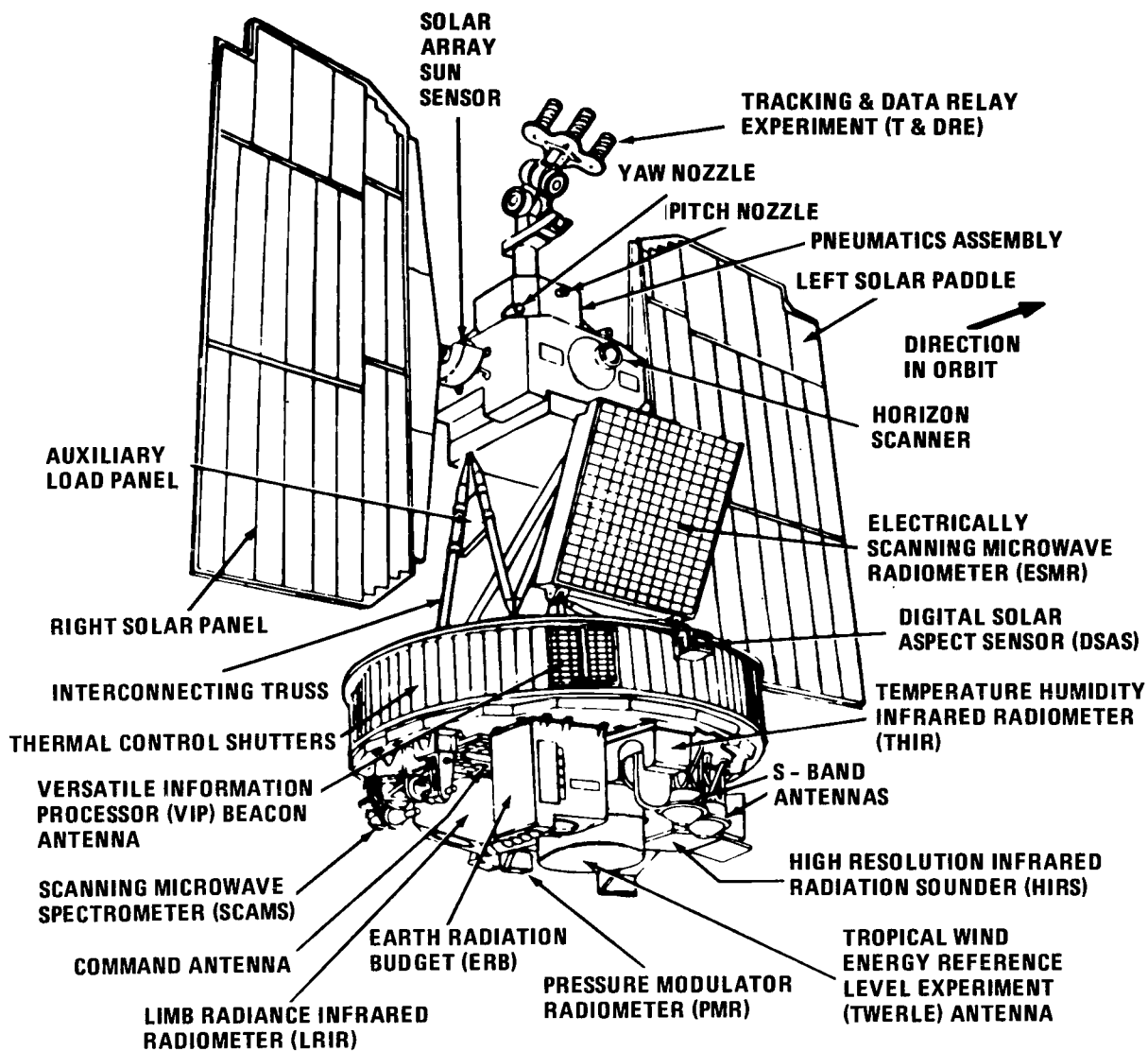


Figure 1b. Nimbus-6 spacecraft with associated experiments.

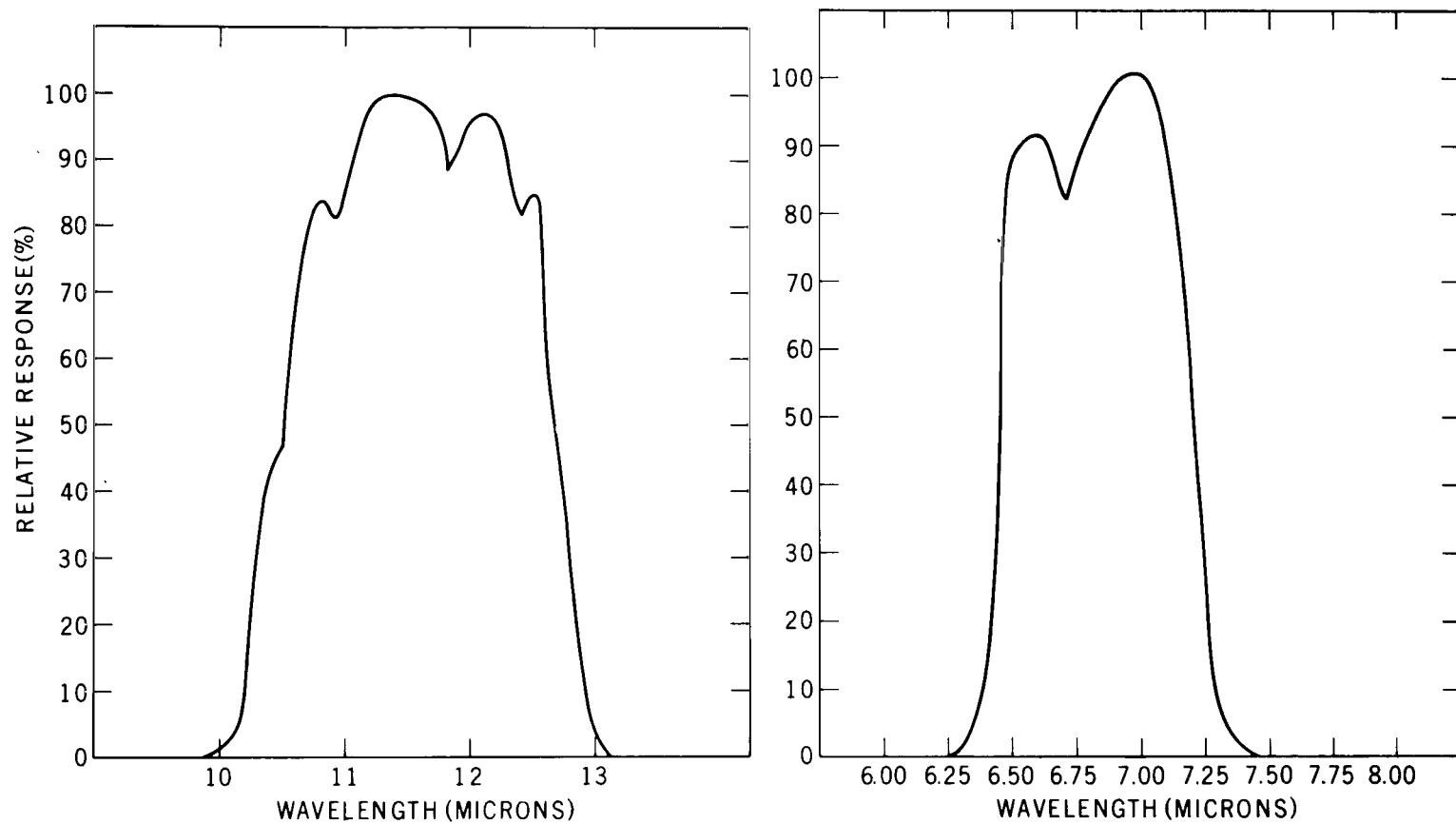


Figure 2. Relative spectral response of the 11.5-μm and 6.7-μm channel of the Nimbus-5 THIR.

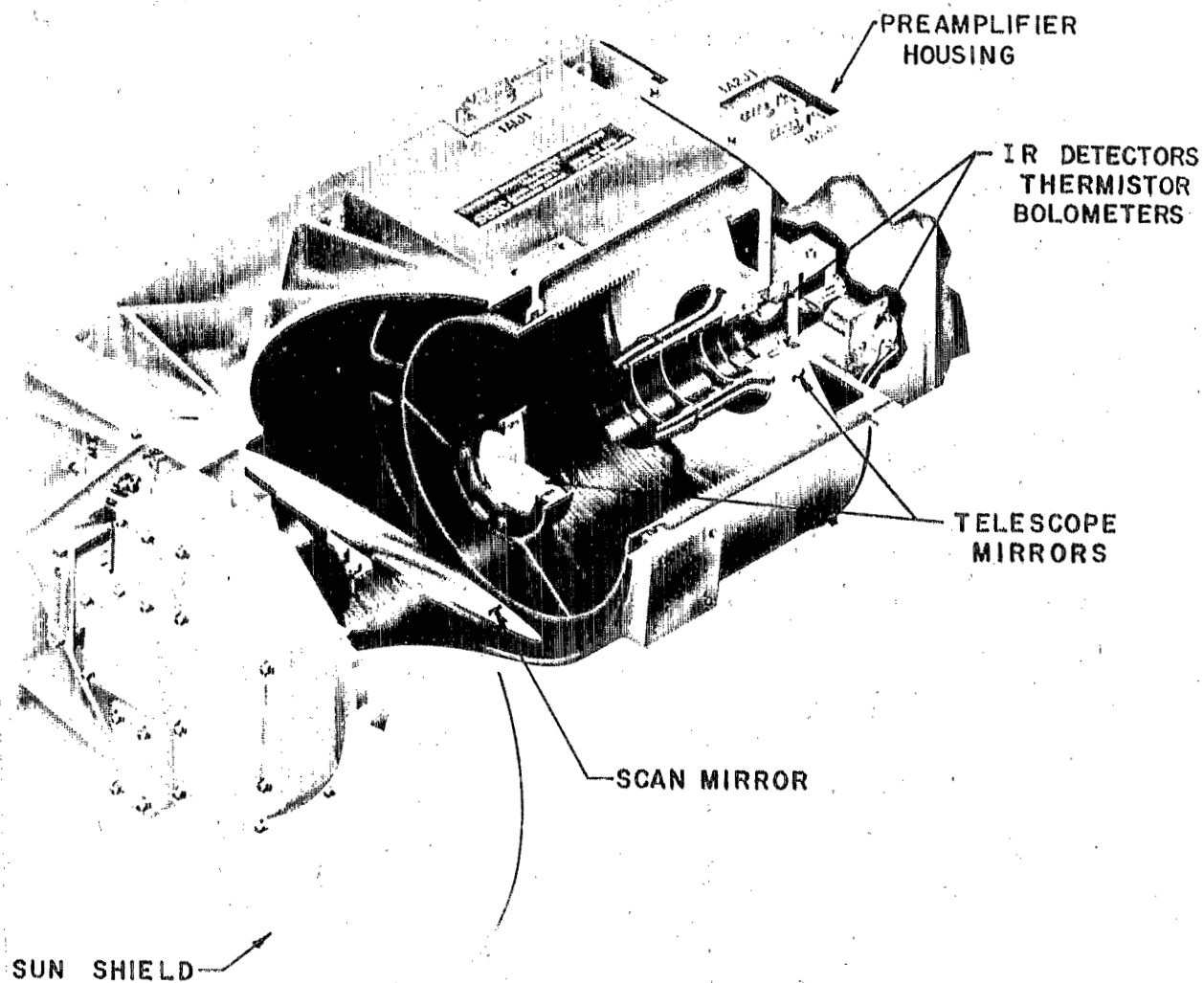


Figure 3. Cutaway of the Nimbus-5 THIR.

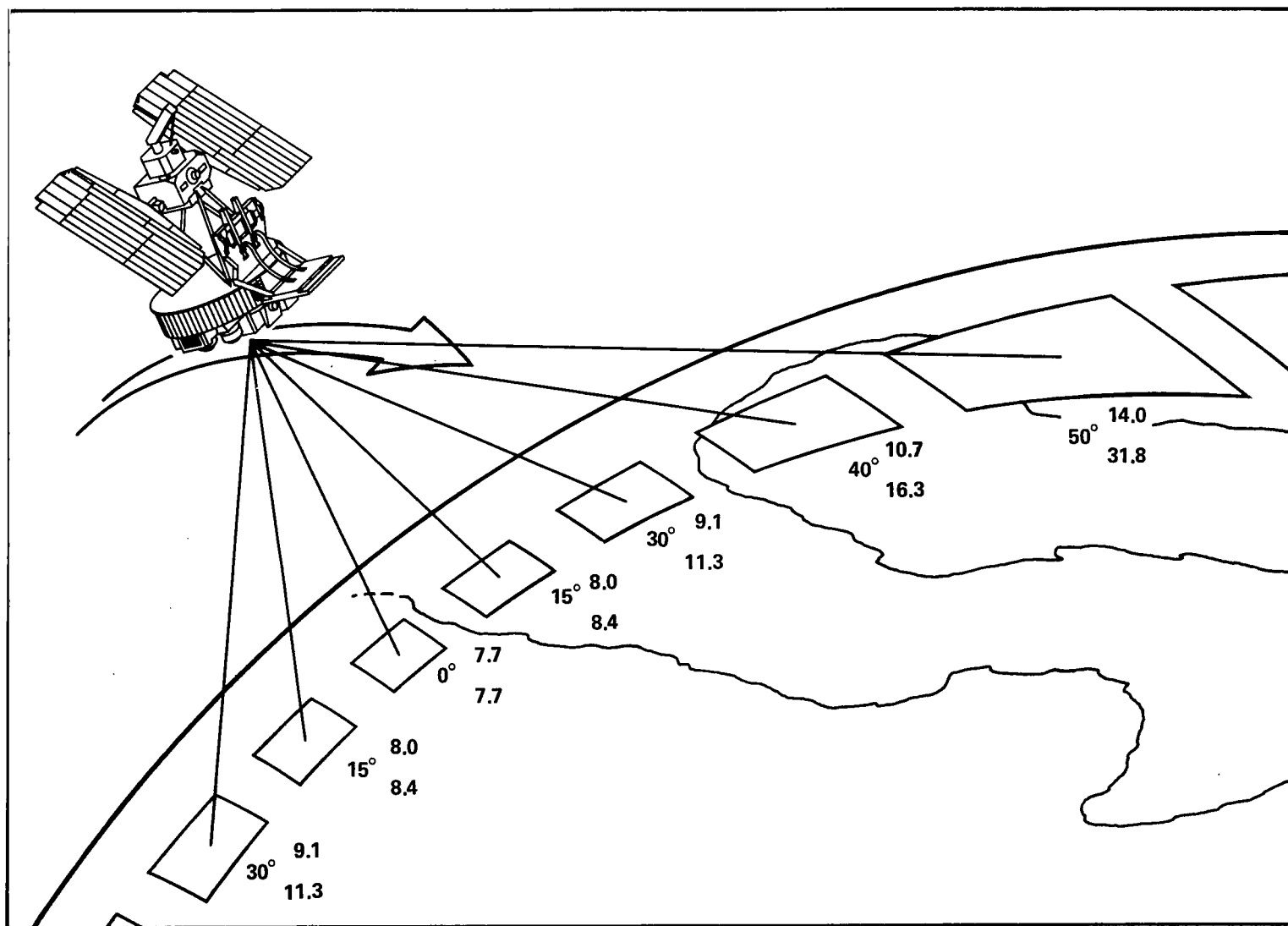
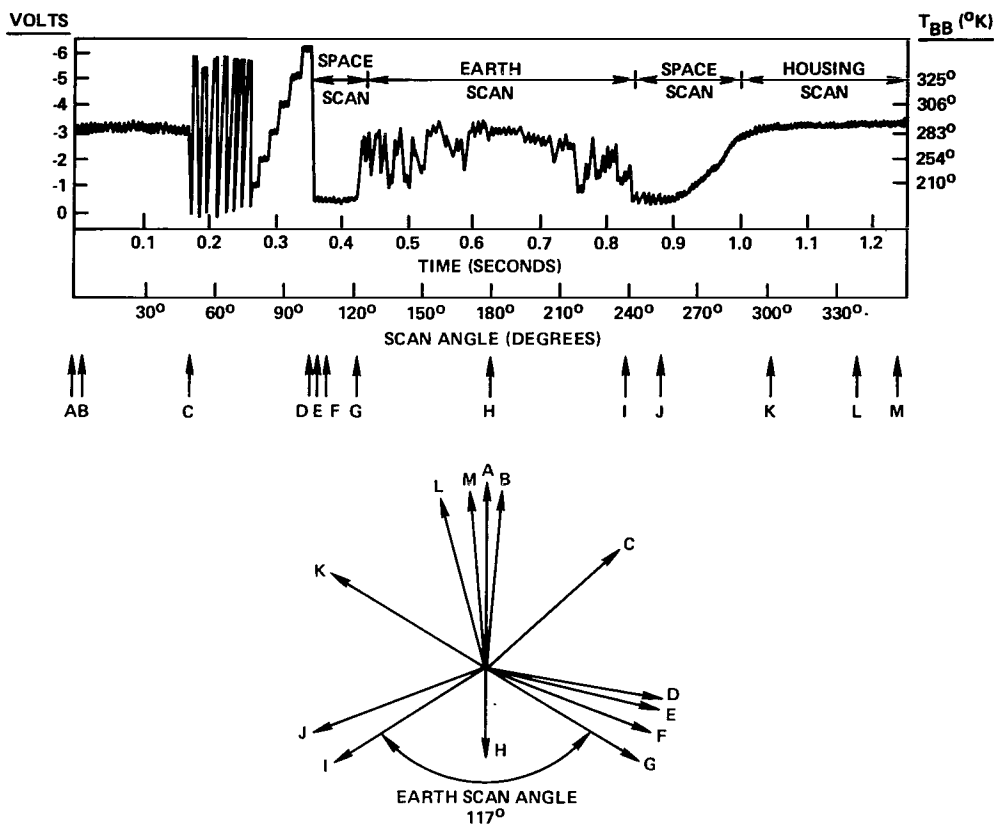


Figure 4. Scanning pattern of the Nimbus-5 THIR, 11 μ m (surface resolution in km at varied nadir angles).



LEGEND

REFERENCE LETTER	ANGLE (DEGREES)	TIME (MSEC)	EVENT
A:	0°	0	SPACECRAFT ZENITH
B:	5°	17.4	RADIOMETER IFOV JUST STARTING TO LEAVE HOUSING.
C:	48°	166.7	SCAN MIRROR POSITION PIP NO. 1 OCCURS AND RADIOMETER SYNC WORD AND CALIBRATION SIGNAL SEQUENCE IS STARTED. 6.7 MICRON CHANNEL GAIN RETURNED TO NORMAL.
D:	100°	347.5	RADIOMETER IFOV JUST STARTING TO SEE ALL OF SPACE.
E:	103.5°	359.4	CALIBRATE SIGNAL SEQUENCE ENDS AND RESTORE PERIOD STARTS.
F:	110.7°	384.4	RESTORE PERIOD ENDS
G:	121.5°	422.2	EARTH SCAN PERIOD BEGINS (600-NMI ORBIT)
H:	180°	625.0	SPACECRAFT NADIR
I:	238.5°	828.8	EARTH SCAN PERIOD ENDS (600-NMI ORBIT)
J:	250°	868.9	RADIOMETER IFOV JUST STARTING TO SEE HOUSING
K:	302°	1048.5	SCAN MIRROR POSITION PIP NO. 2 OCCURS AND 6.7 MICRON CHANNEL GAIN IS ATTENUATED BY A FACTOR OF 3.
L:	345°	1197.9	RADIOMETER IFOV COMPLETELY FILLED BY HOUSING
M:	355°	1232.6	RADIOMETER Z-AXIS

Figure 5. Nimbus-5 THIR 11-μm scan sequence.

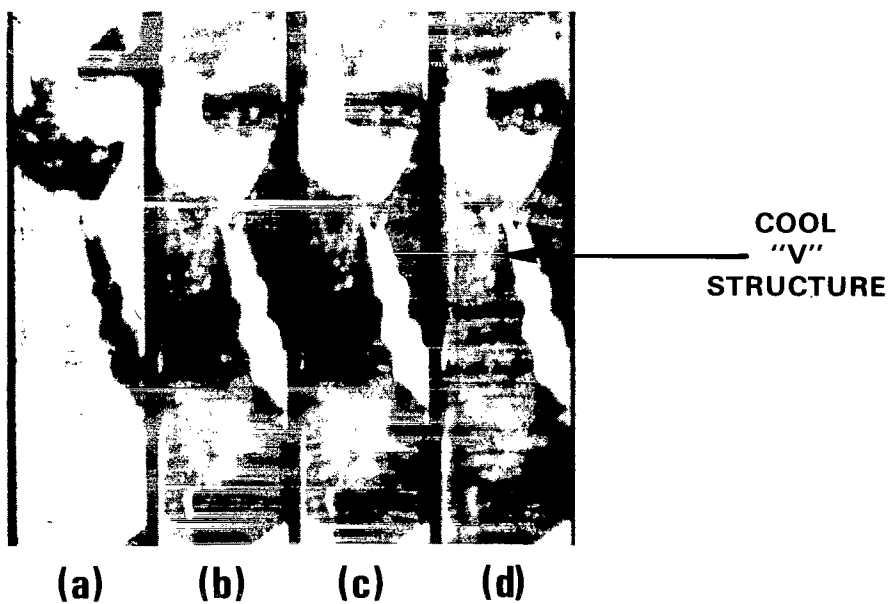


Figure 6. Nimbus-6 ESMR 37-GHz, orbit 618 (day), July 28, 1975, facsimile picture: (a) difference of (c) and (d); (b) average of (c) and (d); (c) vertical polarization; (d) horizontal polarization.

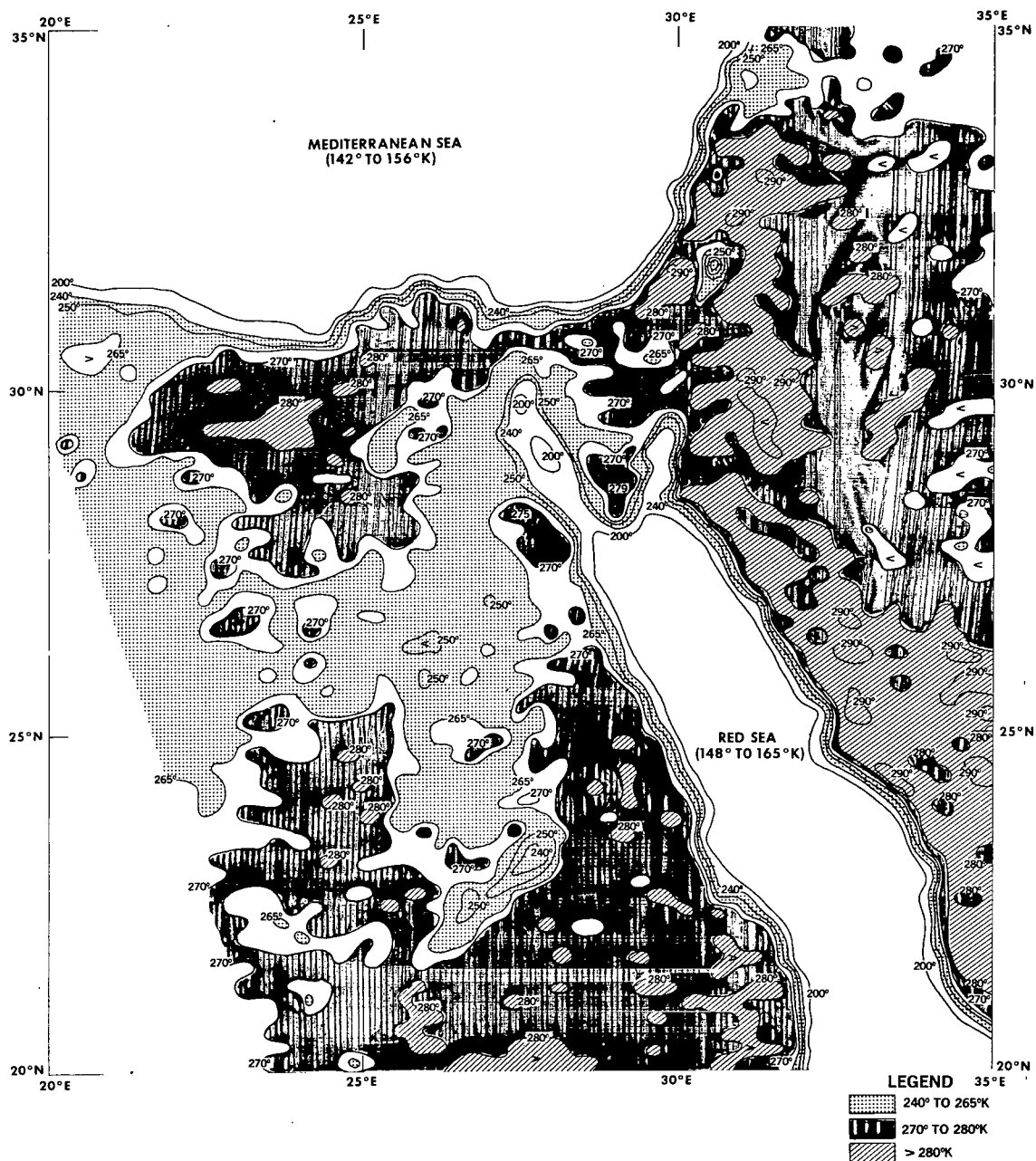


Figure 7. Nimbus-5 ESMR 19.35-GHz, orbit 3813 (day), September 21, 1973, horizontal polarization, analysis of computer-produced grid print map (1:2 million, Mercator).

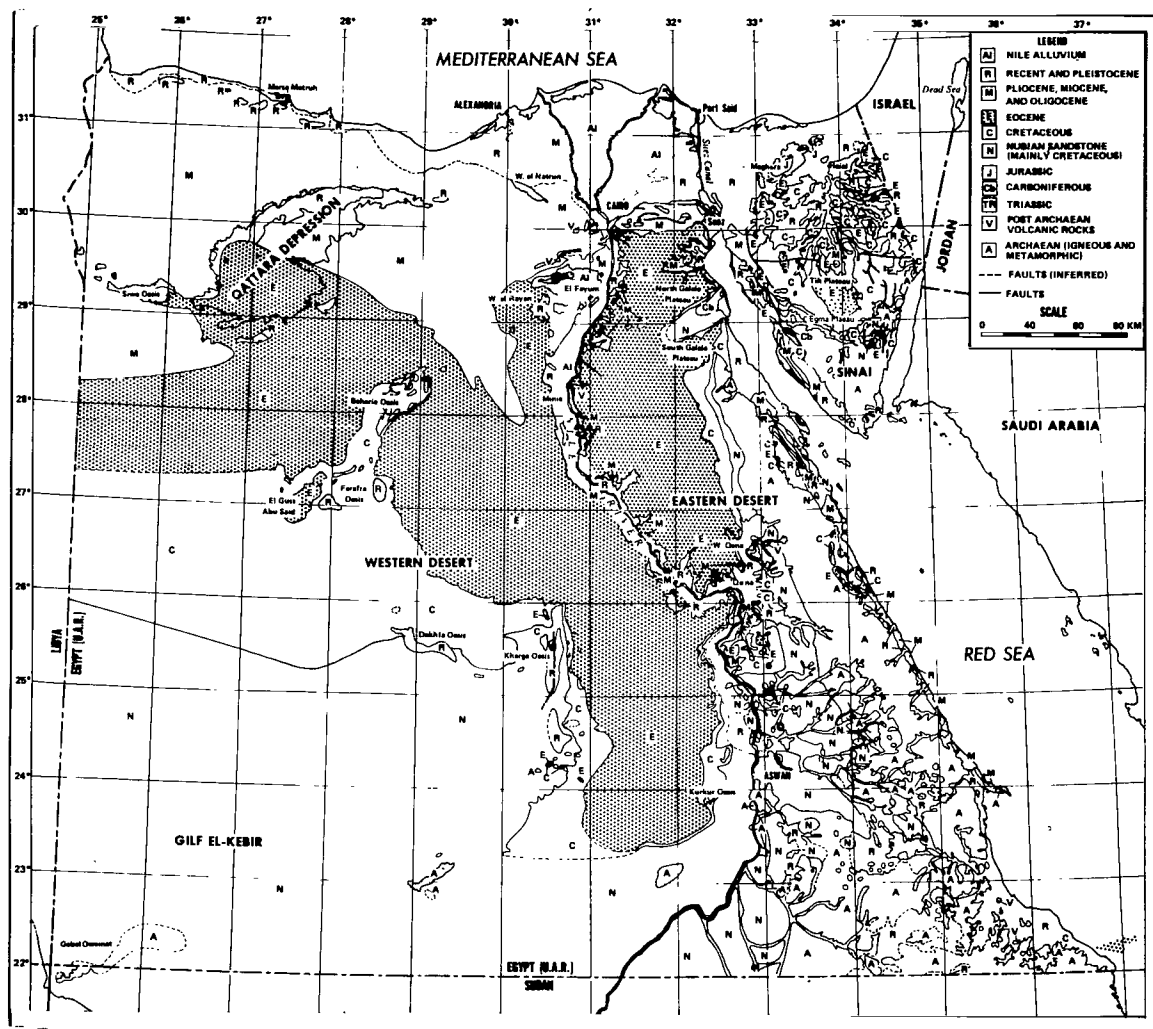


Figure 8. Geological map of Egypt (Said, 1966) (dotted area indicates large units of Eocene limestone).

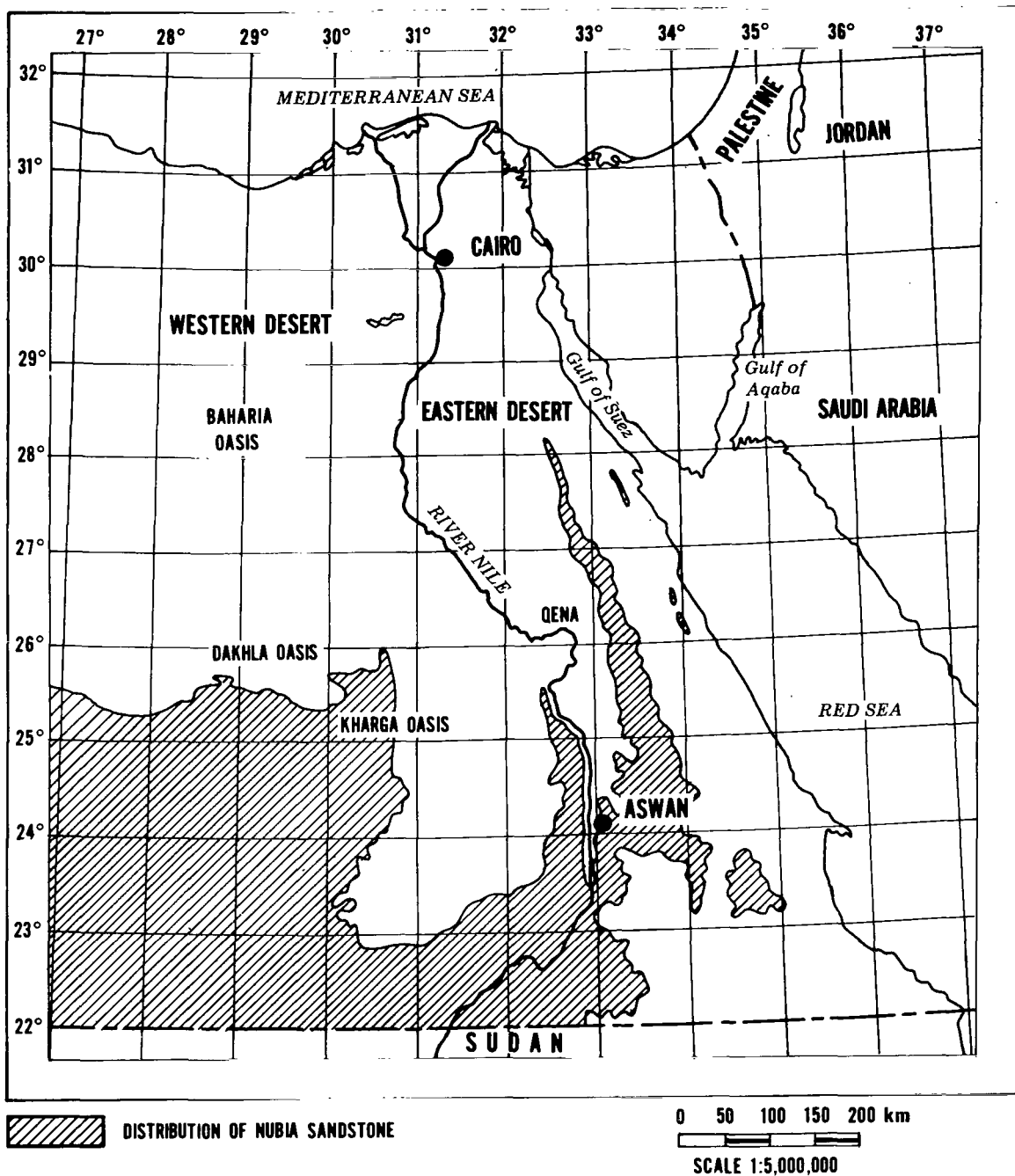
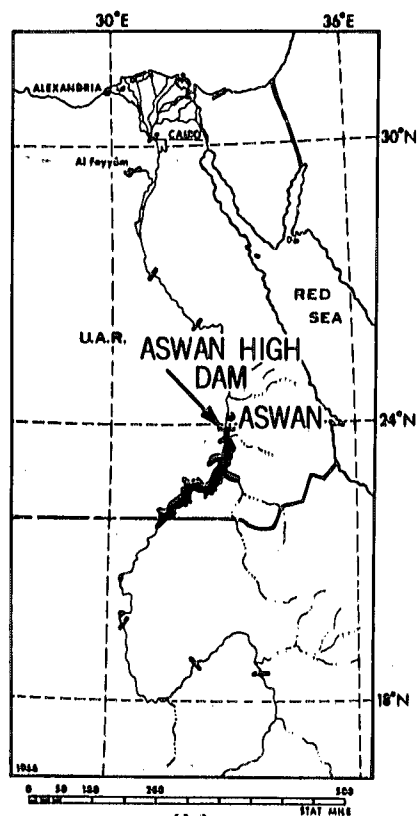


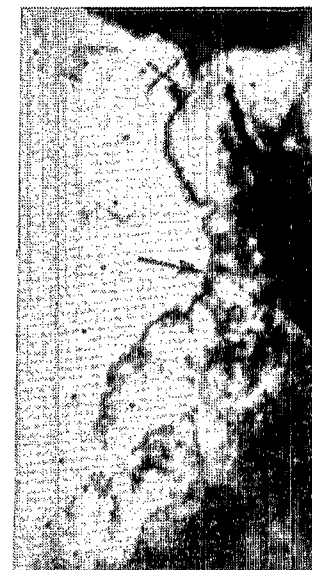
Figure 9. Map showing distribution of Nubia sandstone (diagonal lines) in Egypt (Reference 31).



(a)



(b)



(c)

Figure 10. a. Nimbus-3 HRIR (day), May 26, 1969, preflood stage of Lake Nasser; b. map of flood area of Lake Nasser; c. Nimbus-3 HRIR (day), September 11, 1966, flood stage.

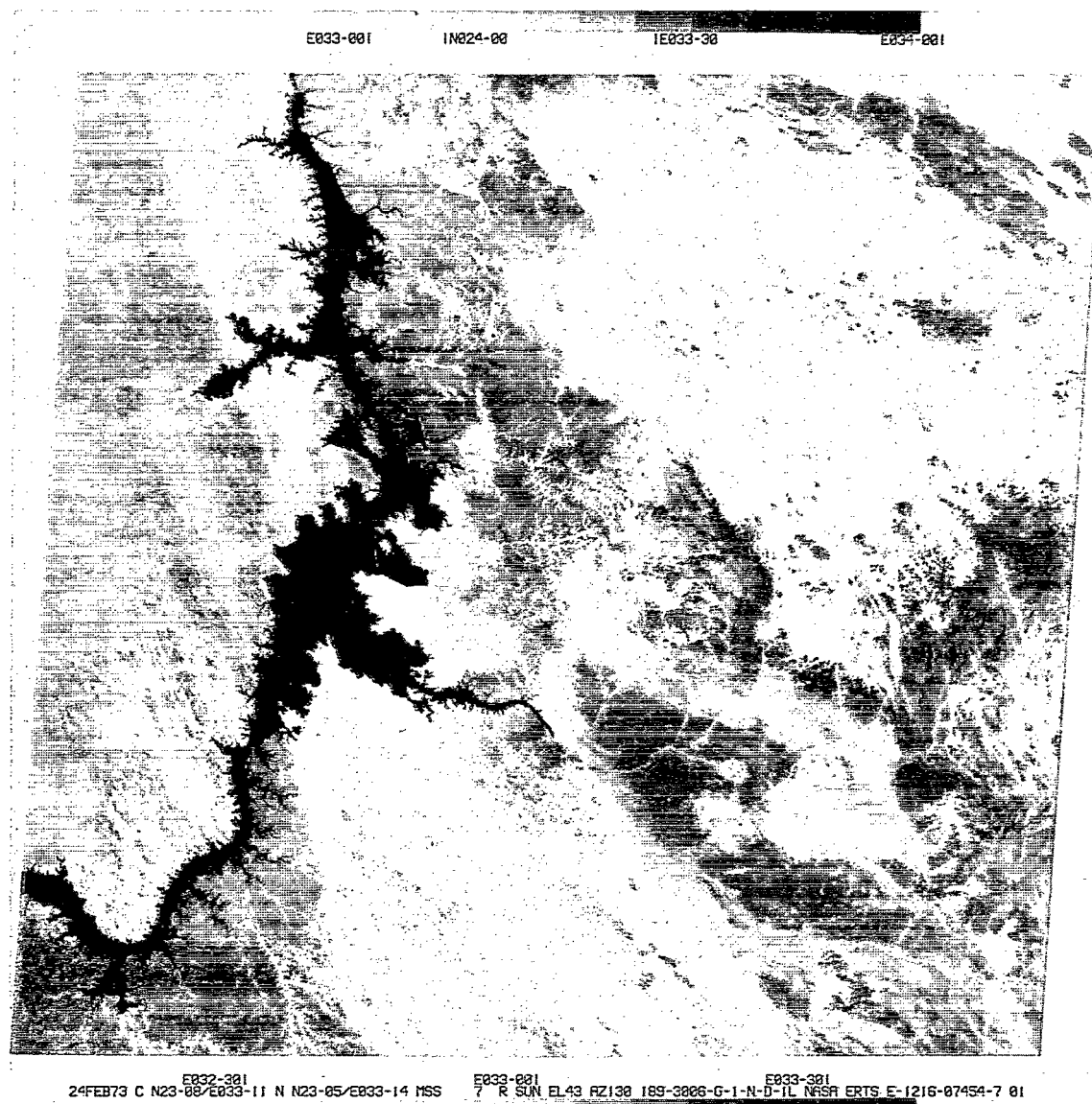


Figure 10d. Landsat-1 MSS-7, February 24, 1973, over Lake Nasser, Egypt (UAR).

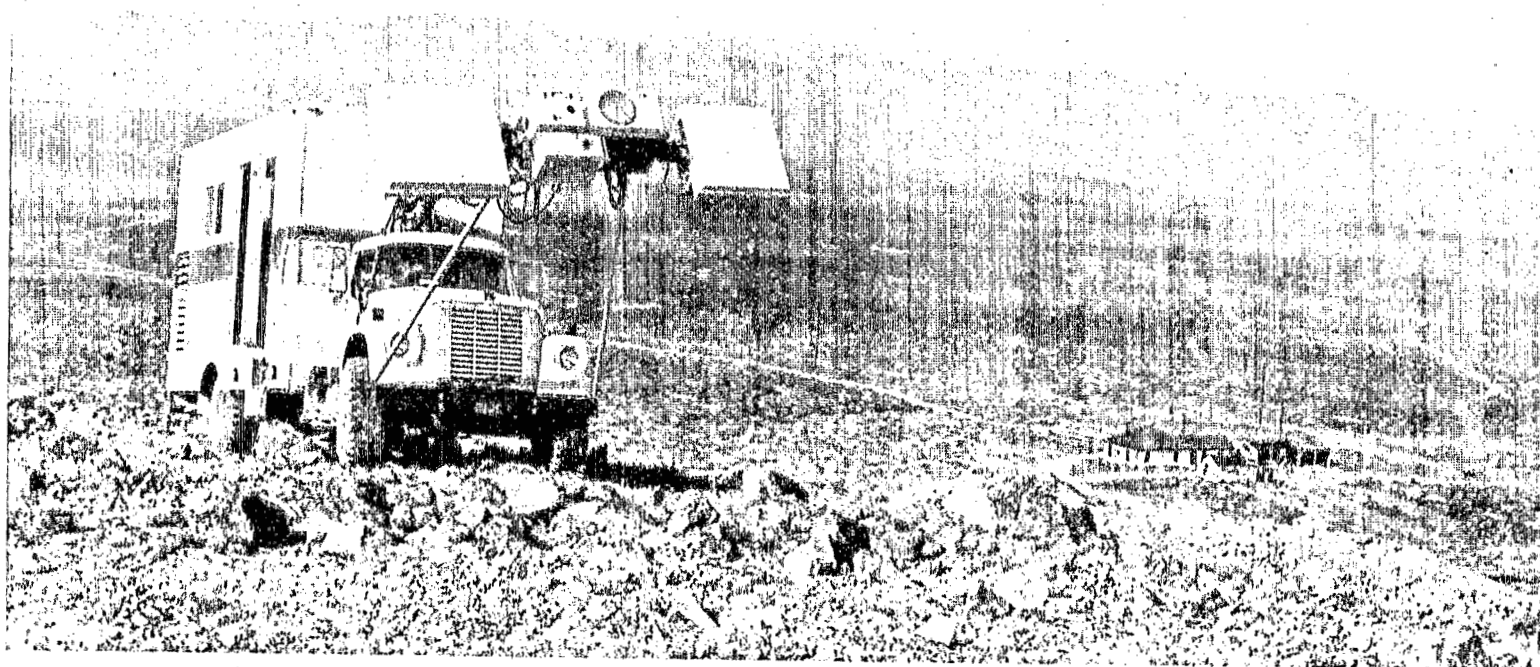


Figure 11. Truck-mounted passive microwave radiometer equipment used on geologic research (Reference 37).

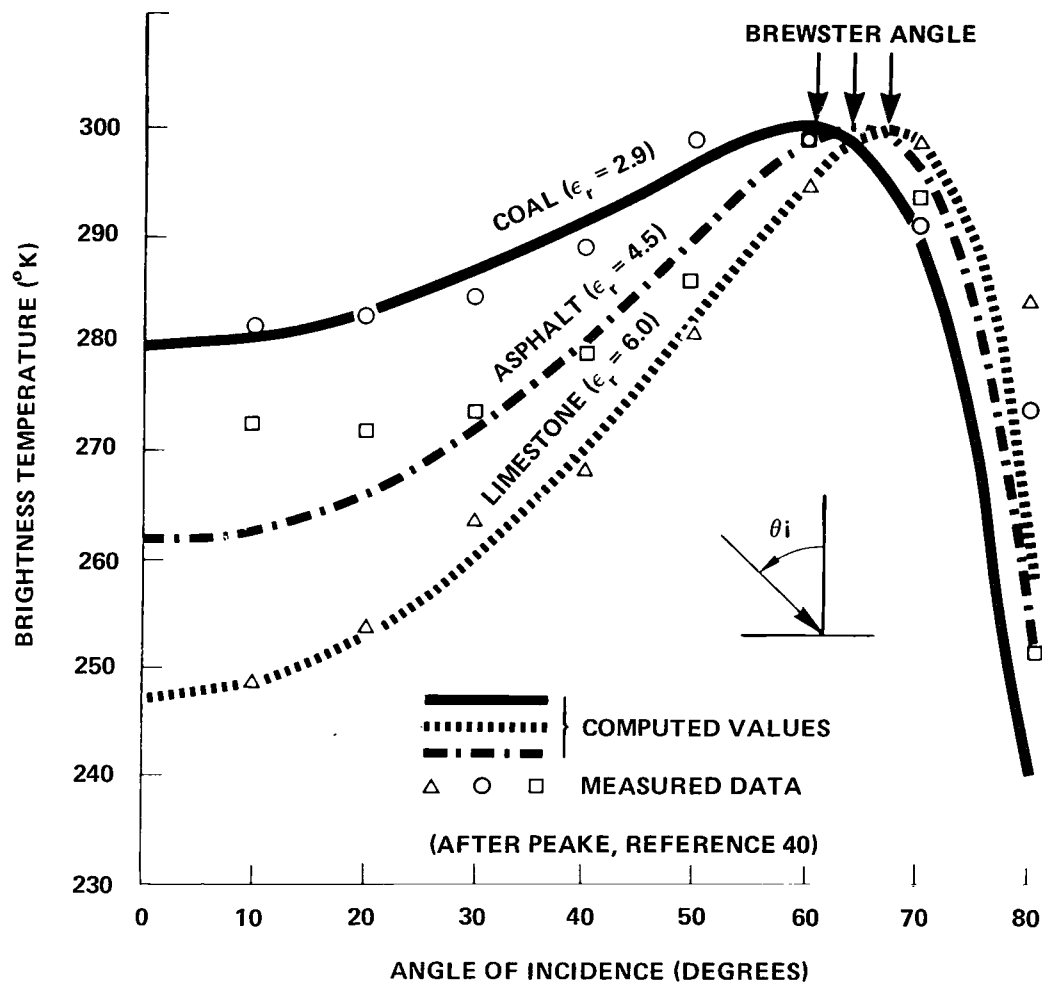


Figure 12. Computed and measured brightness temperatures of limestone, asphalt, and coal at 10 GHz, vertical polarization (Reference 37).

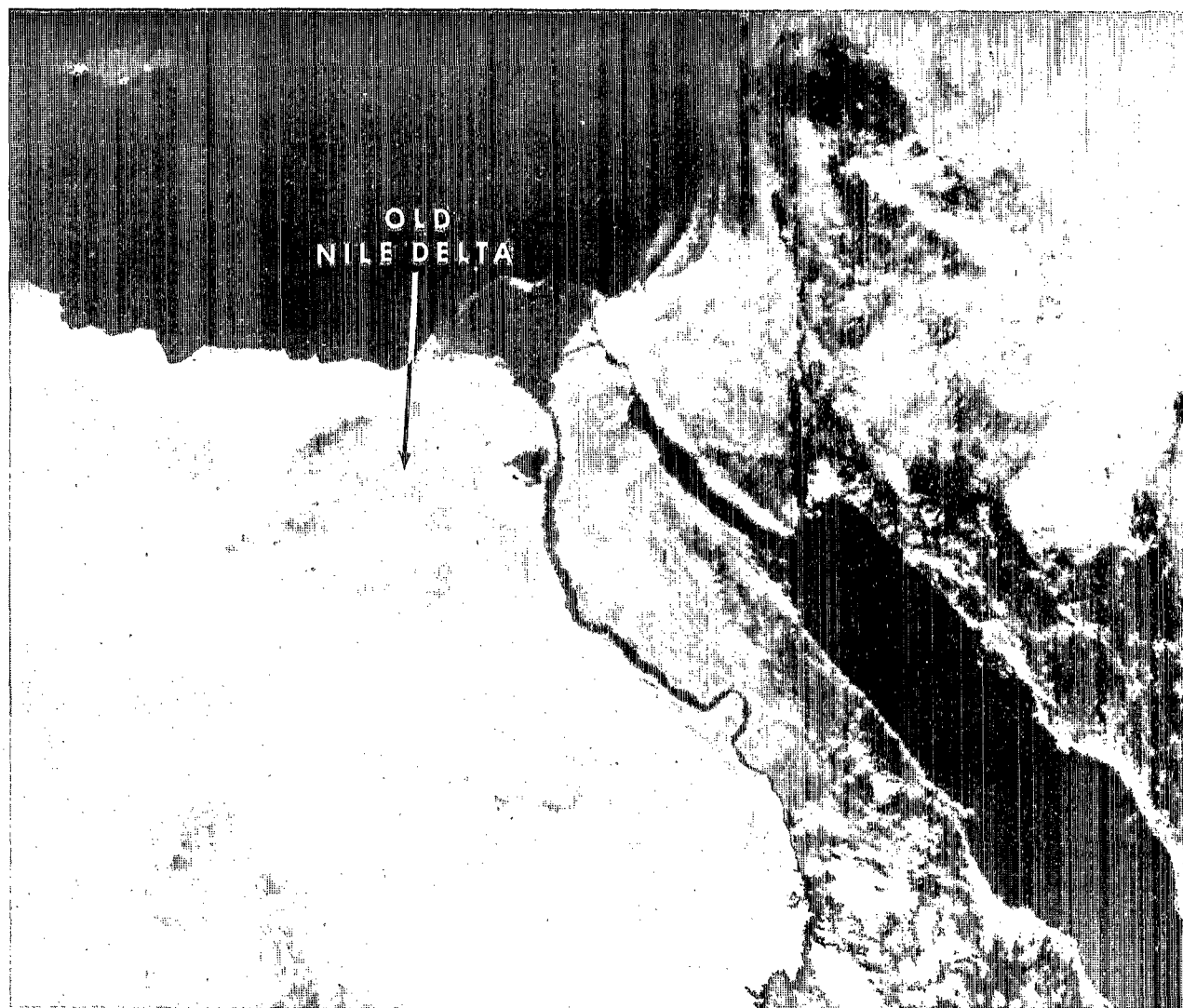


Figure 13. NOAA-2 visual picture (VHRR), October 23, 1974 (1-km resolution), over Egypt and Red Sea area.

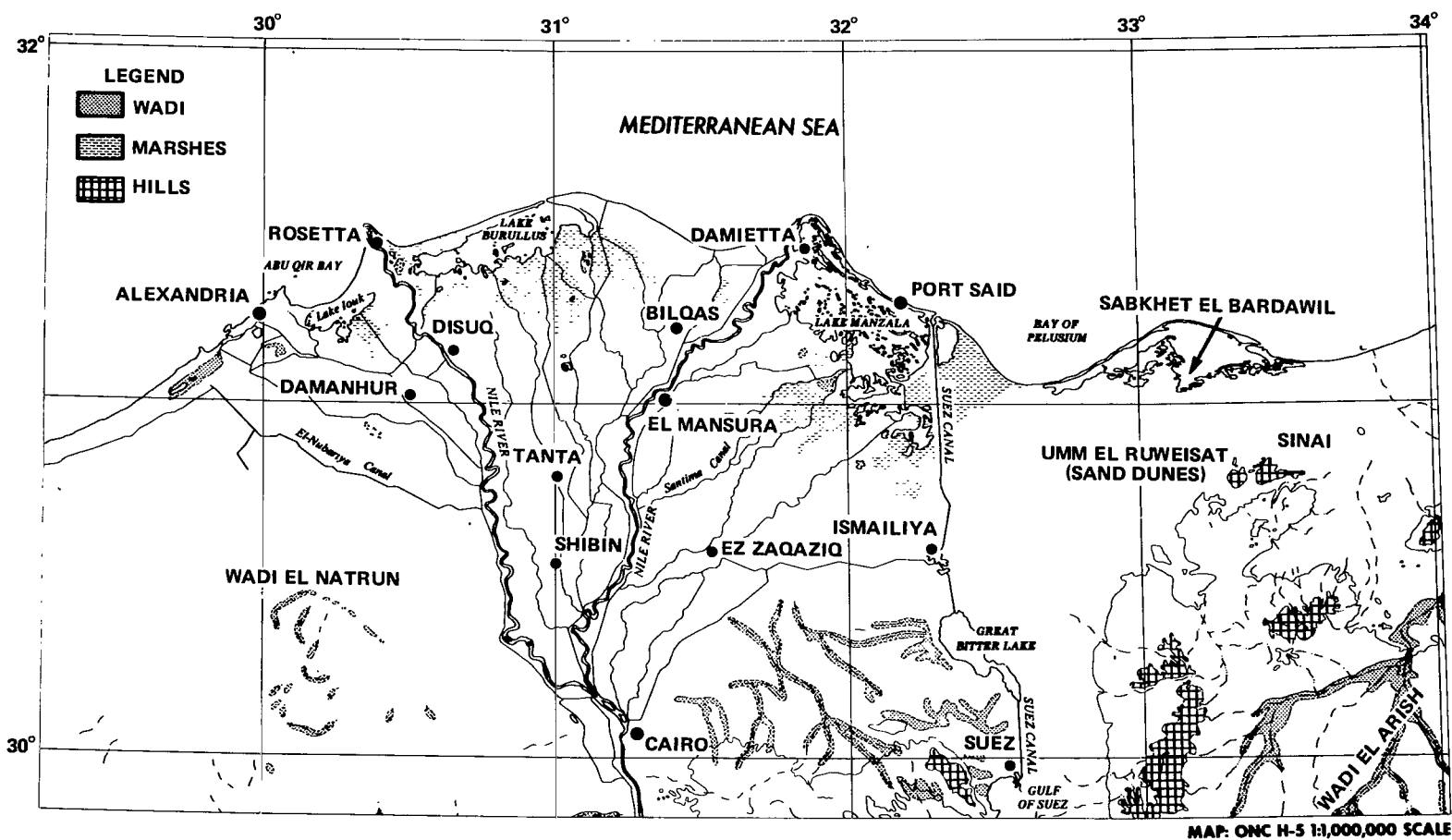


Figure 14. ONC H-5 map, 1:1 million scale of the Nile Delta.

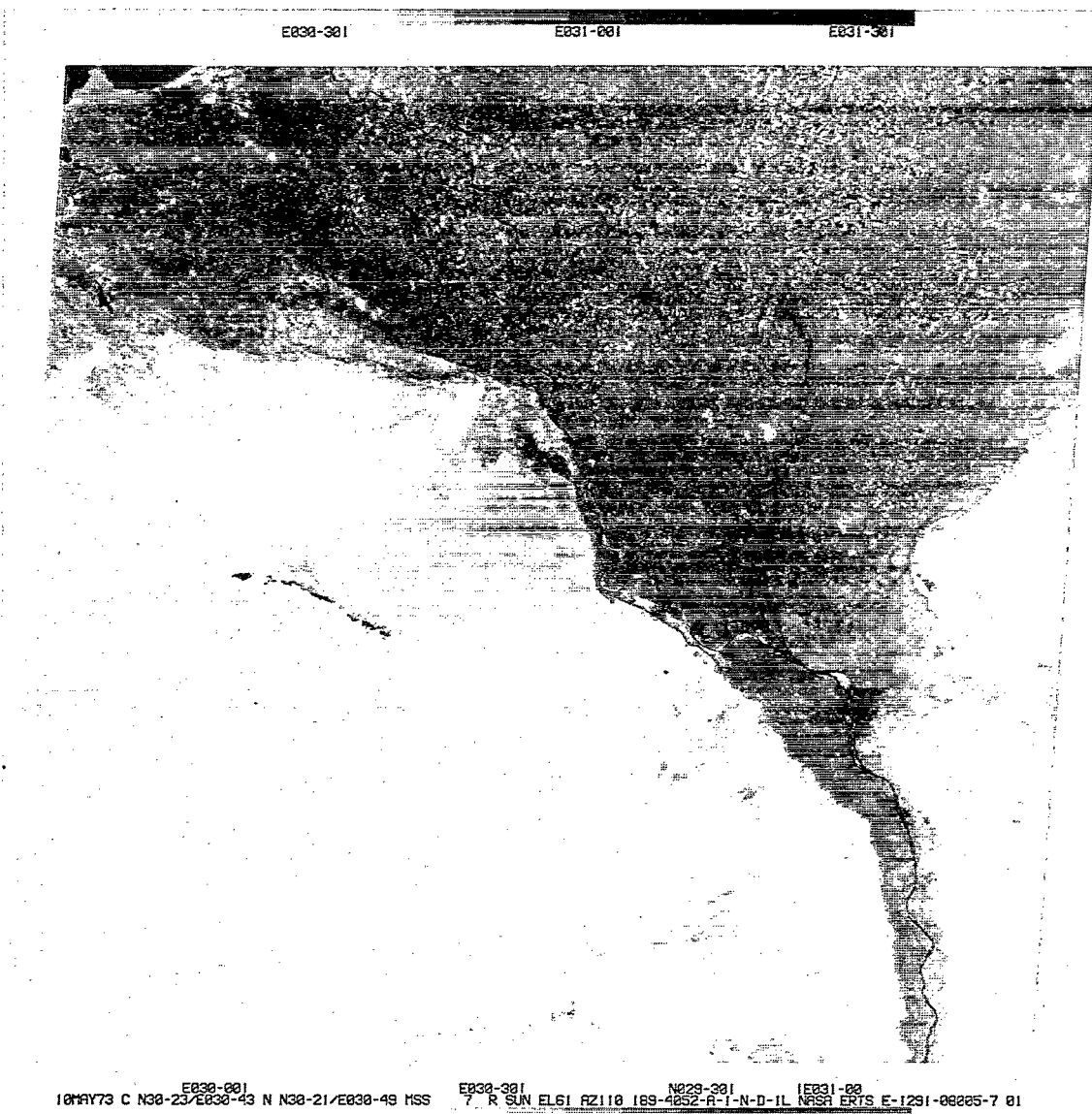


Figure 16. Landsat-2 MSS-7, May 10, 1973, over Nile Delta (southern end), Egypt (UAR).

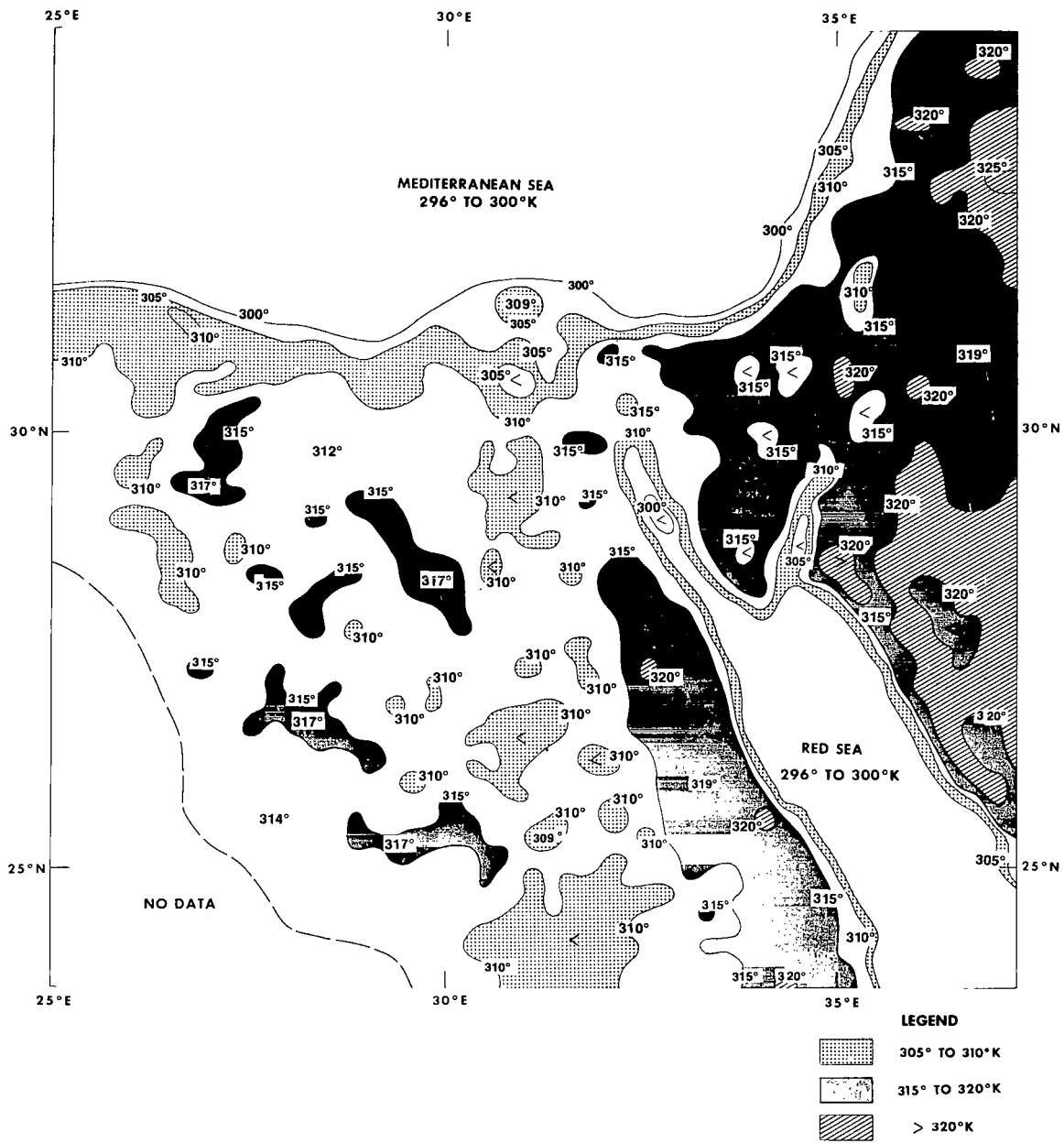


Figure 17. Nimbus-5 THIR 11- μ m, orbit 7813 (day), July 16, 1974, analysis of computer-produced grid print map (1:2 million, Mercator).

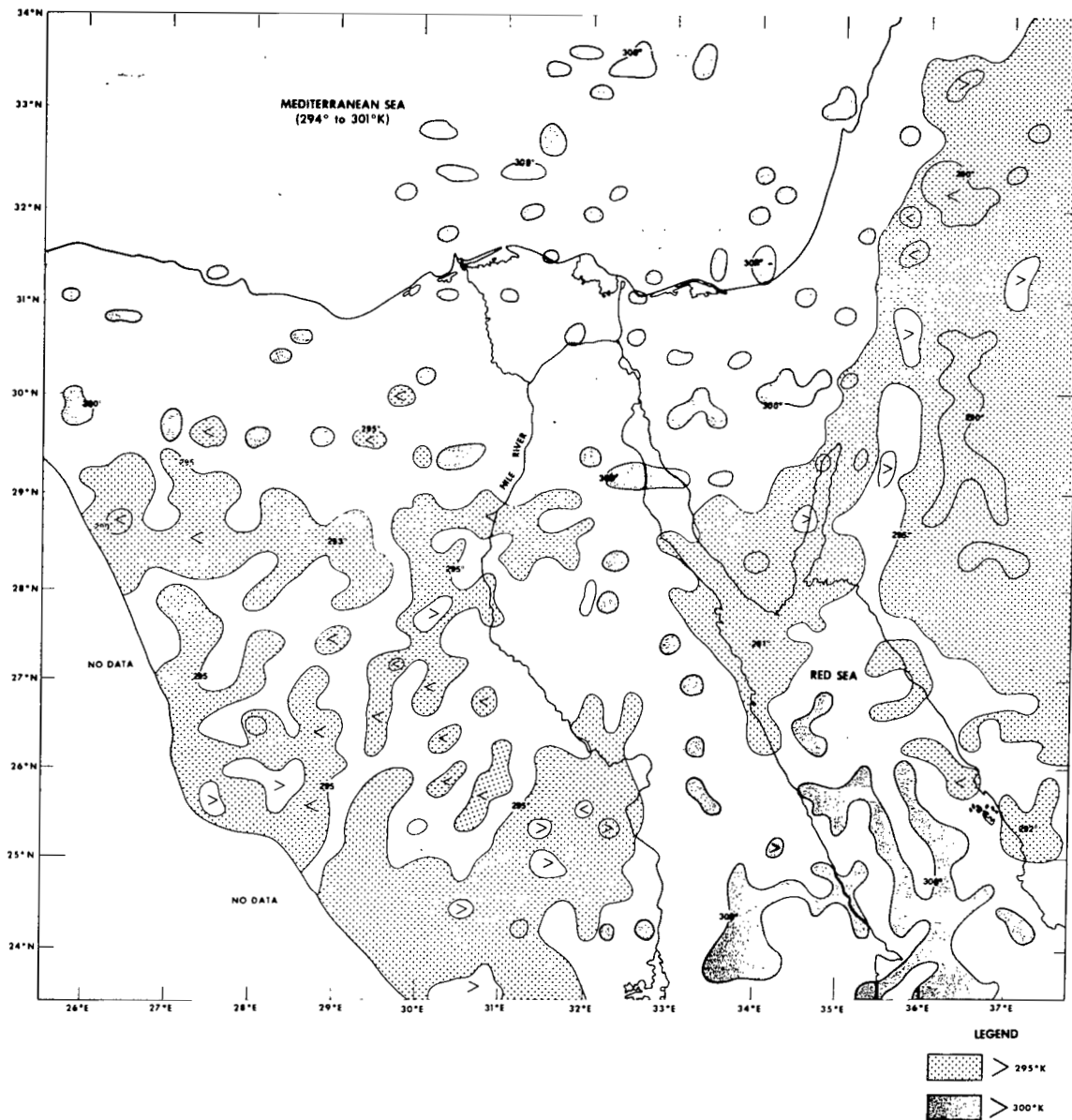


Figure 18. Nimbus-5 THIR 11- μ m, orbit 7821 (night), July 16, 1974, analysis of computer-produced grid print map (1:2 million, Mercator).

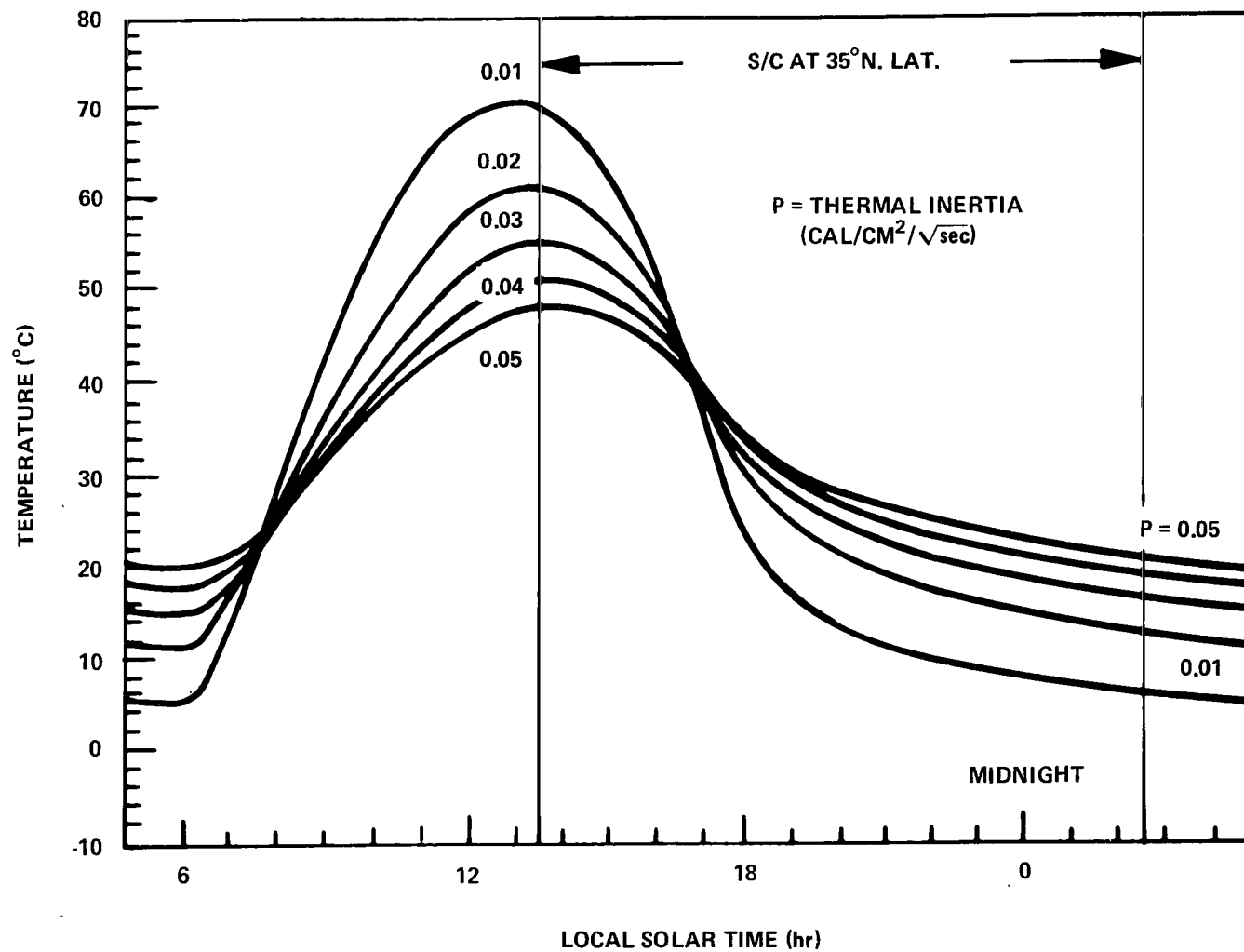


Figure 19. Diurnal surface temperature variation as a function of thermal inertia (Reference 46).

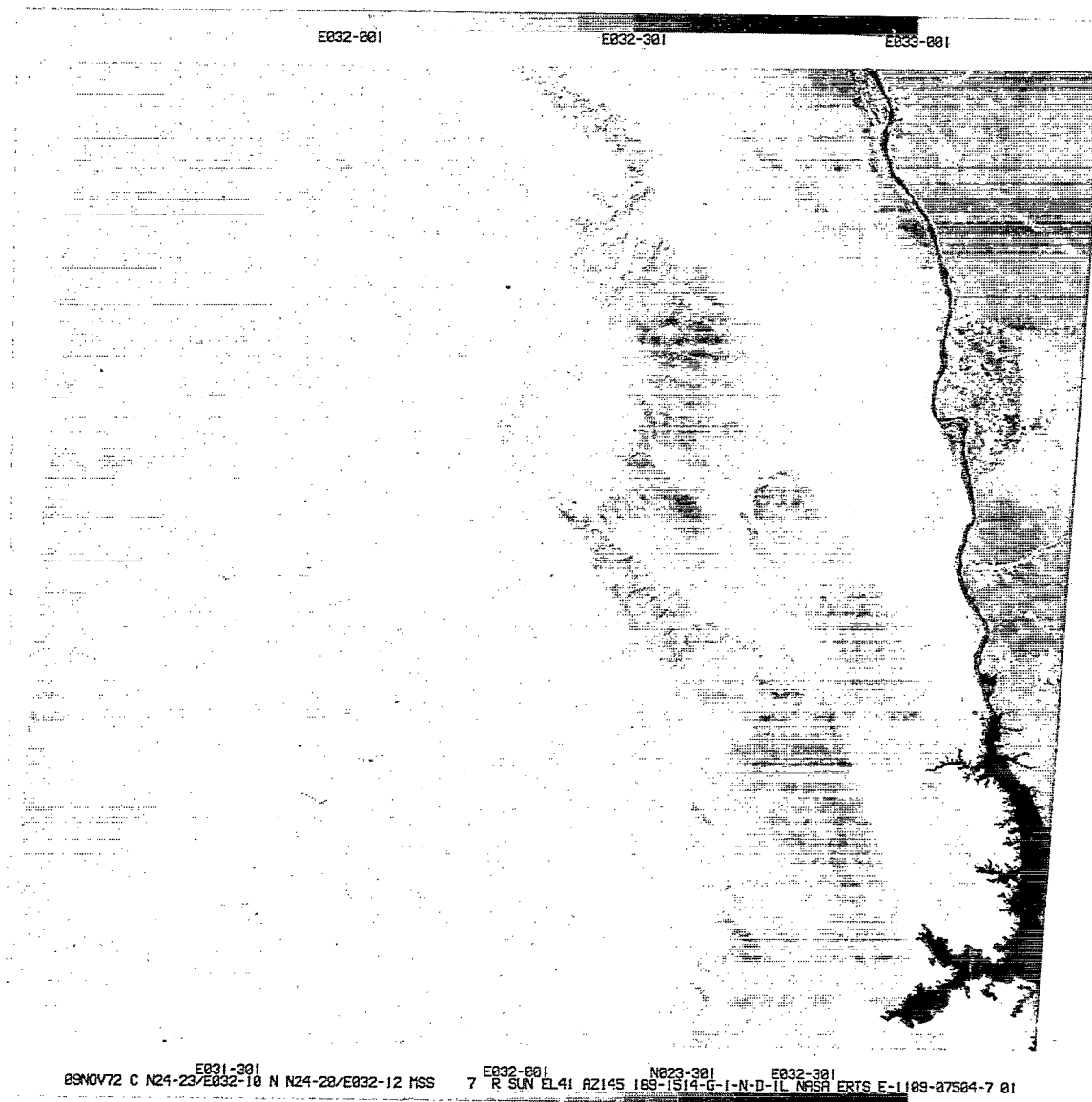


Figure 20a. Landsat-1 MSS-7, November 9, 1972, Lake Nasser and Nile Valley, Egypt (UAR).

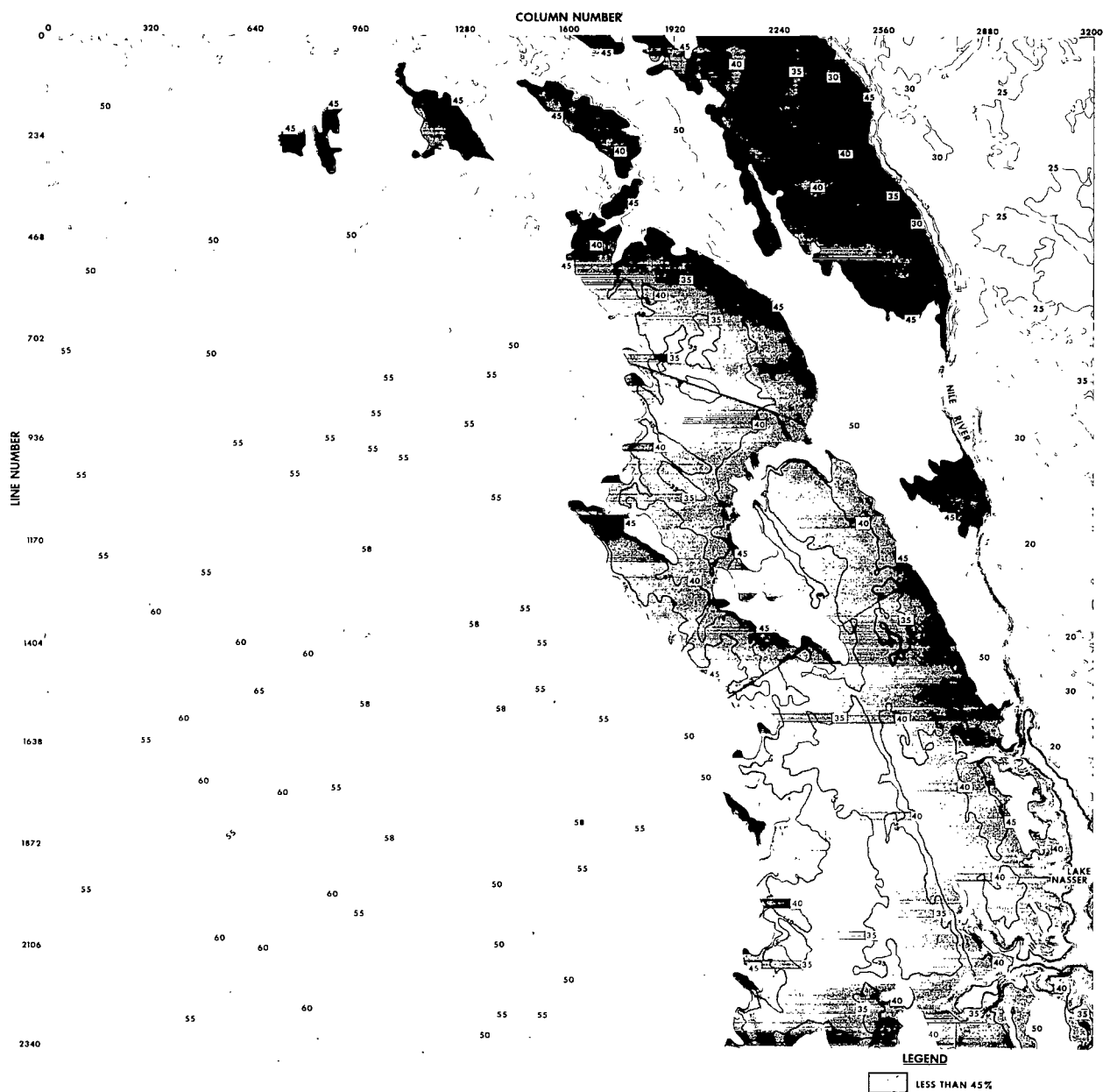


Figure 20b. Space reflectivity (%) derived from Landsat-1 MSS-7, November 9, 1972, frame shown in figure 20a (Cal-Comp line-drawn).

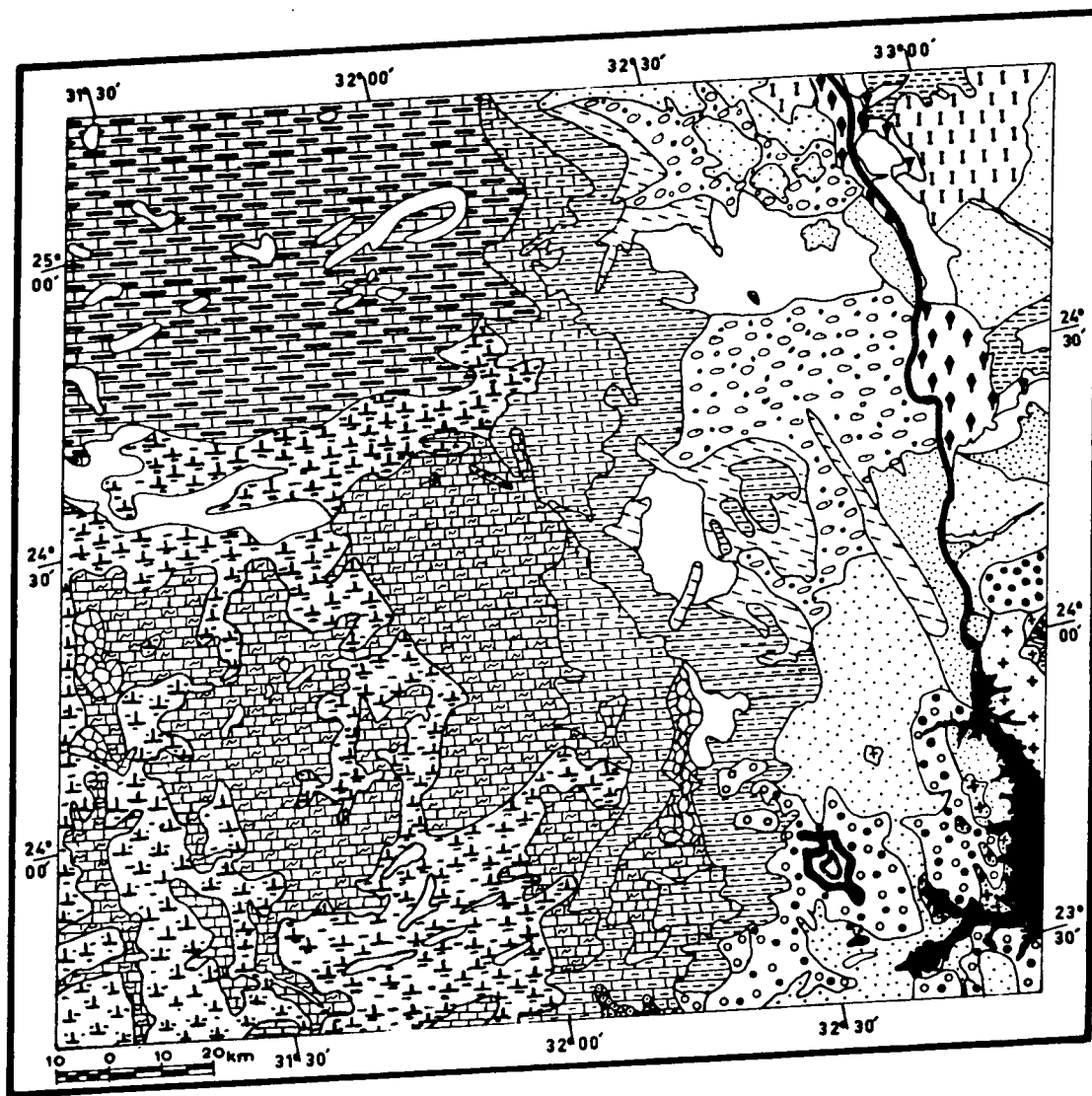


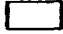



Figure 21. Geological map of West Aswan area, derived from Landsat-1 MSS-7, November 9, 1972, frame shown in figure 20a (Reference 32).


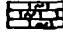
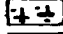
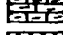


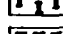
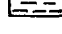
FORELAND SEDIMENTS

FIFTH DETRITAL CALCAREOUS - EVAPORITE SEDIMENTS





- | | |
|--|--|
|  CULTIVATION |  VEGETATION |
|  SURFACIAL DEPOSITS,
MAINLY ALLUVIUM |  ALLUVIUM - ELUVIUM |

- | | |
|--|---|
|  PLAYA | |
|  CONGLOMERATE | |
|  DARB EL GALLABA GRAVEL | |
|  TUFA |  CALCITE |

FOURTH CALCAREOUS SEDIMENTS

- | | |
|---|--|
|  GEBEL SERAI FORMATION | |
|  GEBEL SERAI FORMATION, BASAL | |
|  UPPER ESNA FORMATION | |
|  GEBEL GARRA FORMATION ≈ TARAWAN FORMATION | |
|  KURKUR FORMATION | |
|  LOWER ESNA FORMATION ≈ DAKHLA FORMATION | |
|  GEBEL DUWI PHOSPHATE FORMATION | |
|  WADI ABBAD FORMATION | |

THIRD DETRITAL SEDIMENTS

- | | |
|--|--|
|  NUBIAN SANDSTONE, LINEATED WITH WINDBLOWN SAND | |
|  NUBIAN SANDSTONE, UNDIFFERENTIATED | |
|  NUBIAN SANDSTONE, IRON - ORE MEMBER | |
|  NUBIAN SANDSTONE, BASAL | |

POST OROGENIC PLUTONITES

- | | |
|--|--|
|  ASWAN MONUMENTAL GRANITE
AND ASSOCIATED ROCKS | |
|--|--|

LATE OROGENIC PLUTONITES

- | | |
|--|--|
|  PINK GRANITE | |
|--|--|

GEOSYNCLINAL SEDIMENTS

- | | |
|---|--|
|  METASEDIMENTS | |
|---|--|

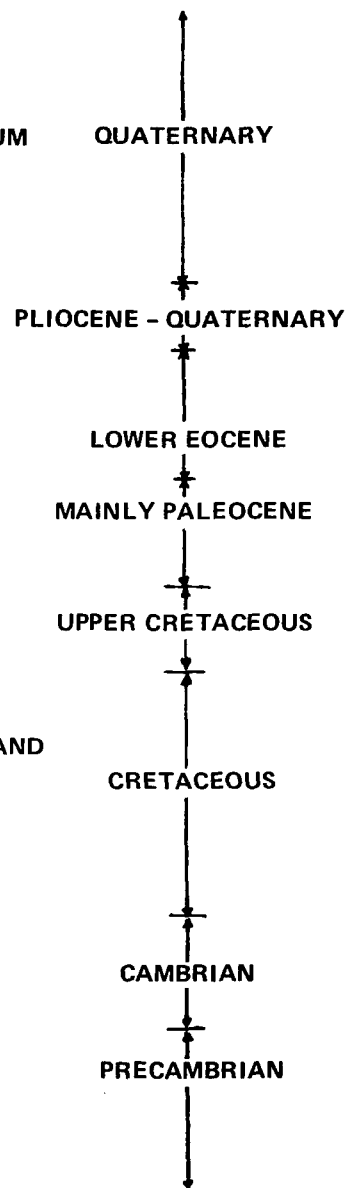


Figure 22. Geological unit classification used in figure 21 (Reference 32).

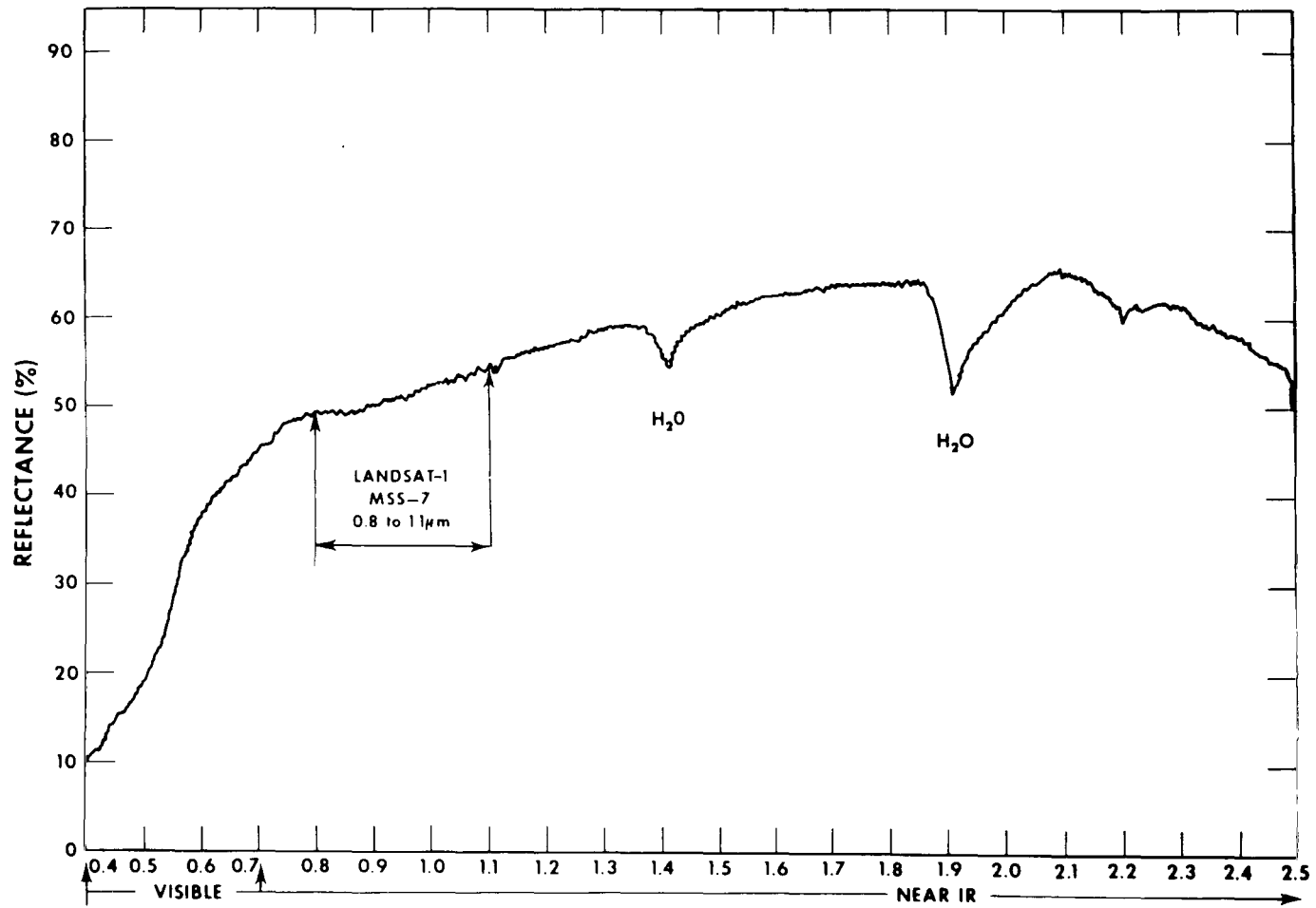


Figure 23. Laboratory spectrophotographic analysis of Sinai desert sand showing total diffusive reflectance (%).

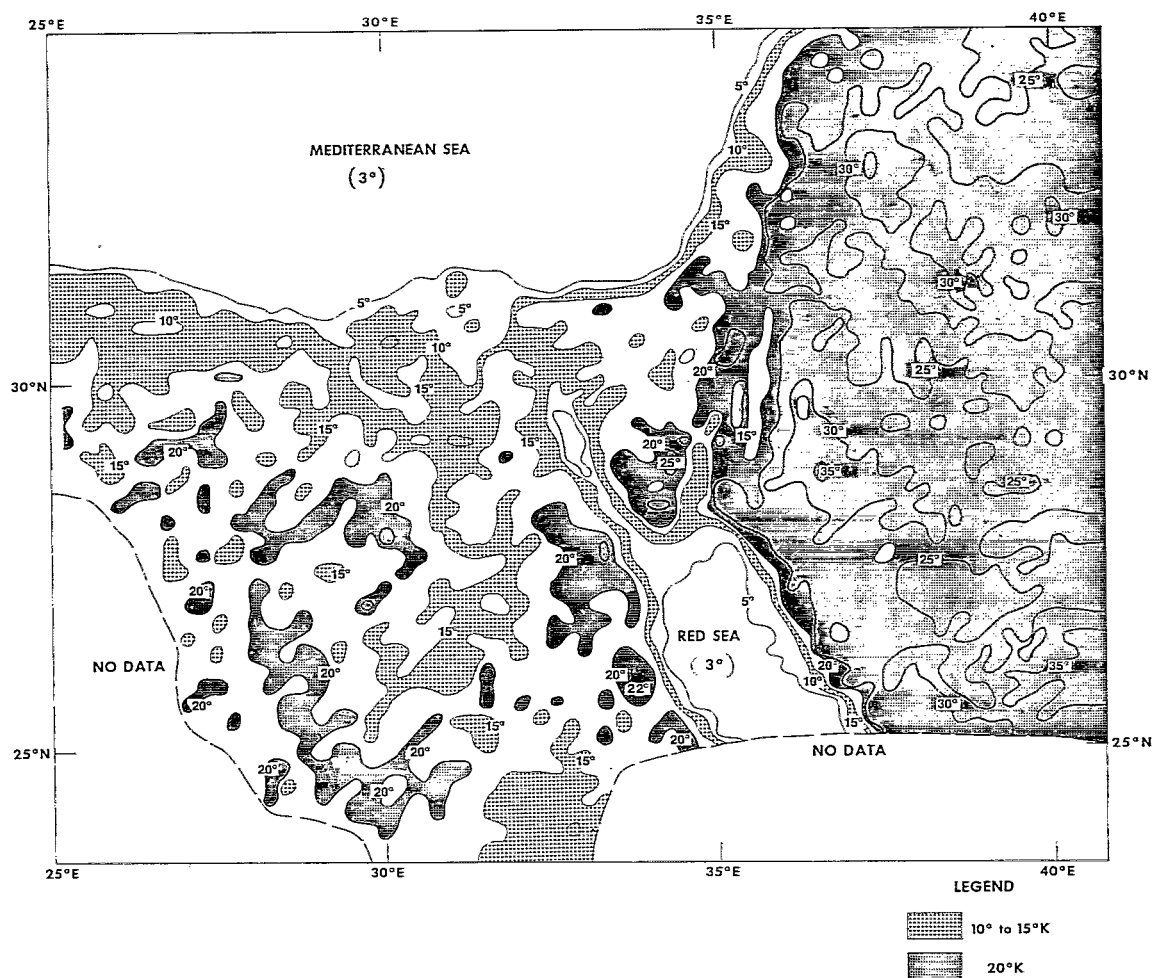


Figure 24. Nimbus-5 THIR 11- μ m, orbit 7813 (day) - orbit 7821 (night), July 16, 1974; analyses of brightness temperature difference, computer-produced grid print map (1:2 million, Mercator).

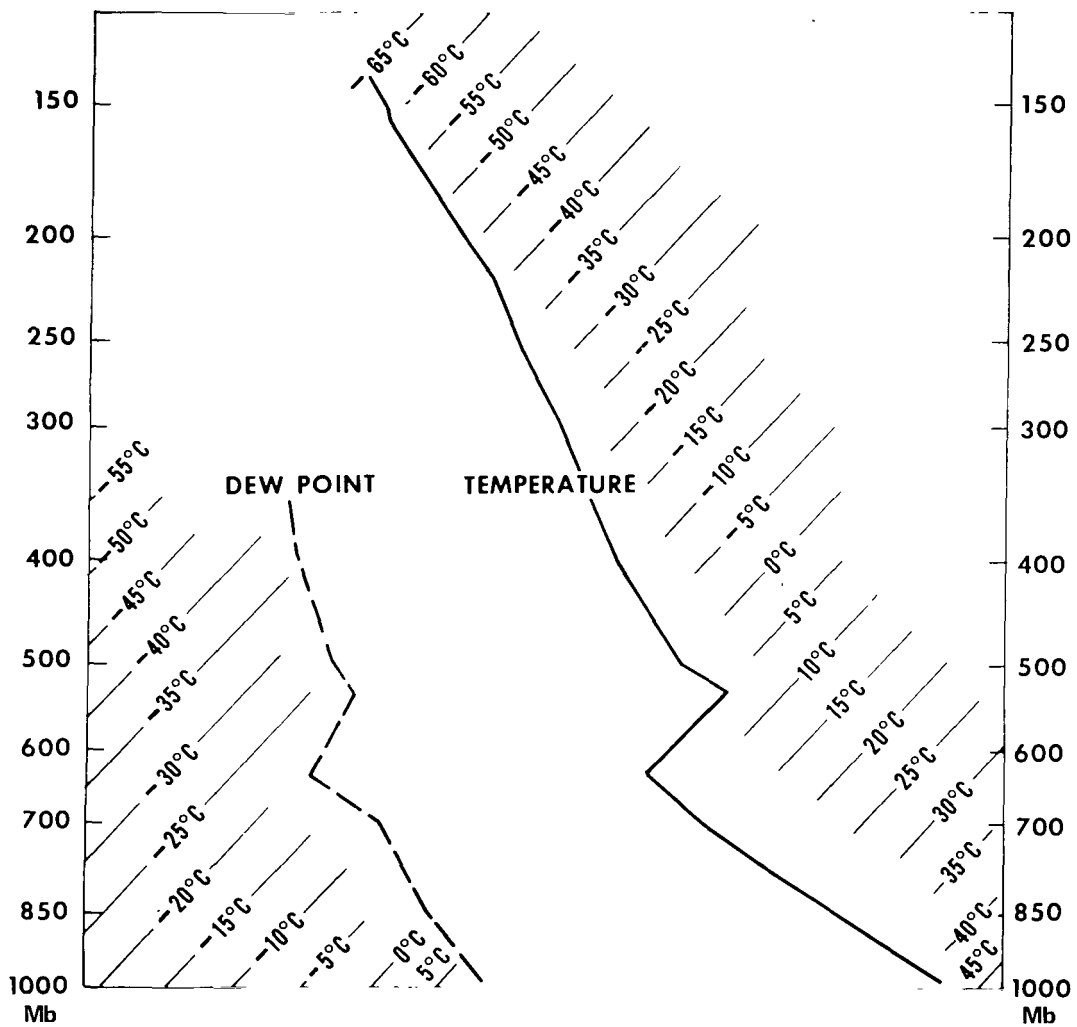


Figure 25. Radiosonde data, 1200 GMT, July 16, 1974, Aswan, Egypt (UAR)

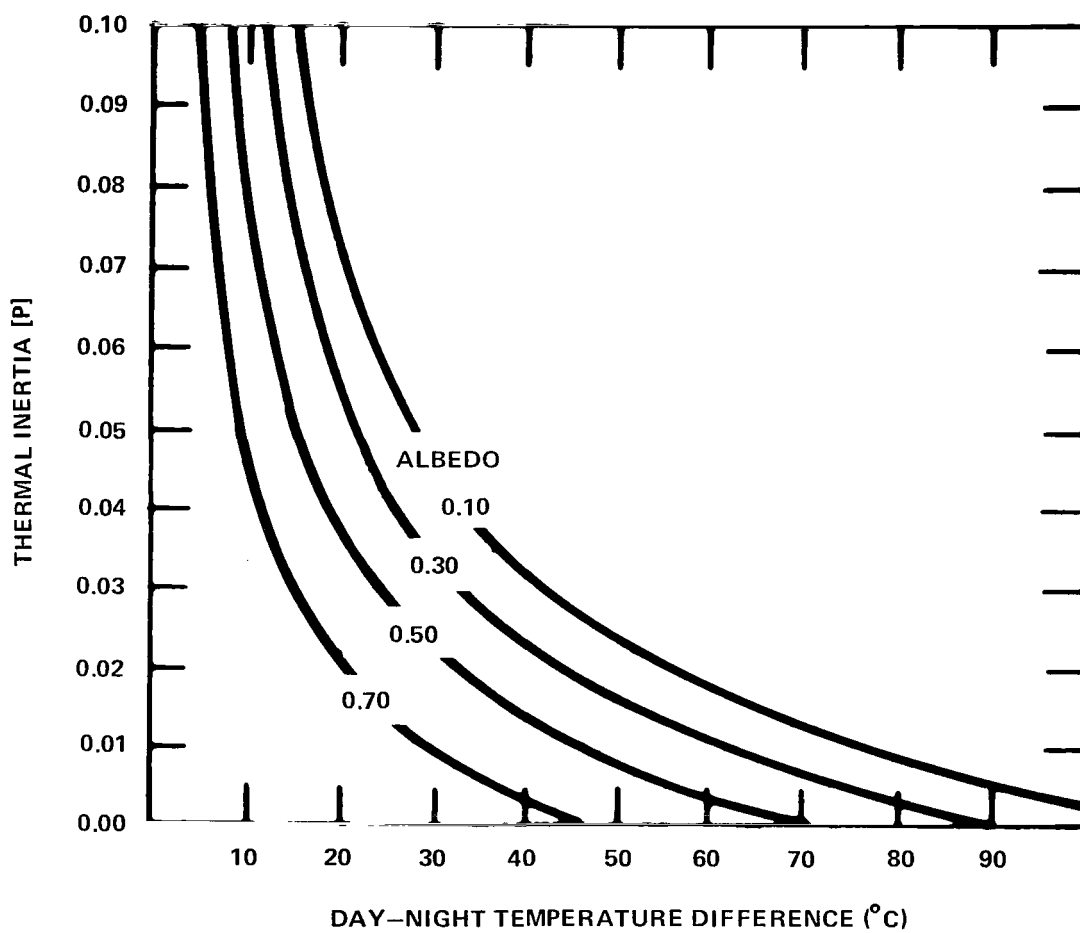


Figure 26. Least-squares fit of thermal inertia versus day-night temperature difference for albedos ranging from 0.10 to 0.70 (Reference 45).

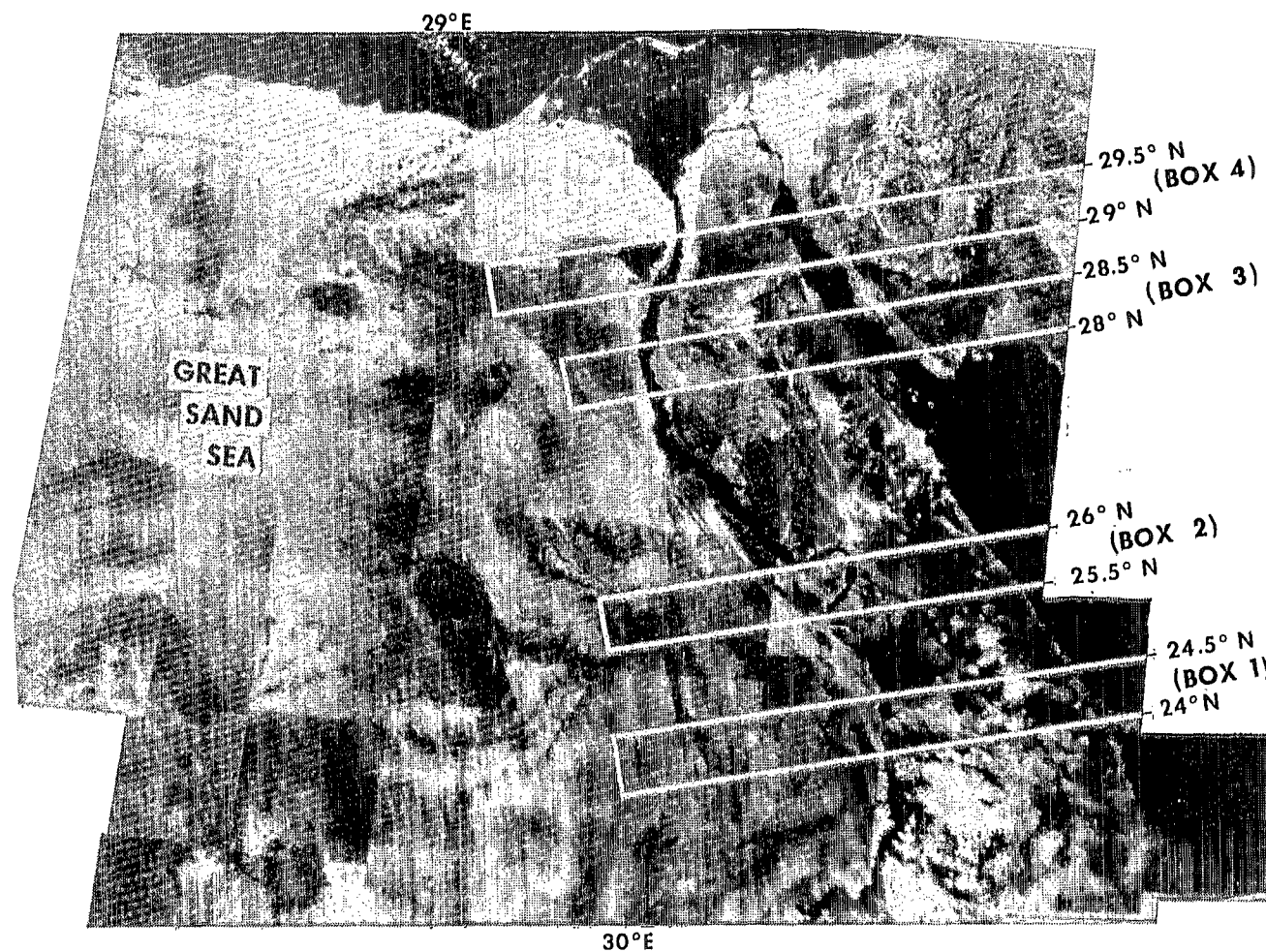


Figure 27. Landsat-1 MSS-7, uncontrolled composite photomosaic of all available cloud-free orbits over Egypt (UAR), with four boxes showing region of THIR and ESMR T_B comparison.

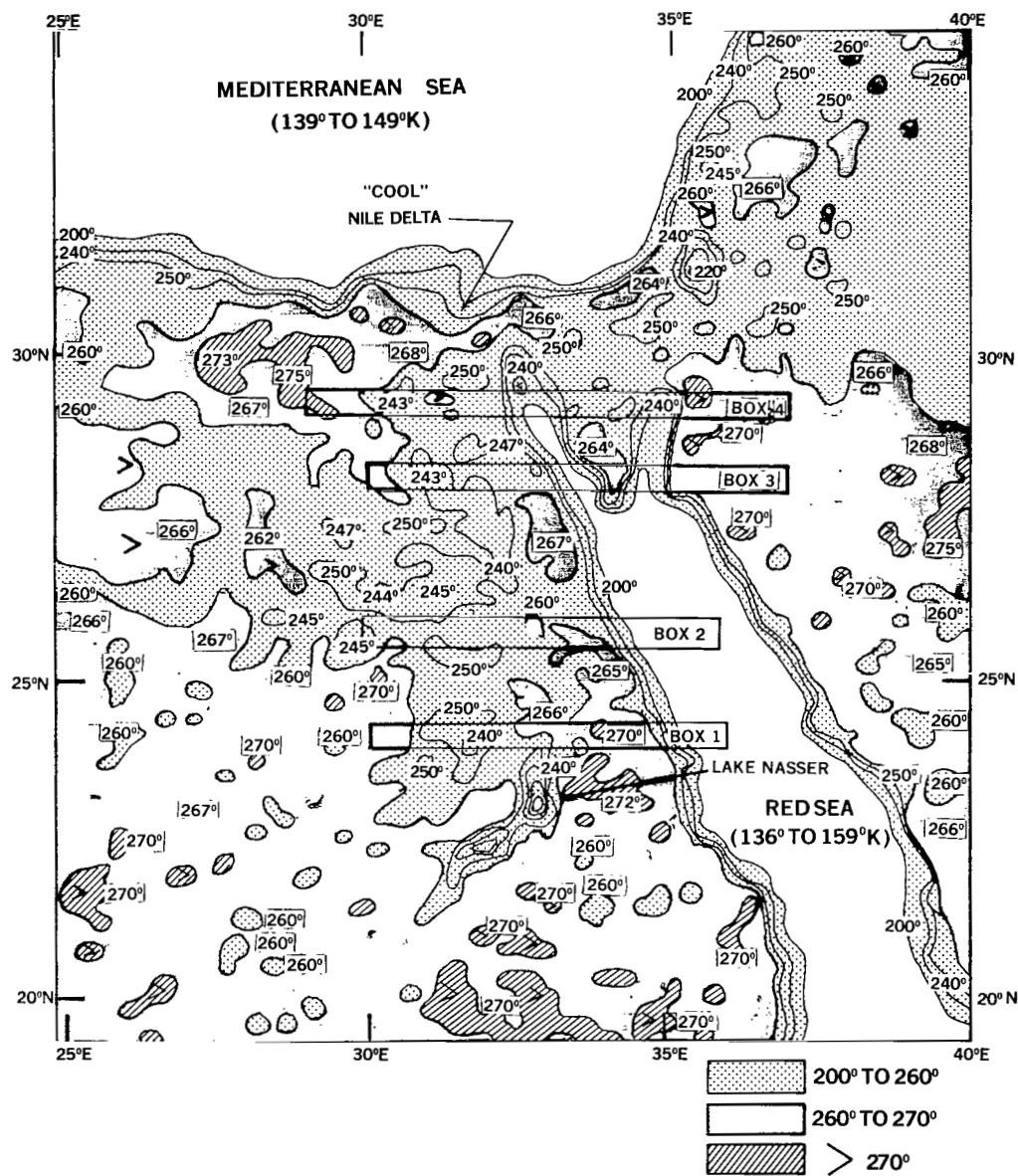


Figure 28. Nimbus-5 ESMR 19.35 GHz, orbit 7821 (night), July 16, 1974, horizontal polarization; analysis of computer-produced grid print map (1:2 million, Mercator) with four boxes showing region of THIR and ESMR T_B comparison.

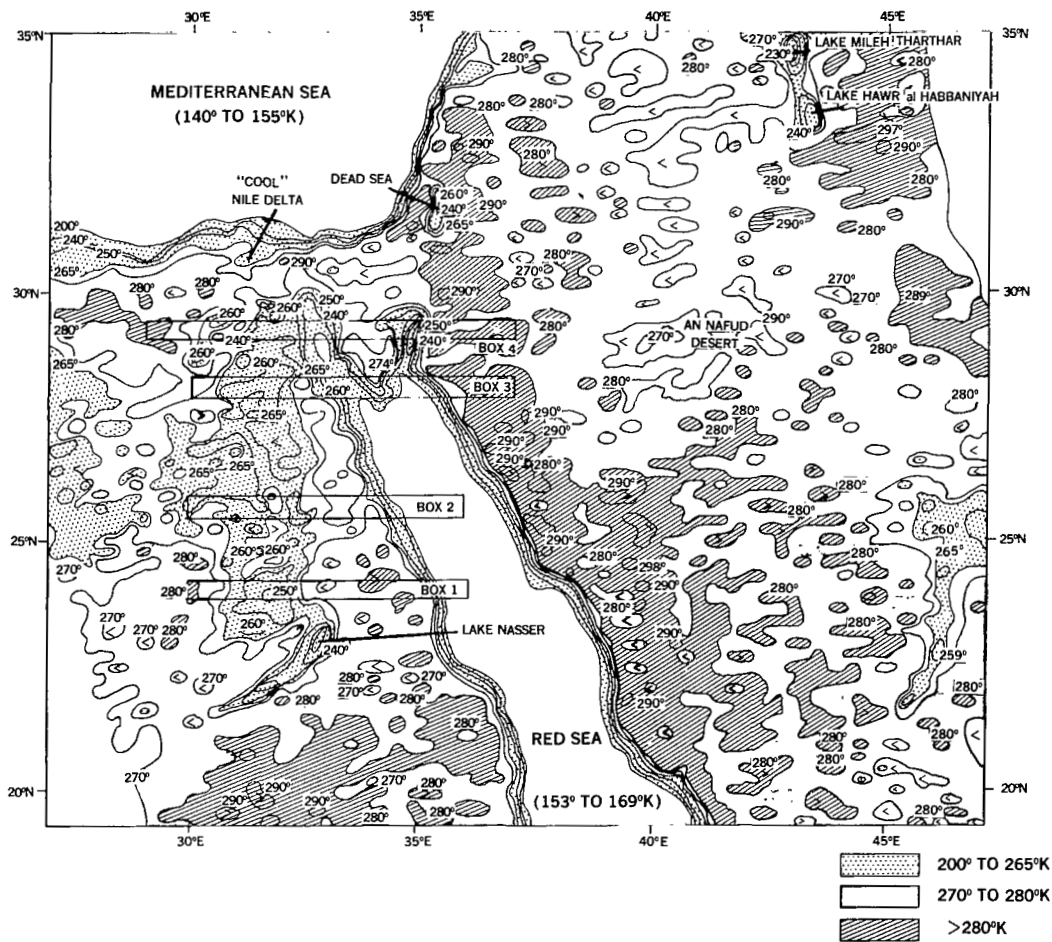


Figure 29. Nimbus-5 ESMR 19.35 GHz, orbit 7934 (day), July 25, 1974, horizontal polarization; analysis of computer-produced grid print map (1:2 million, Mercator) with 4 boxes showing region of THIR and ESMR T_B comparison.

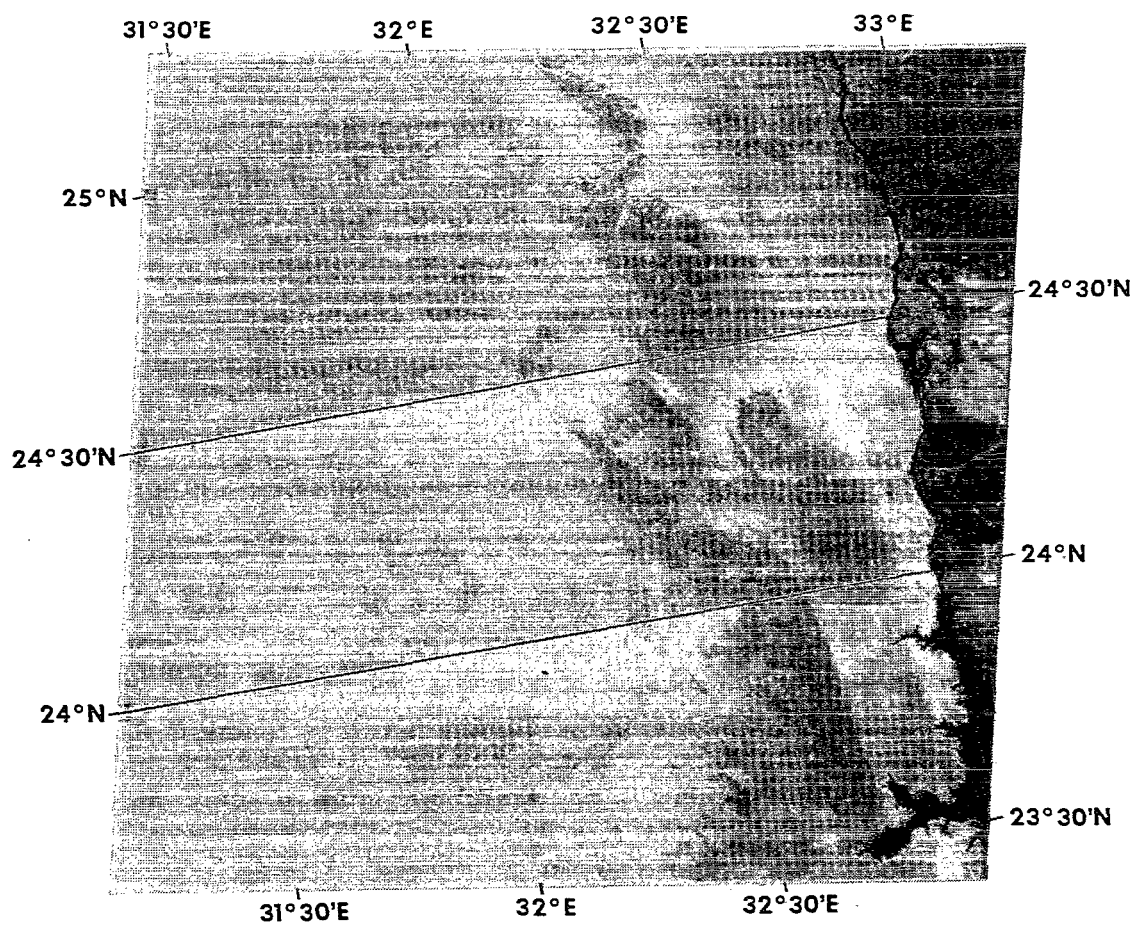


Figure 30. Landsat-1 MSS-7, November 9, 1972, Lake Nasser and Nile Valley, Egypt (UAR), with box limits of THIR and ESMR T_B comparison.

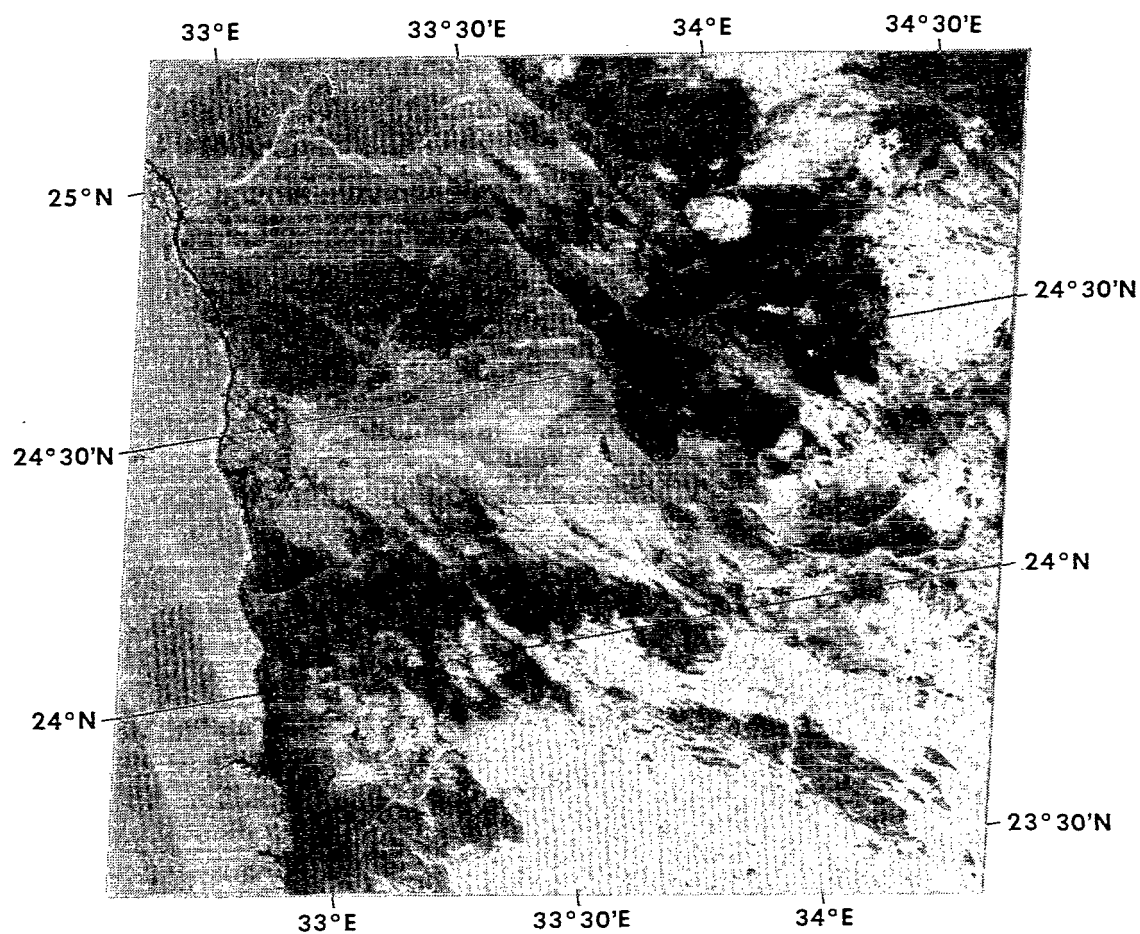


Figure 31. Landsat-1 MSS-7, November 8, 1972, Lake Nasser and Nile Valley, Egypt (UAR), with box limits of THIR and ESMR T_B comparison.

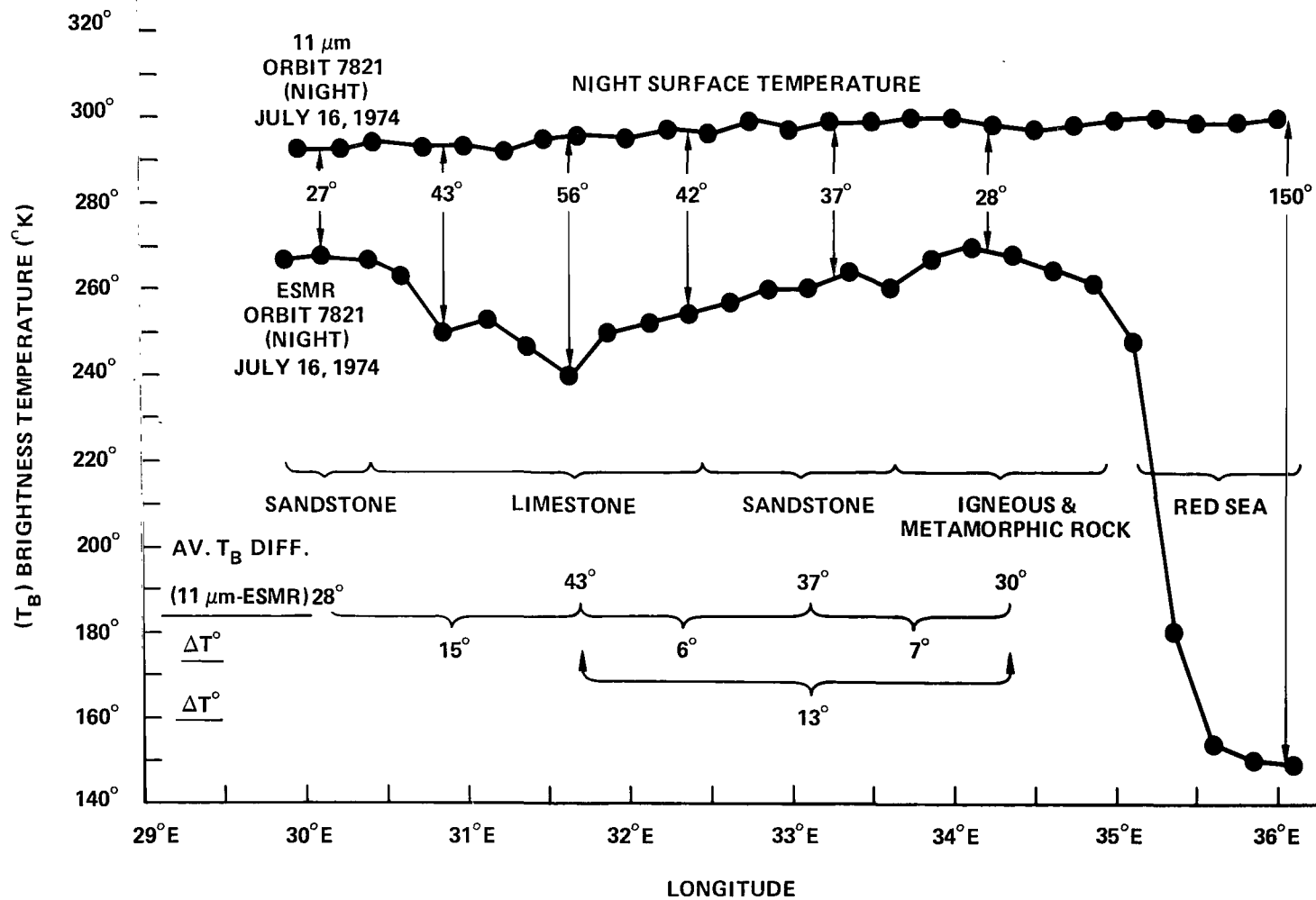


Figure 32. Comparison of Nimbus-5 THIR 11 μ m and ESMR, orbit 7821, July 16, 1974 (night), between 24°N and 24° 30'N, Egypt (UAR).

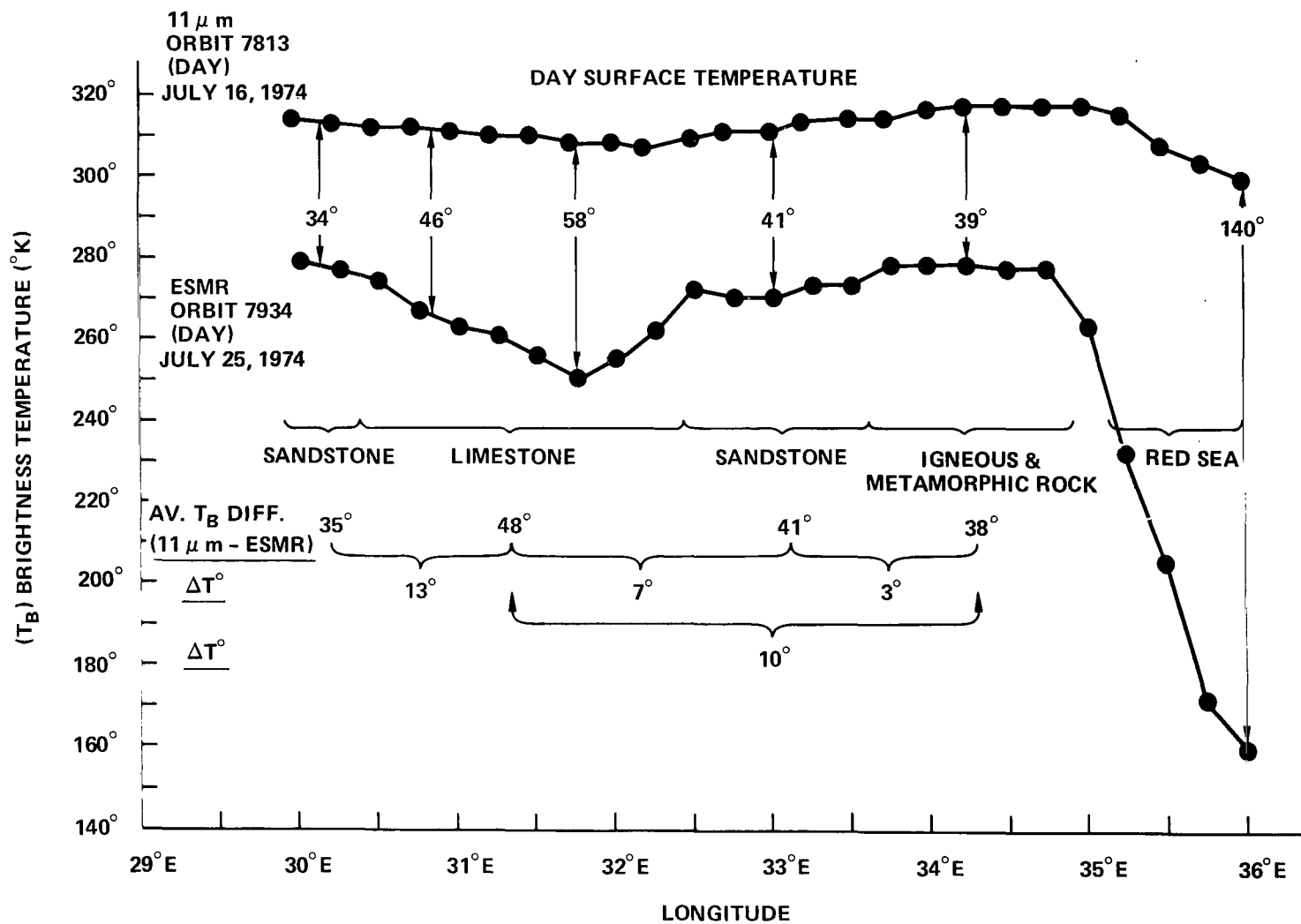


Figure 33. Comparison of Nimbus-5 THIR $11 \mu\text{m}$, orbit 7813, July 16, 1974 (day), and ESMR, orbit 7934, July 25, 1974 (day), between 24° N and $24^{\circ} 30'$ N, Egypt (UAR).

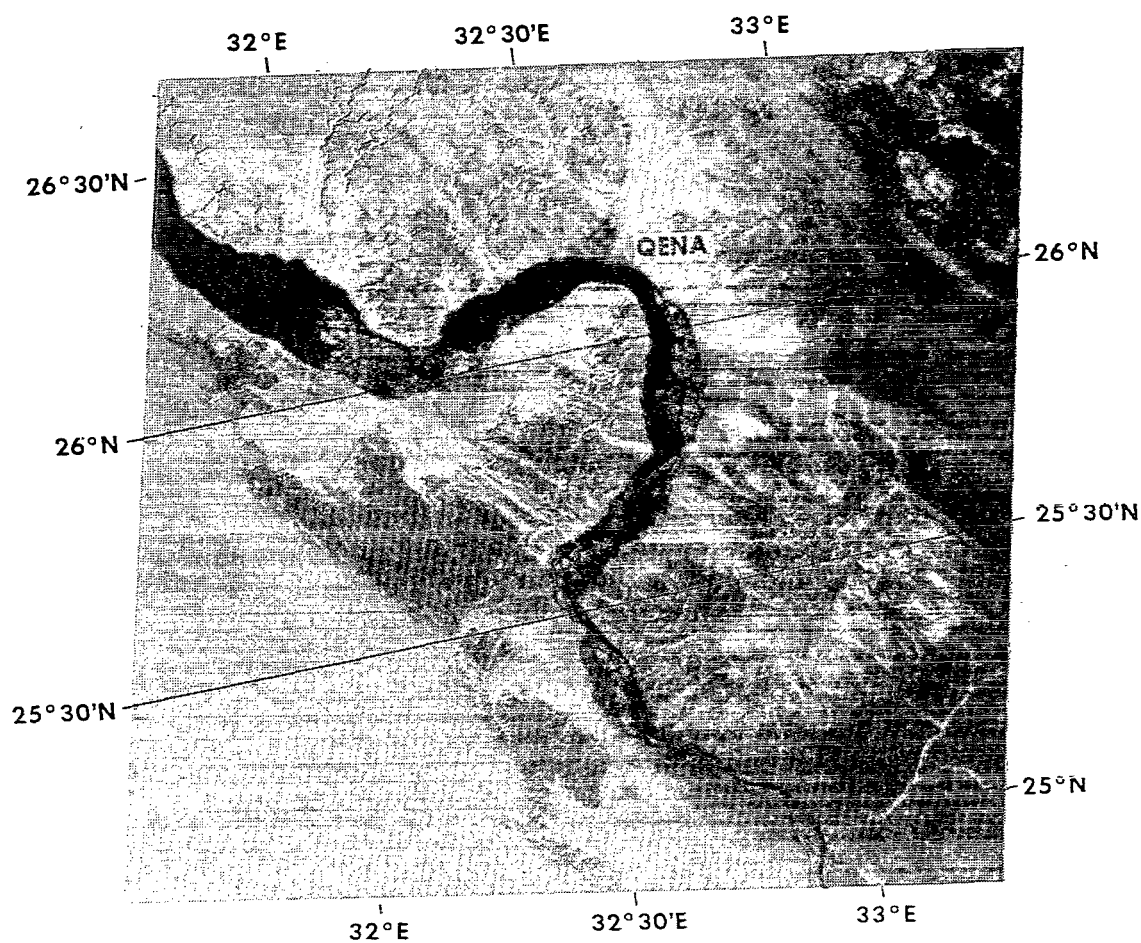


Figure 34. Landsat-1 MSS-7, November 9, 1972, Nile River (Qena) Egypt (UAR), with box limits of THIR and ESMR T_B comparison.

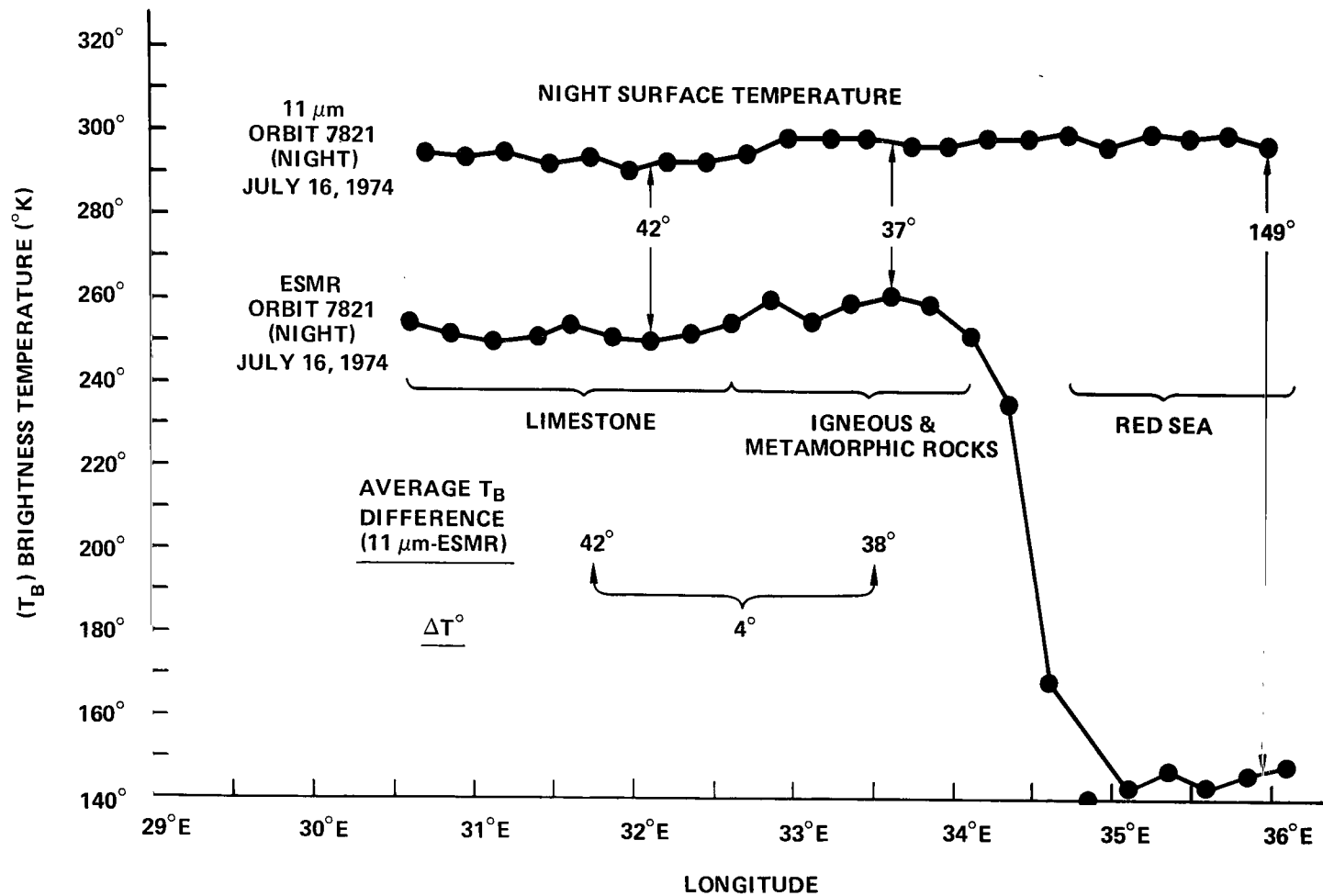


Figure 35. Comparison of Nimbus-5 THIR 11 μm and ESMR, orbit 7821, July 16, 1974 (night), between 25° 30'N and 26°N, Egypt (UAR).

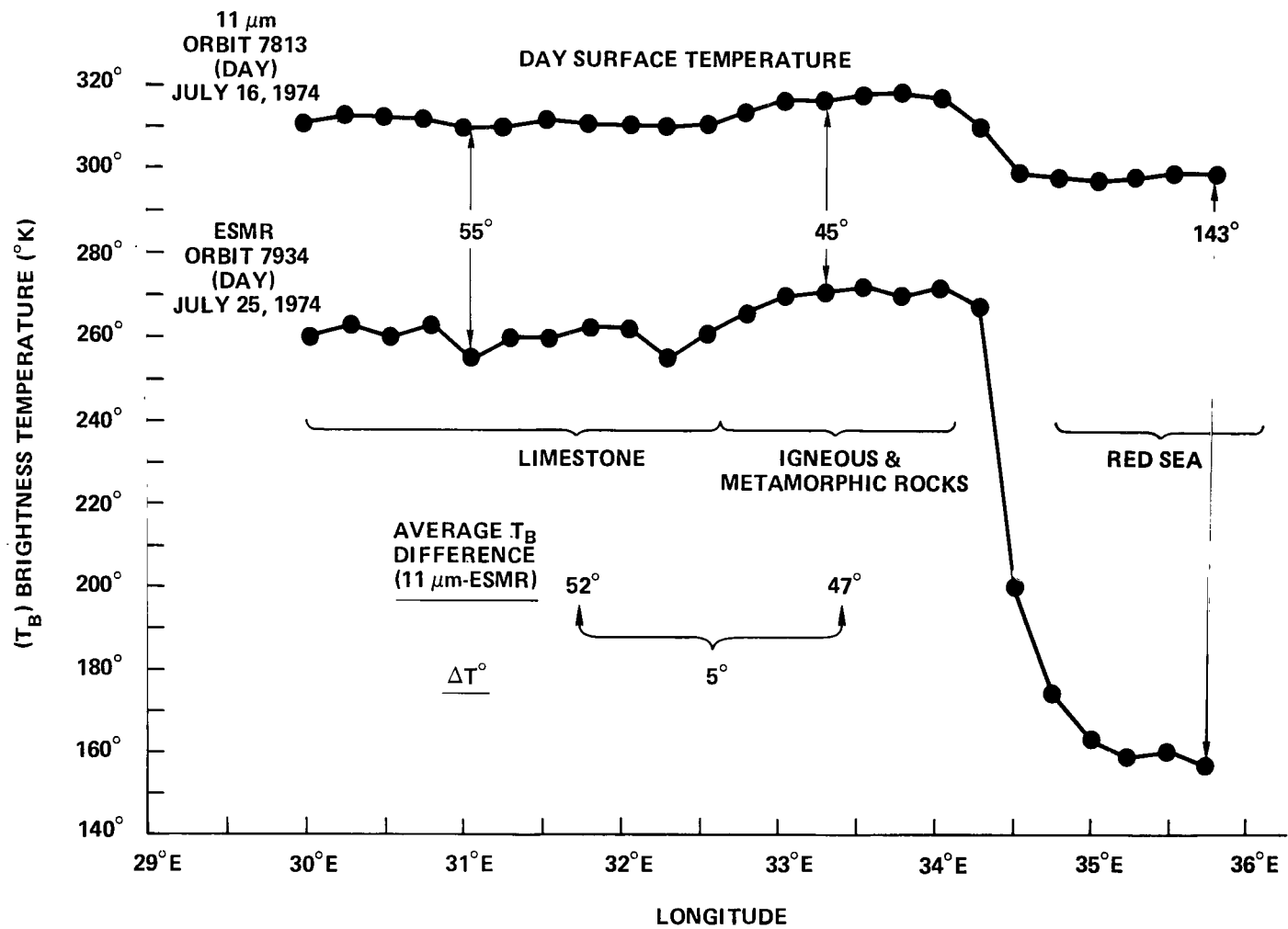


Figure 36. Comparison of Nimbus-5 THIR 11 μm , orbit 7813, July 16, 1974 (day), and ESMR, orbit 7934, July 25, 1974 (day), between 25 $^{\circ}$ 30'N and 26 $^{\circ}$ N, Egypt (UAR).

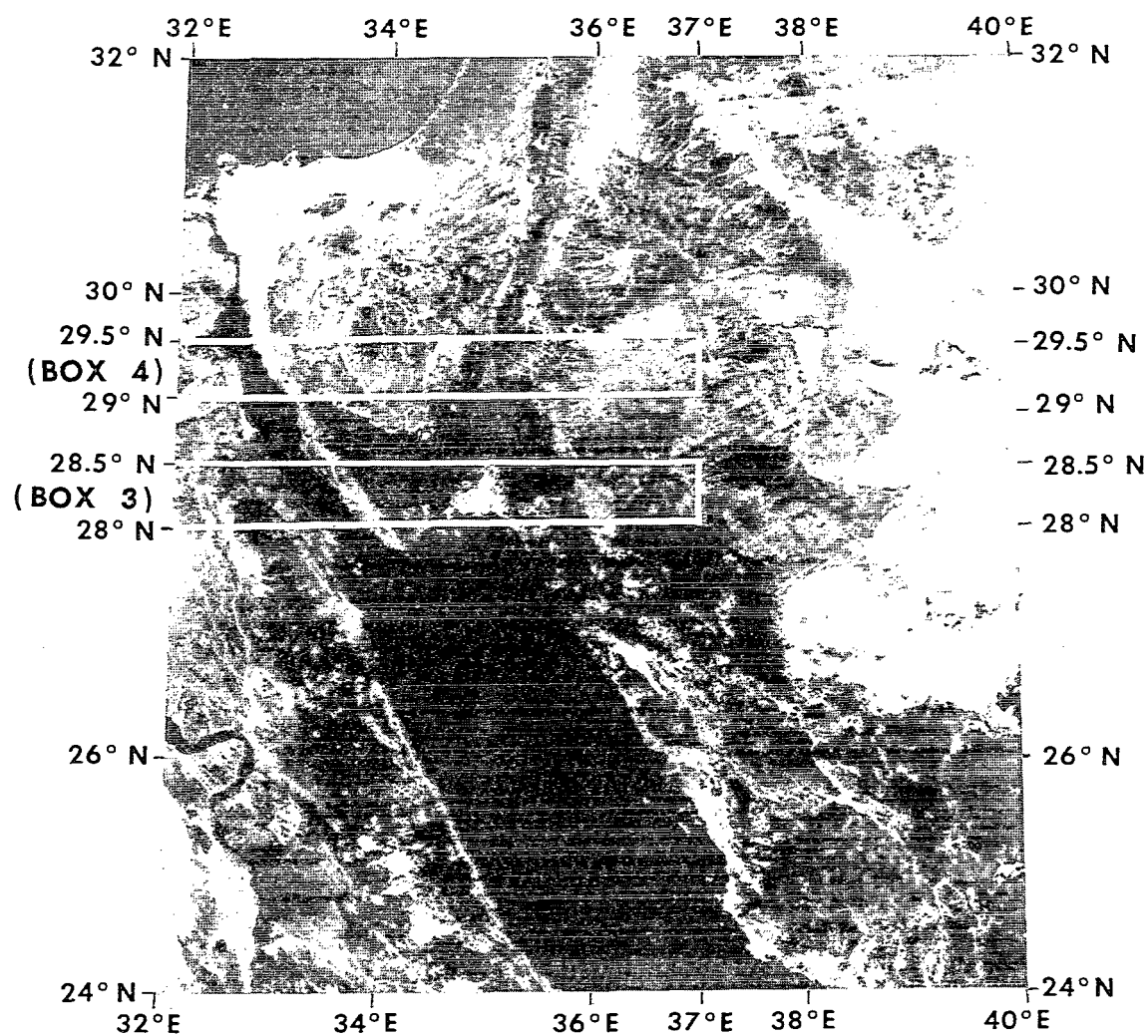


Figure 37. Landsat-1 MSS-5 and -7 composite photomosaic of all available cloud-free orbits over Sinai and Red Sea, with two boxes showing region of THIR and ESMR T_B comparison.

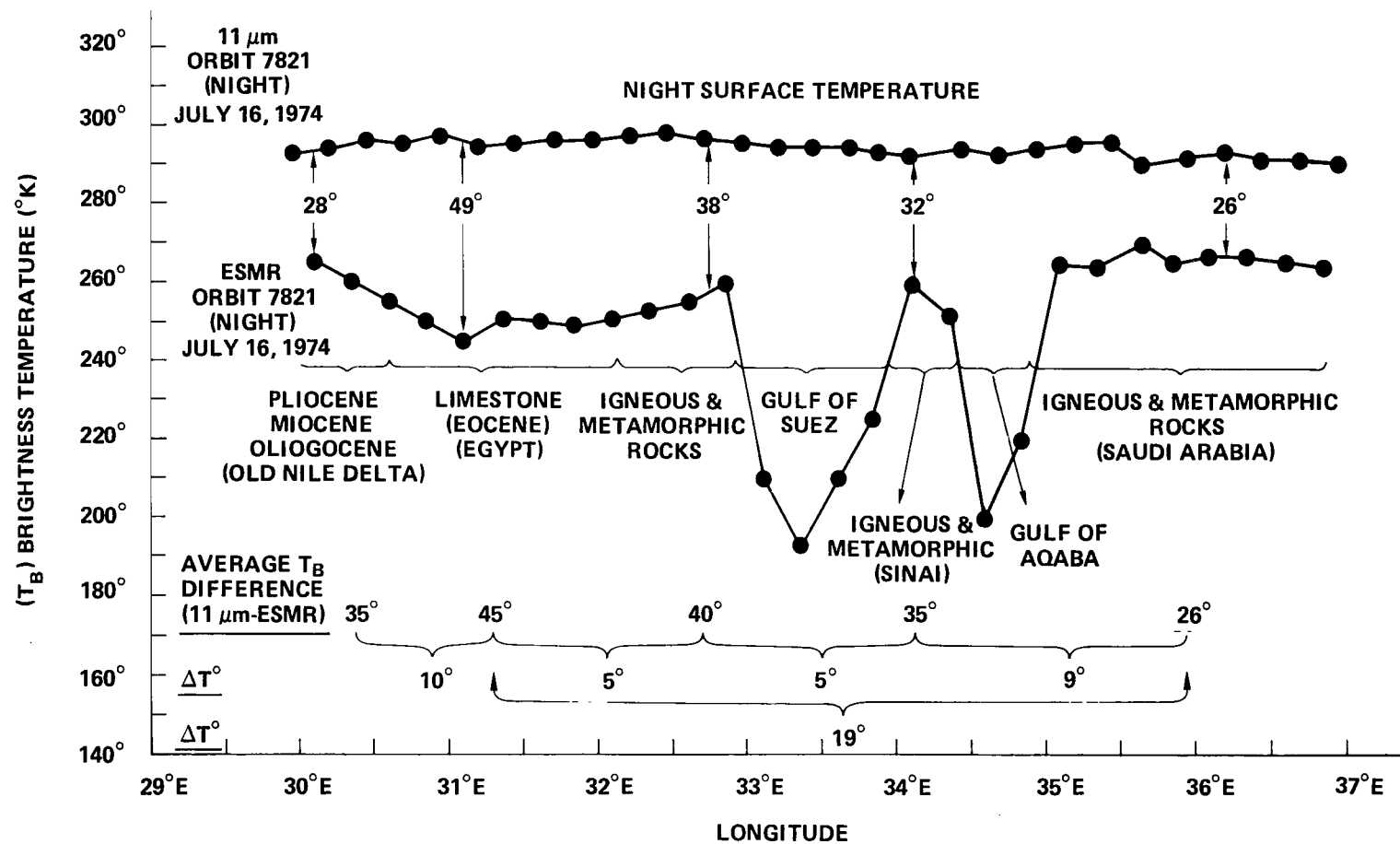


Figure 38. Comparison of Nimbus-5 THIR 11 μ m and ESMR, orbit 7821, July 16, 1974 (night), between 28 $^{\circ}$ N and 28 $^{\circ}$ 30'N, Egypt and Saudi Arabia.

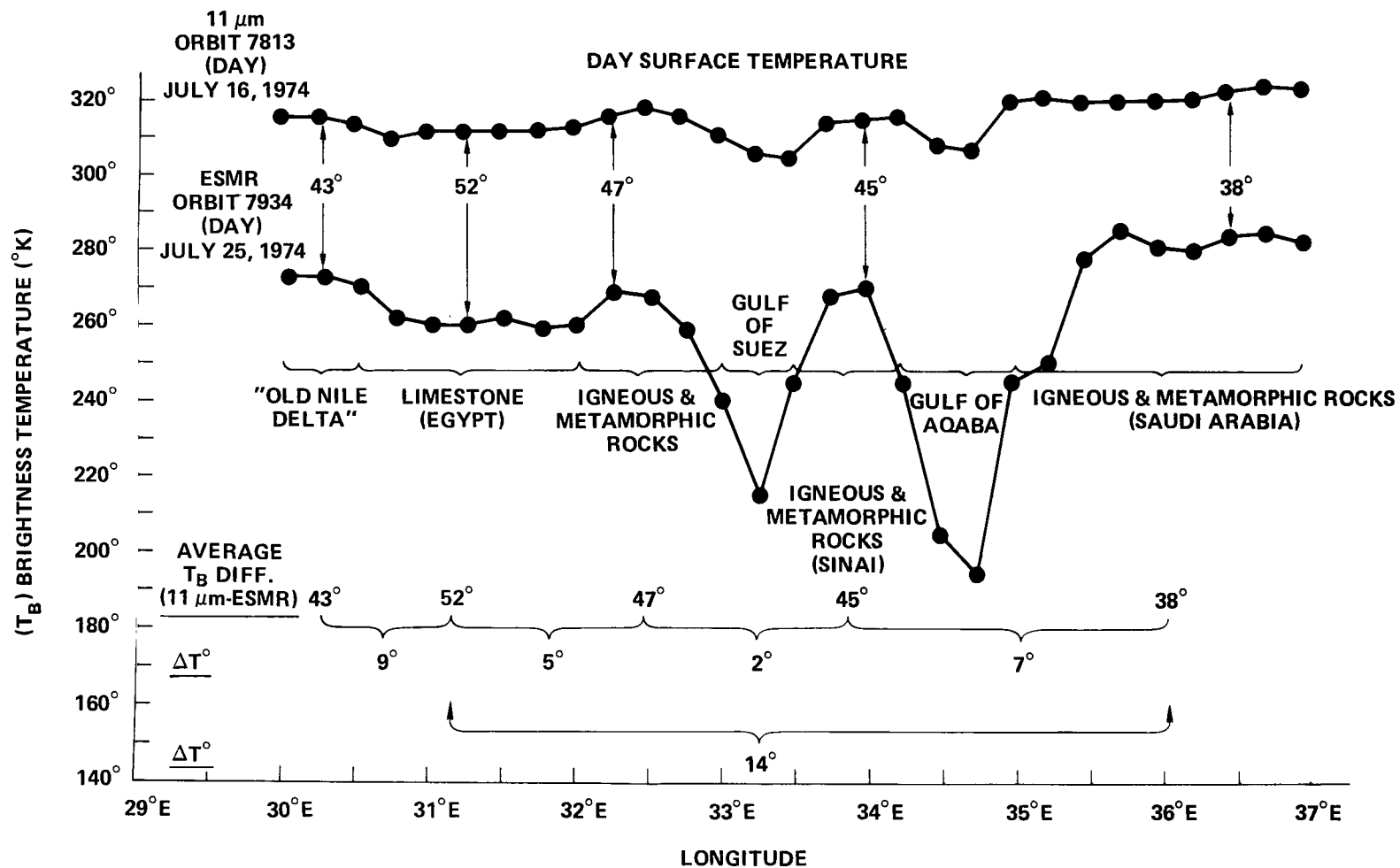


Figure 39. Comparison of Nimbus-5 THIR 11 μ m, orbit 7813, July 16, 1974 (day), and ESMR, orbit 7934, July 25, 1974 (day), between 28 $^{\circ}$ N and 28 $^{\circ}$ 30'N, Egypt and Saudi Arabia.

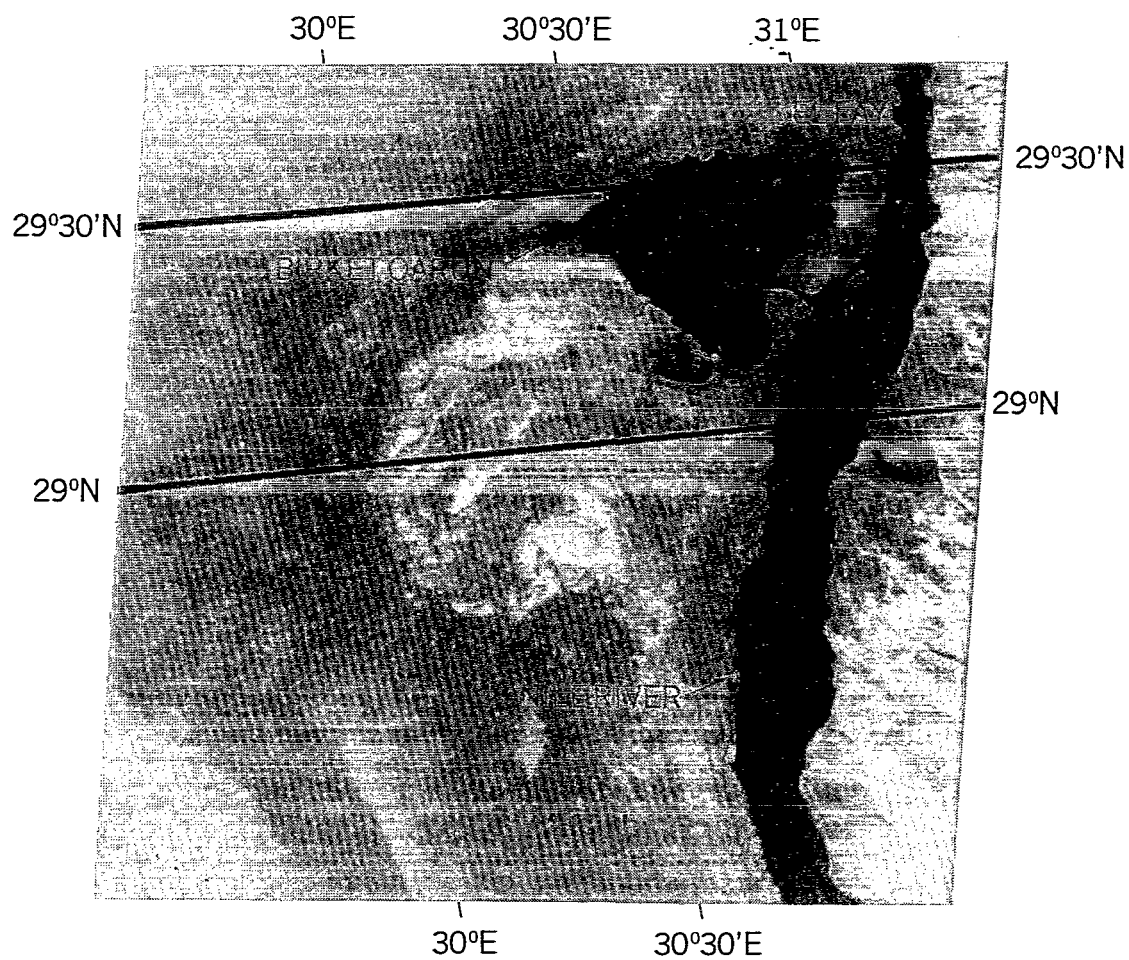


Figure 40. Landsat-2 MSS-7, May 10, 1973, El Fayum, Nile River Valley, Egypt (UAR), with box limits of THIR and ESMR T_B comparison.

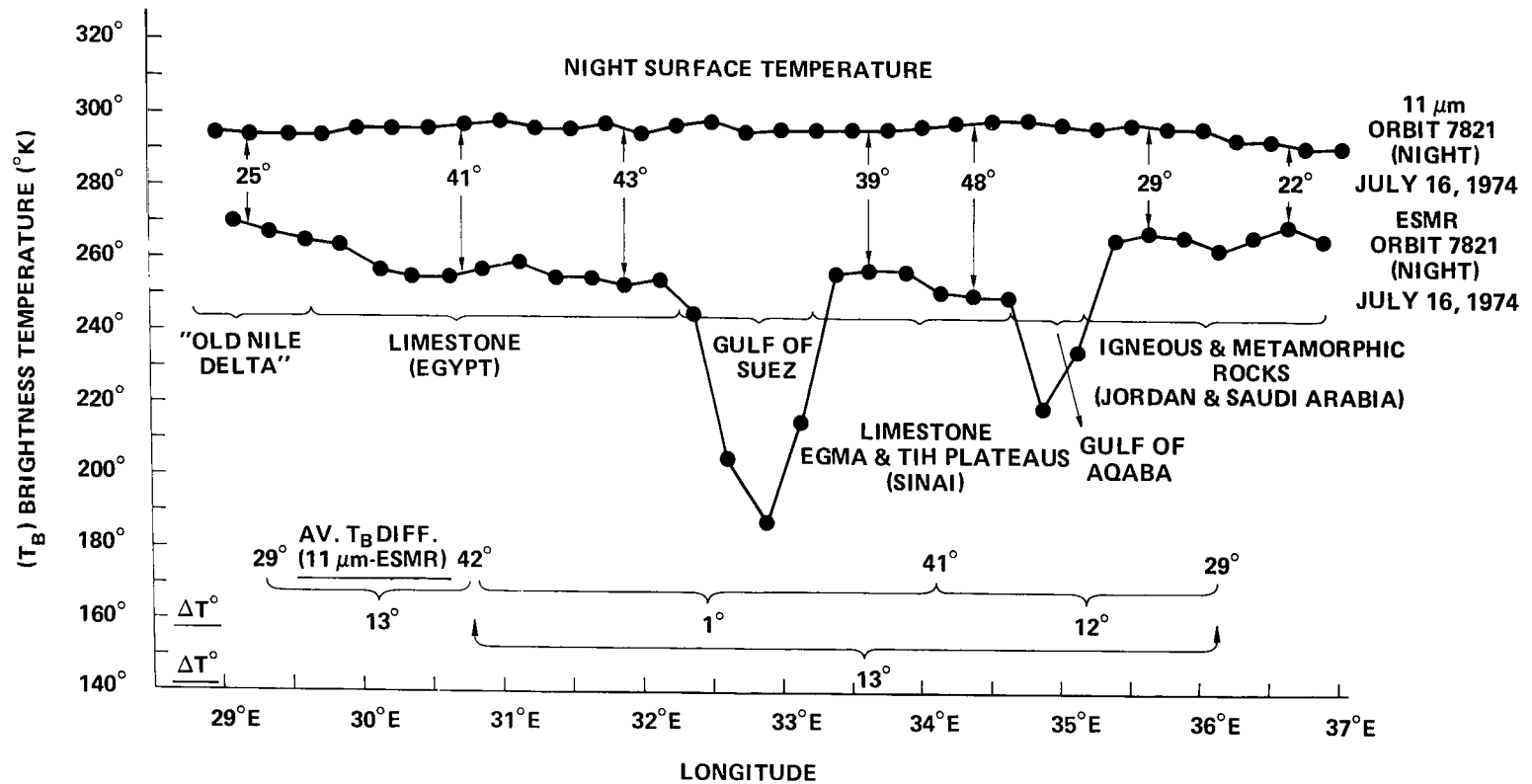


Figure 41. Comparison of Nimbus-5 THIR 11 μ m and ESMR orbit 7821, July 16, 1974 (night), between 29 $^{\circ}$ N and 29 $^{\circ}$ 30'N, Egypt, Jordan, and Saudi Arabia.

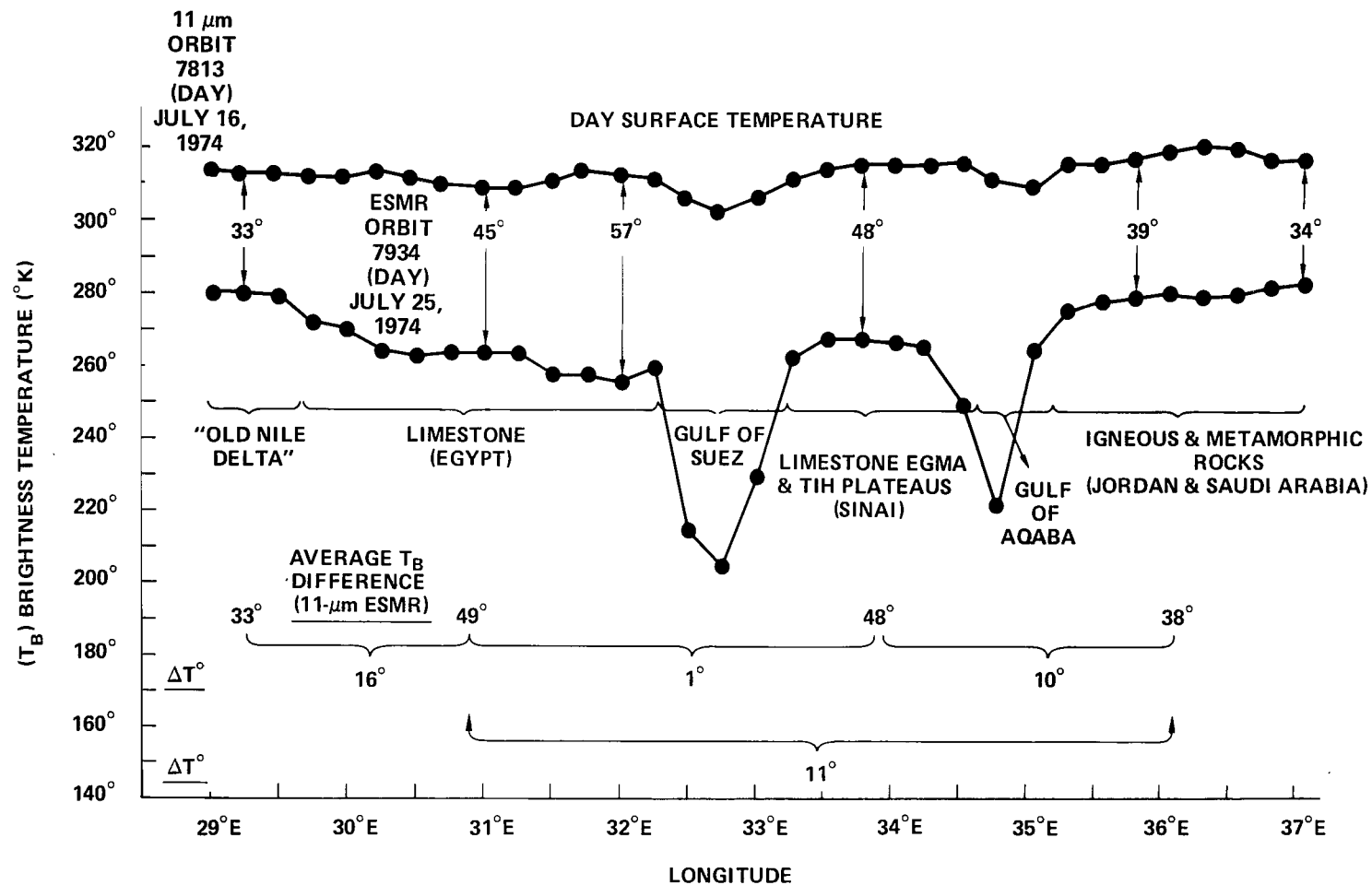


Figure 42. Comparison of Nimbus-5 THIR 11 μ m, orbit 7813, July 16, 1974 (day), and ESMR, orbit 7934, July 25, 1974 (day), between 29°N and 29° 30'N, Egypt, Jordan, and Saudi Arabia.

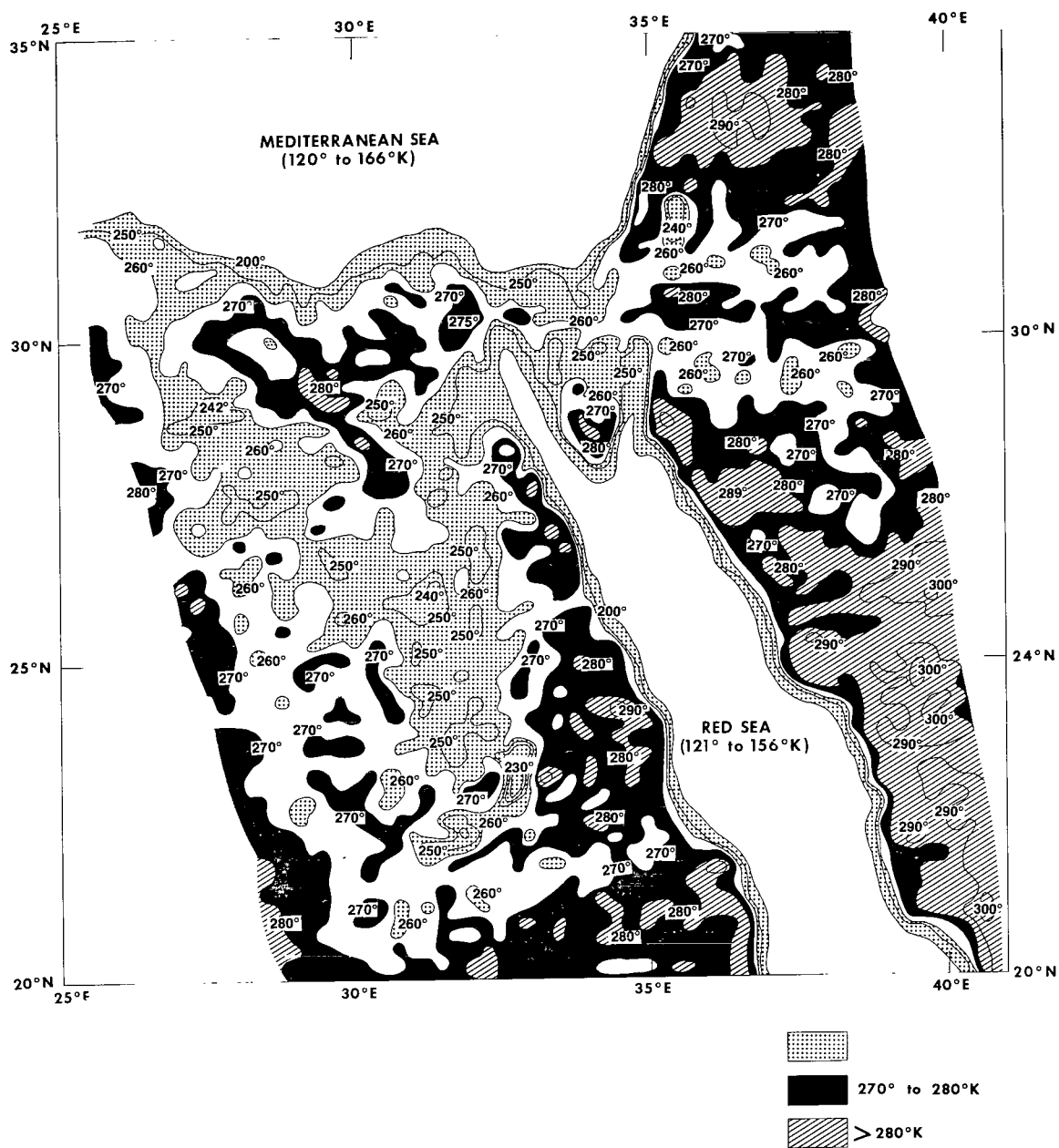


Figure 43. Nimbus-6 ESMR 37 GHz, orbit 618 (day), July 28, 1975, horizontal polarization; analysis of computer-produced grid print map (1:2 million, Mercator).

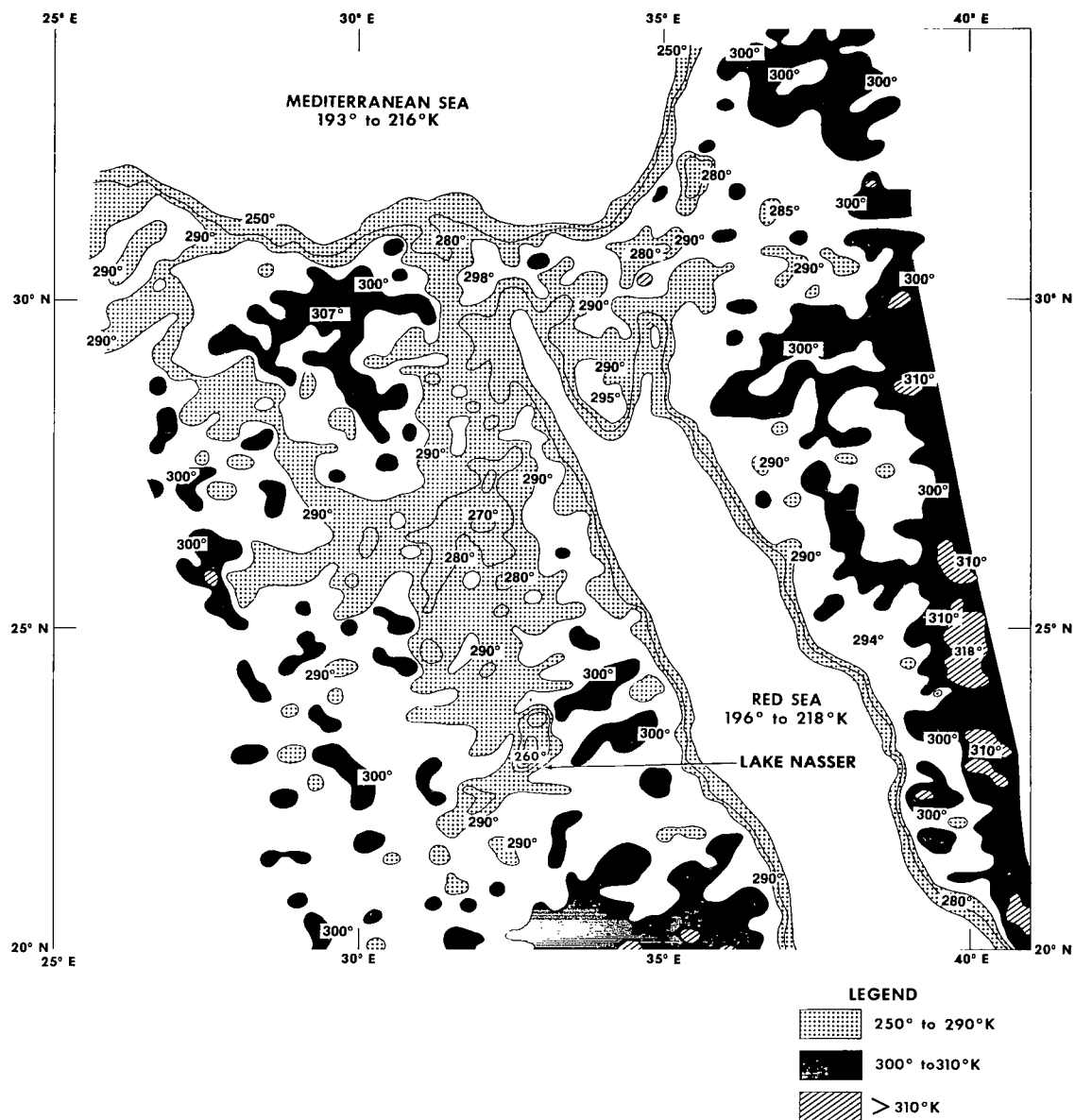


Figure 44. Nimbus-6 ESMR 37 GHz, orbit 618 (day), July 28, 1975, vertical polarization; analysis of computer-produced grid print map (1:2 million, Mercator).

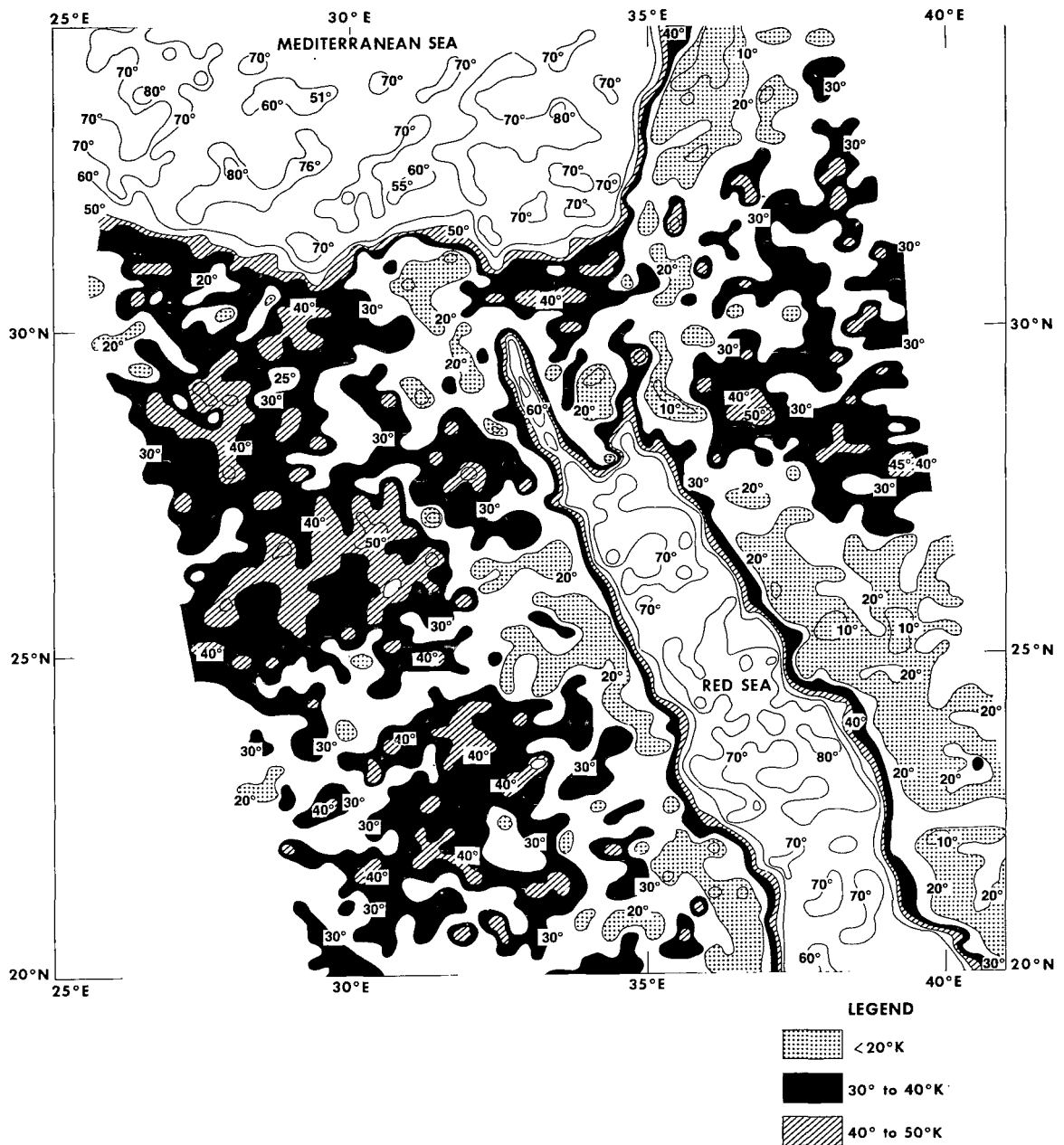
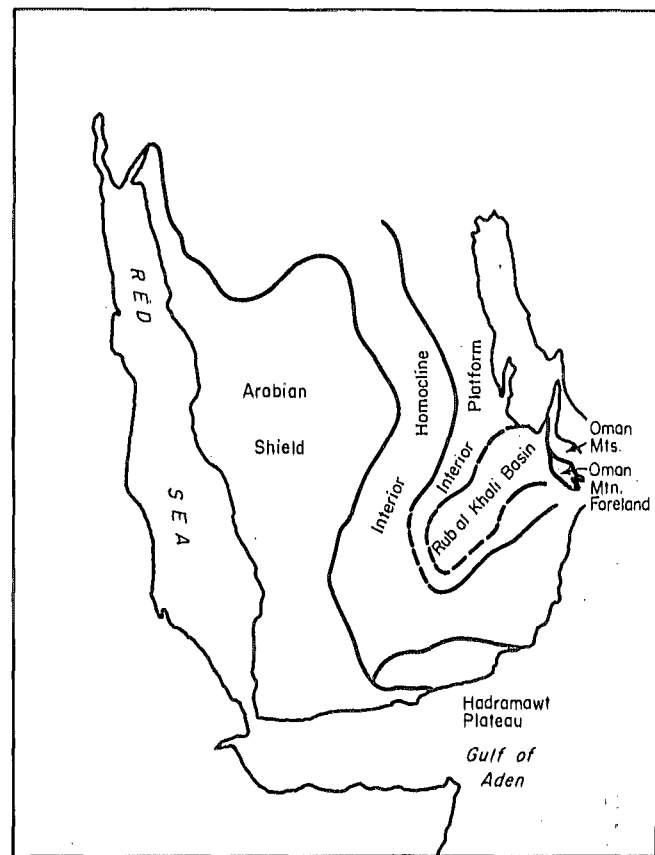


Figure 45. Nimbus-6 ESMR 37 GHz, orbit 846 (day), August 14, 1975, vertical minus horizontal polarization; analysis of computer-produced grid print map (1:2 million, Mercator).



(a)



(b)

Figure 46. a. U.S. Air Force DMSP visual picture, orbit 4752, February 14, 1975, 0837Z, (2-mile resolution); b. map of Saudi Arabia indicating major geological features (U.S. Geological Survey, 1966).



Figure 49. Nimbus-5 ESMR 19.35 GHz,
orbit 3780 (night), September 18, 1975,
facsimile picture.

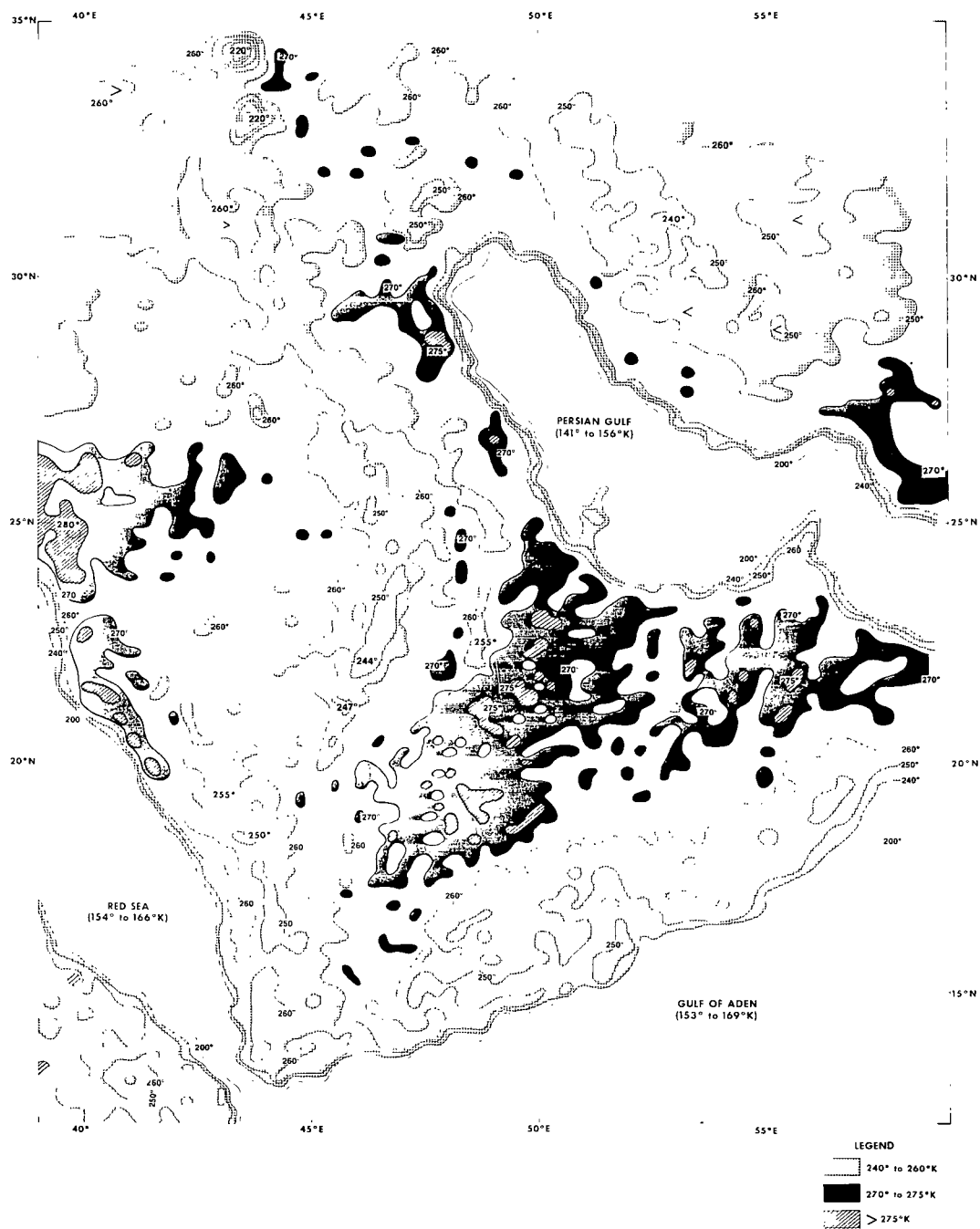


Figure 50. Nimbus-5 ESMR 19.35 GHz, orbit 3779 (night), September 18, 1973, horizontal polarization; analysis of computer-produced grid print map (1:2 million, Mercator).

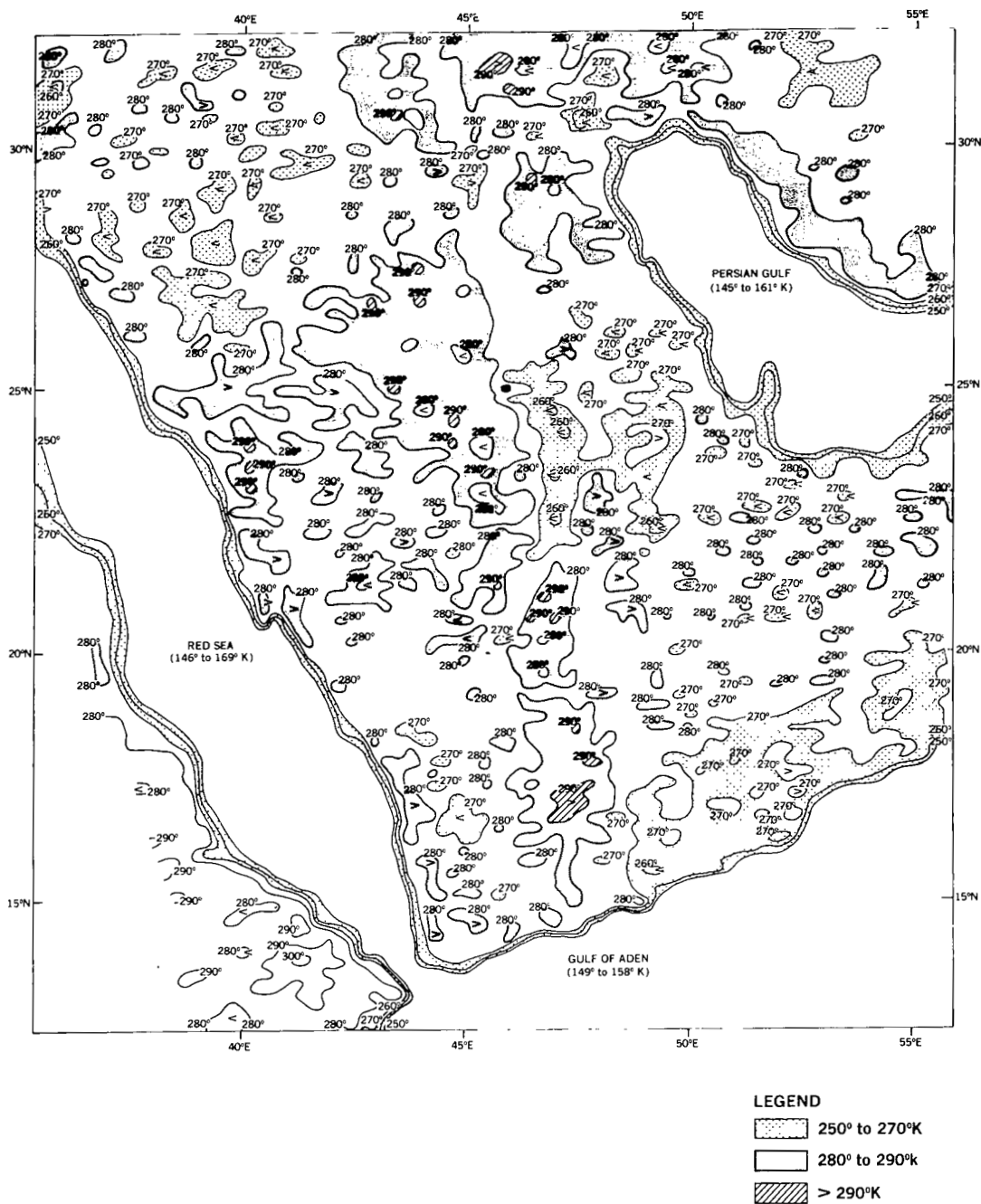


Figure 51. Nimbus-5 ESMR 19.35 GHz, orbit 3853 (day), September 24, 1973, horizontal polarization; analysis of computer-produced grid print map (1:2 million, Mercator).

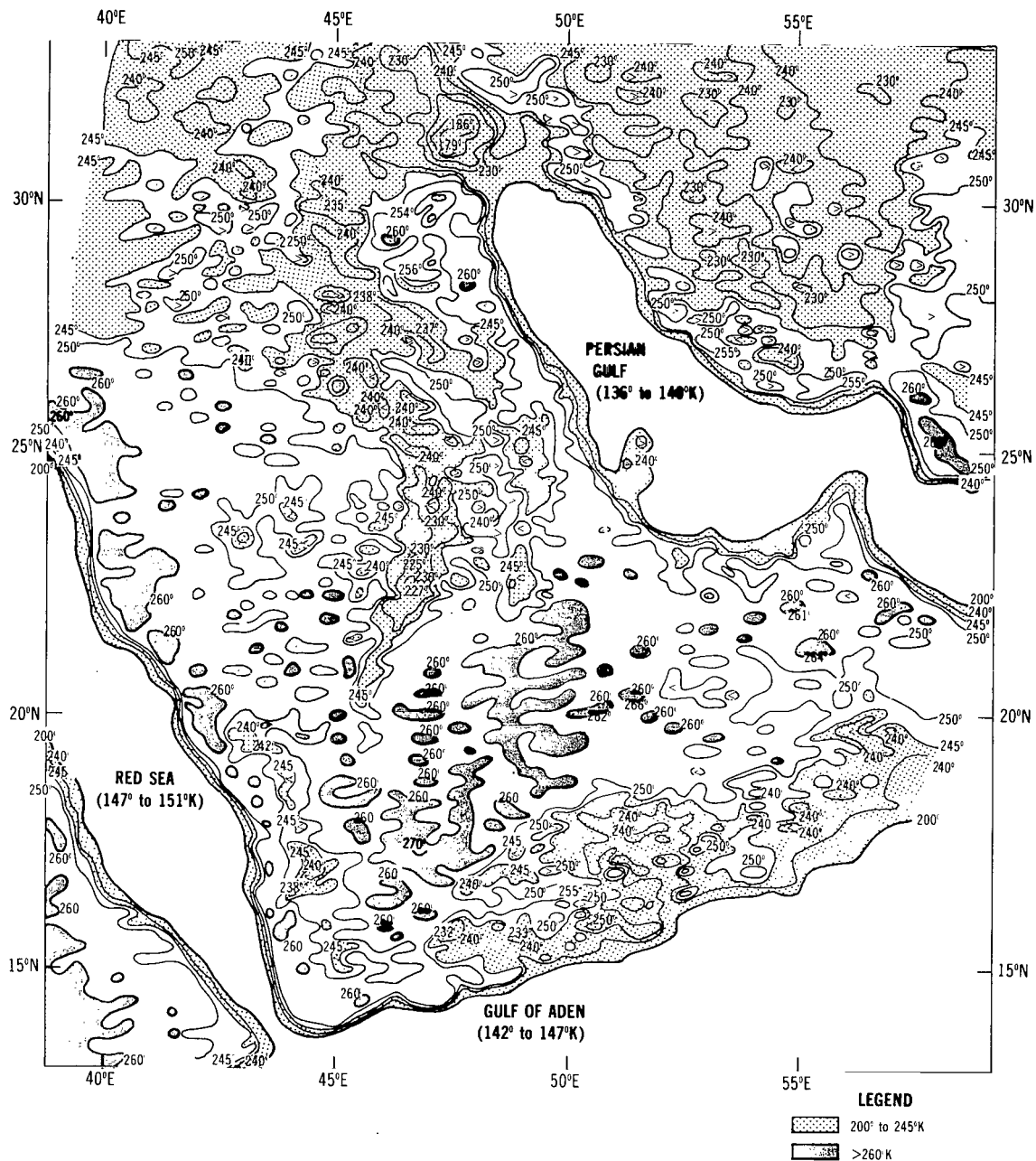


Figure 52. Nimbus-5 ESMR 19.35 GHz, orbit 10974 (night), March 8, 1975, horizontal polarization, analysis of computer-produced grid print map (1:2 million, Mercator).

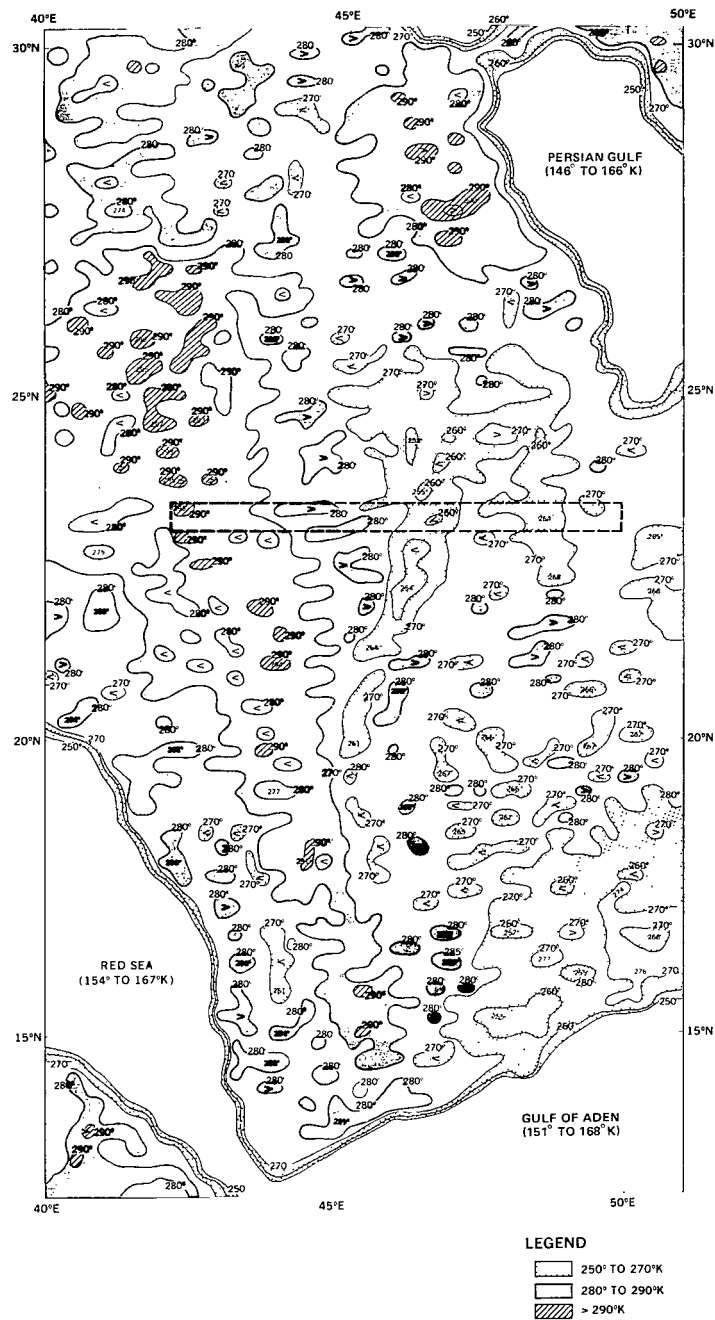


Figure 53. Nimbus-5 ESMR 19.35 GHz, orbit 7813 (day), July 16, 1974, horizontal polarization; analysis of computer-produced grid print map (1:2 million, Mercator) (dashed box indicates area of cross section shown in figure 55).

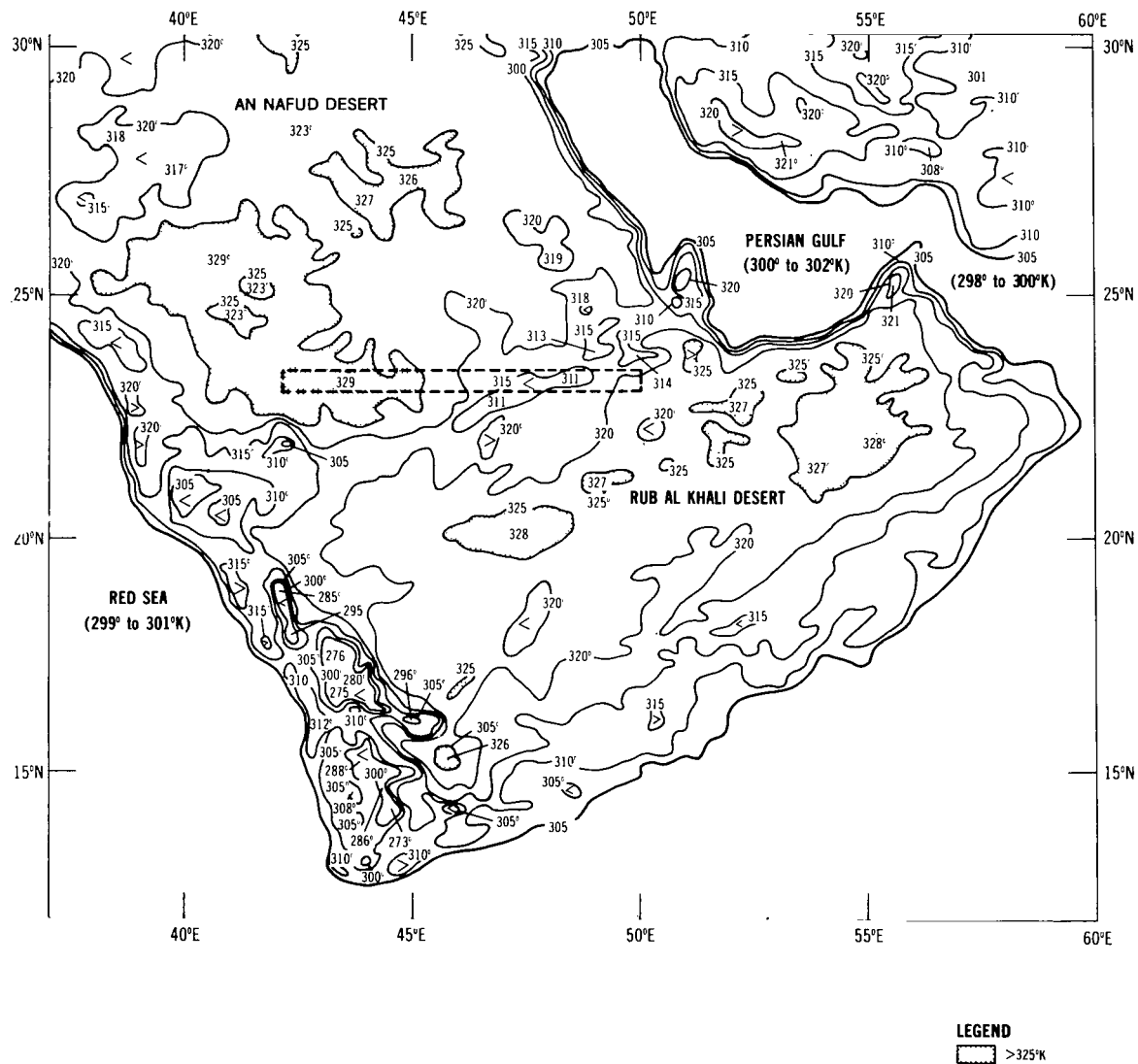


Figure 54. Nimbus-5 THIR 11 μ m, orbit 7813 (day), July 16, 1974, analysis of computer-produced grid print map (1:2 million, Mercator) (dashed box indicates area of cross section shown in figure 55).

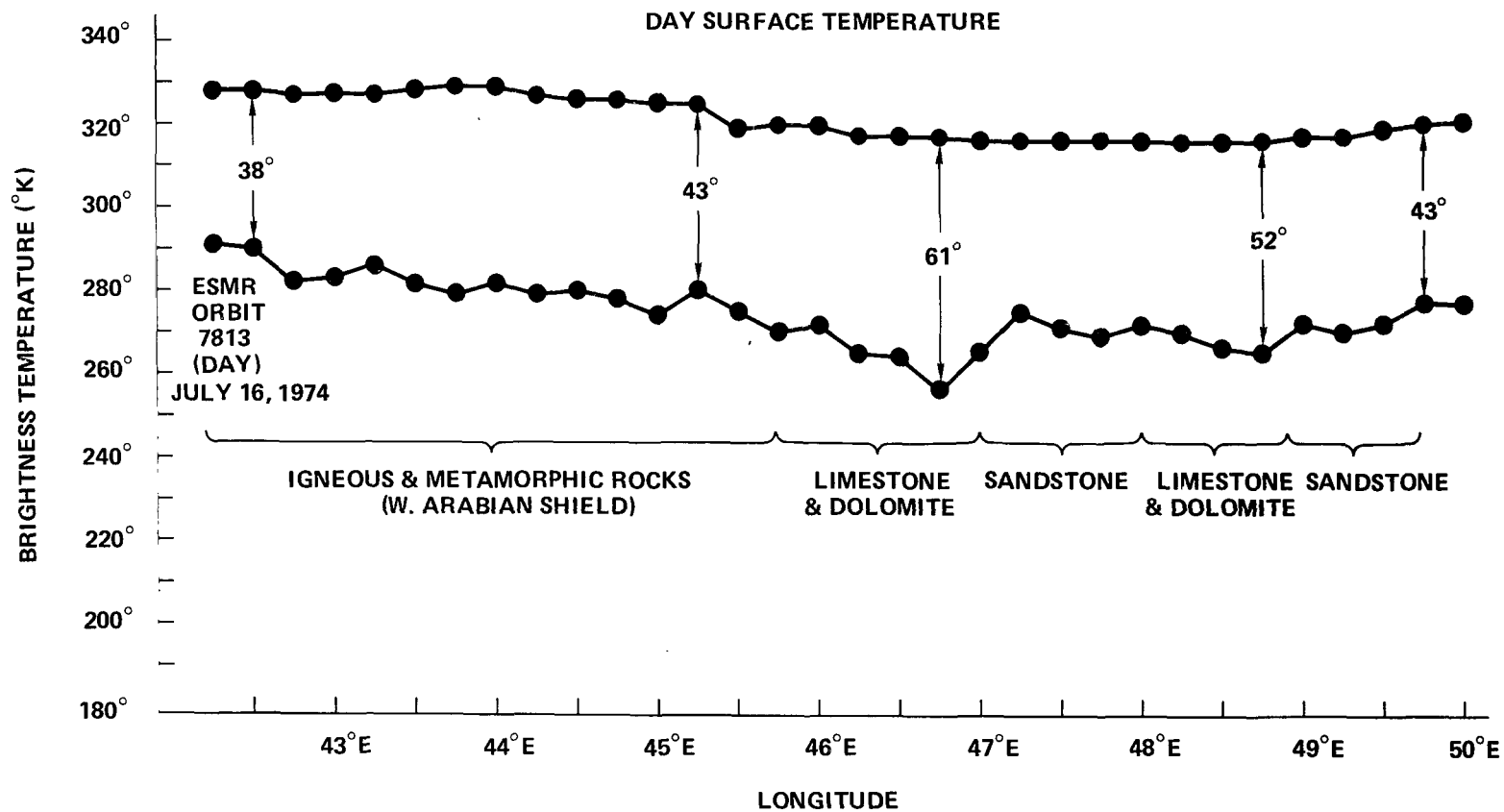


Figure 55. Comparison of Nimbus-5 THIR $11\ \mu\text{m}$ and ESMR, orbit 7813 (day), between 23° and $23^\circ 30'N$, Saudi Arabia.

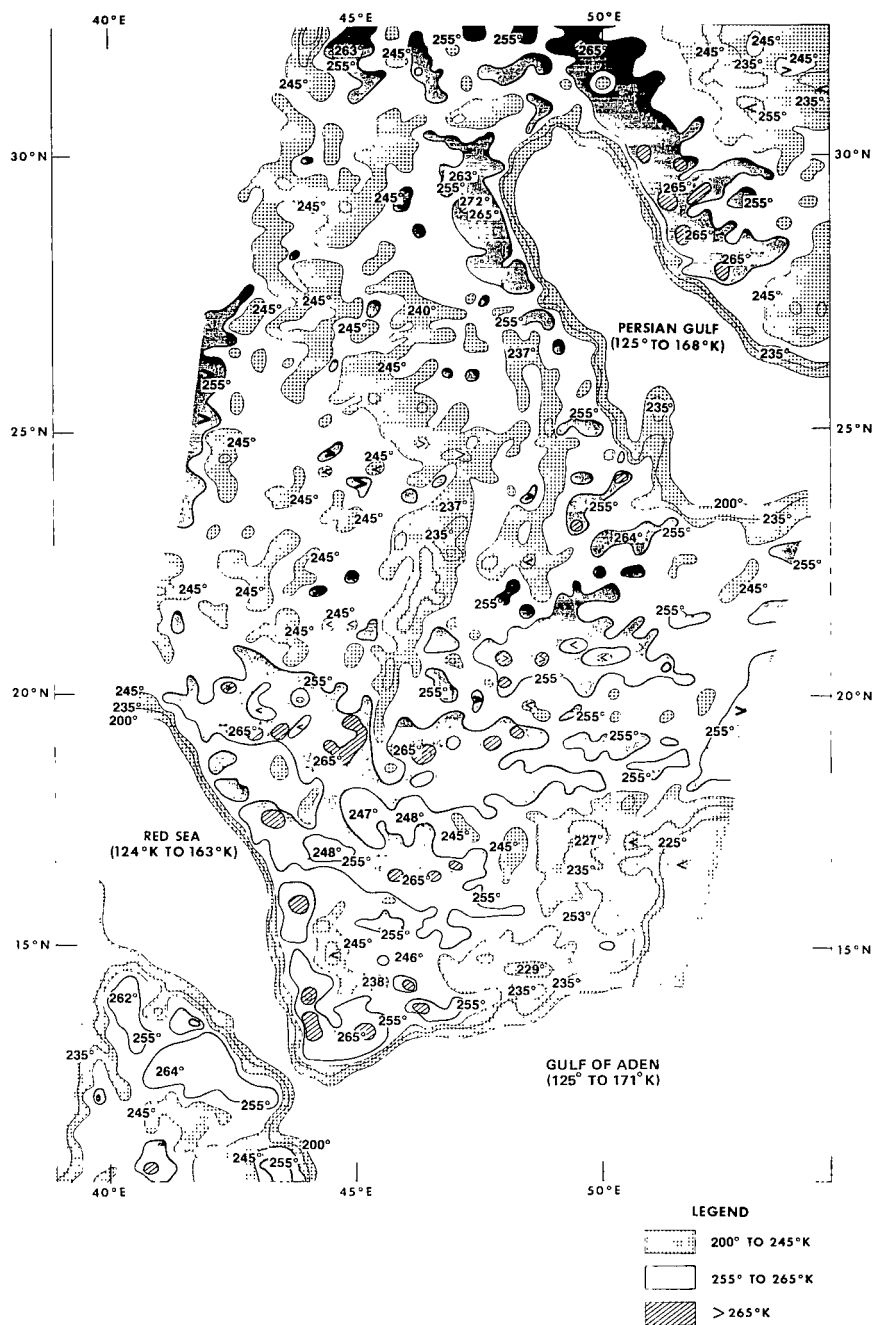


Figure 56. Nimbus-6 ESMR 37 GHz, orbit 880 (night), August 16, 1975, horizontal polarization; analysis of computer-produced grid print map (1:2 million, Mercator).

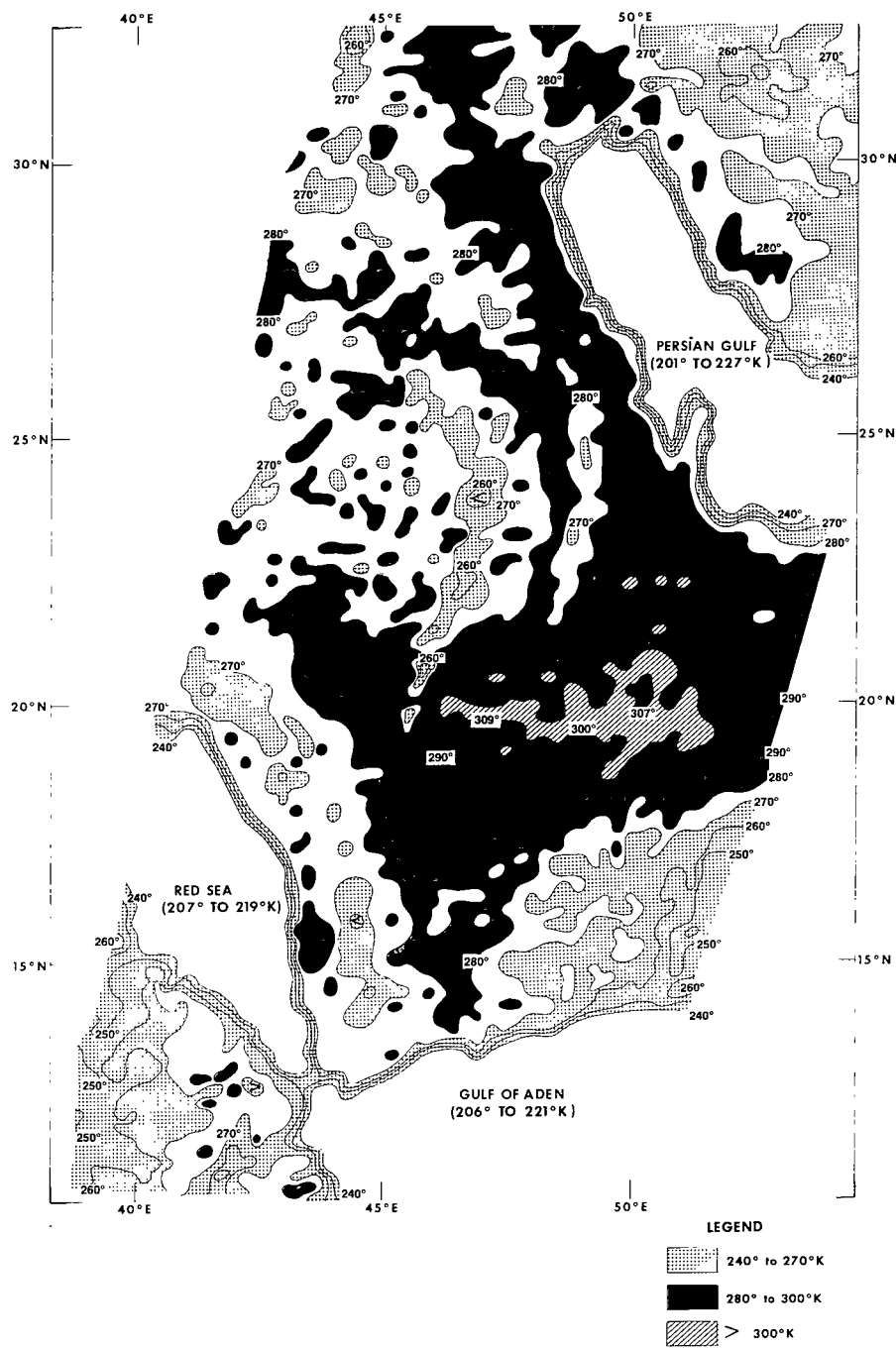


Figure 57. Nimbus-6 ESMR 37 GHz, orbit 880 (night), August 16, 1975, vertical polarization; analysis of computer-produced grid print map (1:2 million, Mercator).

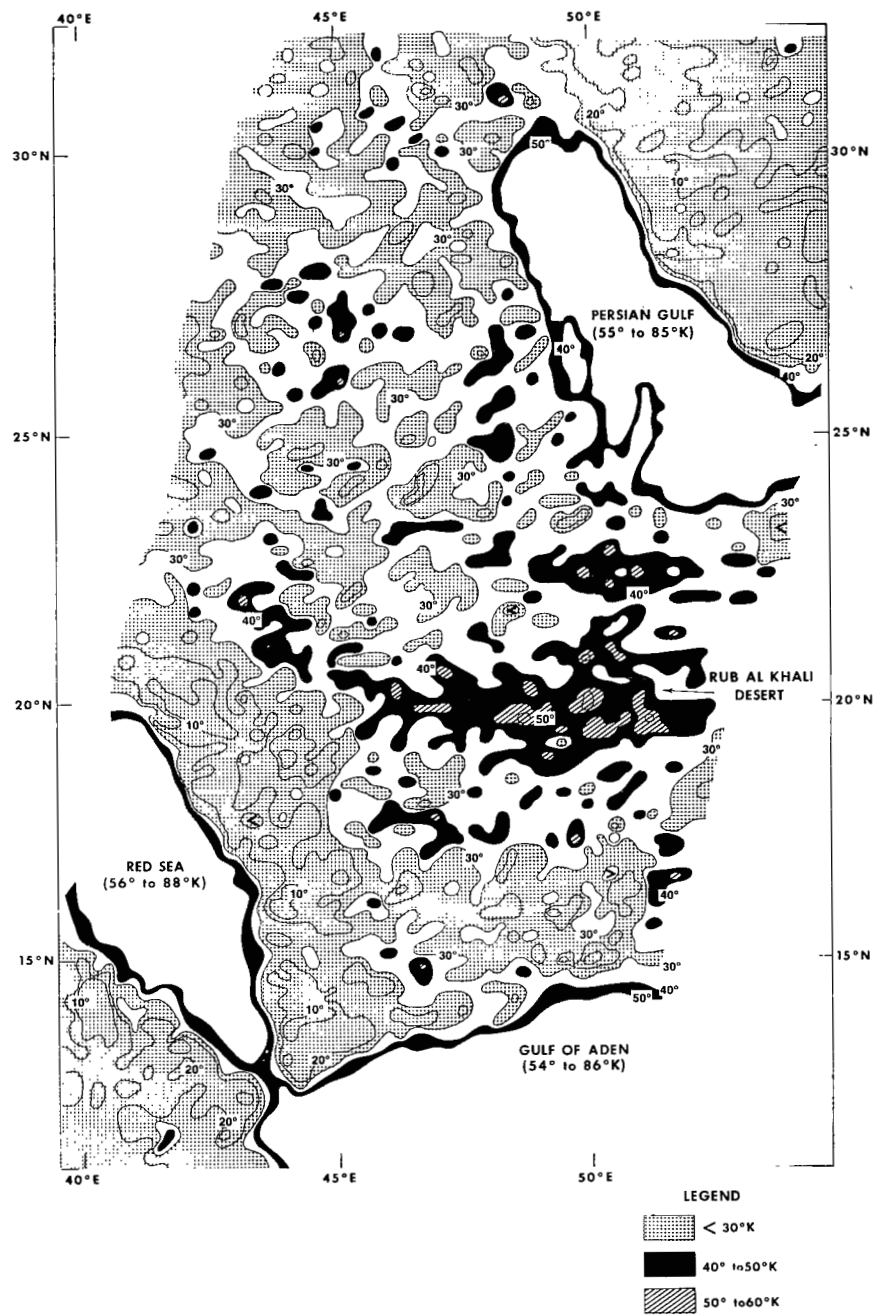


Figure 58. Nimbus-6 ESMR 37 GHz, orbit 880 (night), August 16, 1975, vertical minus horizontal polarization; analysis of computer-produced grid print map (1:2 million, Mercator).

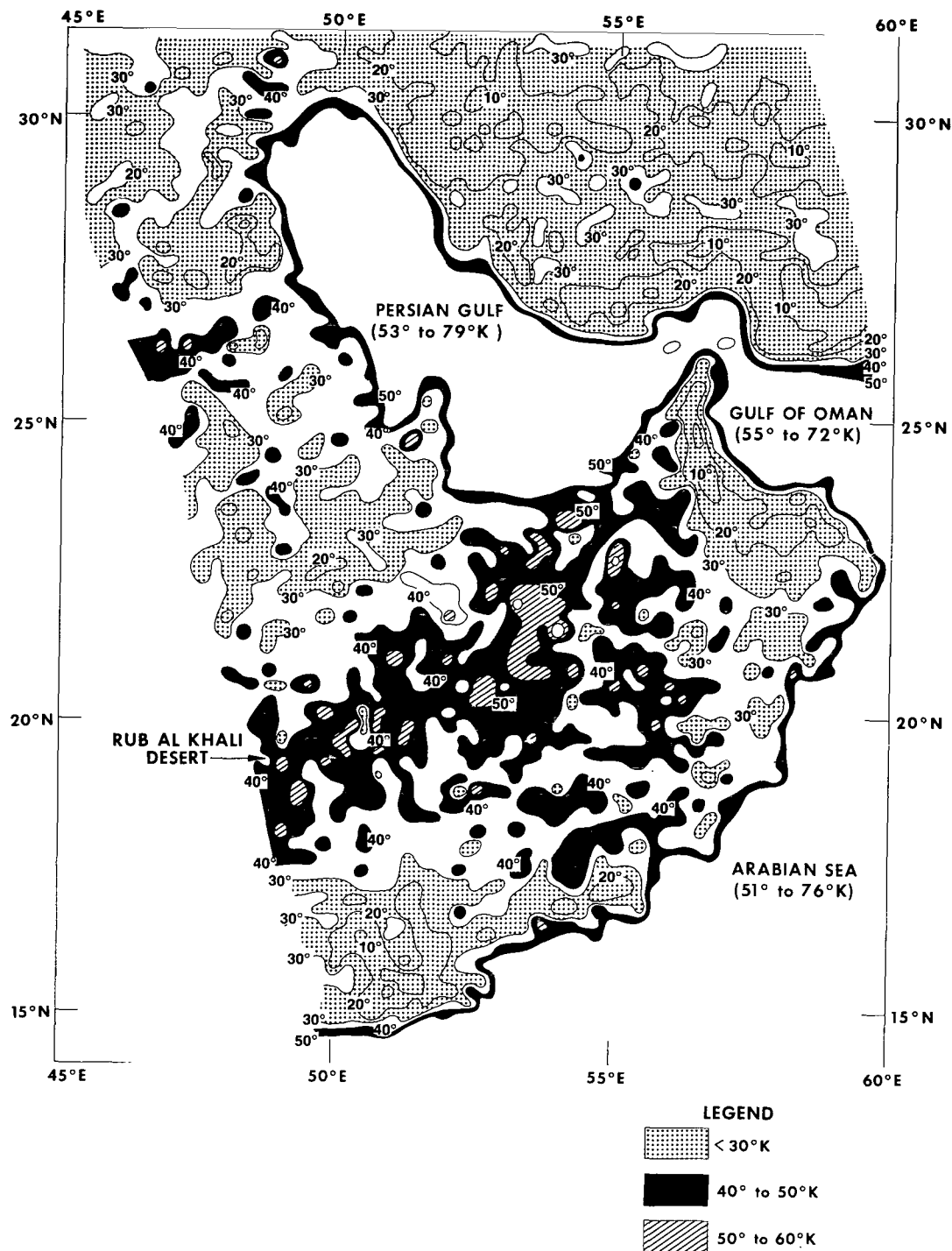


Figure 59. Nimbus-6 ESMR 37 GHz, orbit 738 (day), August 6, 1975, vertical minus horizontal polarization; analysis of computer-produced grid print map (1:2 million, Mercator).

REFERENCES

1. Schnapf, A., "TIROS 1, 2 and 3 - Design and Performance," *Aerospace Engineering*, **21**, (6), 1962, pp. 32-43.
2. World Meteorological Organization, "Reduction and Use of Data Obtained by Meteorological Satellites," Tech. Note 49, 1963, p. 59.
3. Nordberg, W. and R. E. Samuelson, "Terrestrial Features Observed by the High Resolution Infrared Radiometer," *Observations from the Nimbus 1 Meteorological Satellite*, NASA SP-89, 1965, pp. 37-41.
4. Lowman, P. D. and J. A. McDivitt, *Terrain Photography on the Gemini IV Mission: Preliminary Report*, NASA TN D-3982, 1967, p. 15.
5. Pouquet, J., *Remote Detection of Terrain Features from Nimbus 1 High Resolution Infrared Radiometer Nighttime Measurements*, NASA TN D-4603, 1968, p. 8.
6. Pouquet, J. and E. Raschke, *A Preliminary Study of the Detection of Geomorphological Features over Northeast Africa by Satellite Radiation Measurements in the Visible and Infrared*, NASA TN D-4648, 1968, p. 16.
7. Merifield, P. M. (ed.), J. Cronin, L. L. Foshee, S. J. Gawarecki, J. T. Neal, R. E. Stevenson, R. O. Stone, and R. S. Williams, Jr., "Satellite Imagery of the Earth," *Photogrammetric Engineering*, **35**, (7), 1969, pp. 654-668.
8. Sabatini, R., G. A. Rabchevsky, and J. Sisala, *Nimbus Earth Resources Observations*, Tech. Report #2 prepared for Goddard Space Flight Center by Allied Research Associates, Inc., Concord, Mass., 1971, p. 256.
9. Rowan, L. C., P. H. Wetlaufer, A. F. H. Goetz, F. C. Billingsley, and J. H. Stewart, *Discrimination of Rock Types and Detection of Hydrothermally Altered Areas in South-Central Nevada by the Use of Computer-Enhanced ERTS Images*, Geological Survey Professional Paper 883, 1974, p. 35.
10. Blodget, H. W., G. F. Brown, and J. G. Moik, *Geological Mapping in Northwestern Saudi Arabia Using Landsat-Multispectral Techniques*, NASA TM X-70961 1975, p. 21.
11. "The Nimbus 5 Spacecraft System," *Nimbus 5 User's Guide*, ERTS/Nimbus Project, Goddard Space Flight Center, 1972, pp. 1-10.

12. "Nimbus 6 Spacecraft System," *Nimbus 6 User's Guide*, Landsat/Nimbus Project, Goddard Space Flight Center, 1975, pp. 1-10.
13. Wilheit, T. T., "The Electrically Scanning Microwave Radiometer (ESMR) Experiment," *The Nimbus 5 User's Guide*, R. R. Sabatini, ed., ERTS/Nimbus Project, Goddard Space Flight Center, 1972, pp. 59-105.
14. Allison, L. J., E. B. Rodgers, T. T. Wilheit, and R. W. Fett, "Tropical Cyclone Rainfall as Measured by the Nimbus 5 Electrically Scanning Microwave Radiometer," *Bulletin of the American Meteorological Society*, **55**, (9), 1974, pp. 1074-1089.
15. Allison, L. J., E. B. Rodgers, T. T. Wilheit, and R. Wexler, *A Multisensor Analysis of Nimbus 5 Data Recorded on January 22, 1973*, NASA TN D-7911, 1975, p. 43.
16. Wilheit, T. T., J. S. Theon, W. E. Shenk, L. J. Allison, and E. B. Rodgers, "Meteorological Interpretations of the Images from the Nimbus 5 Electrically Scanned Microwave Radiometer," *Journal of Applied Meteorology*, **15**, (2), 1976, pp. 166-172.
17. Kidder, S. Q., "Tropical Oceanic Precipitation Frequency from Nimbus 5 Microwave Data," Atmos. Science Paper 248, Colorado State University, Ft. Collins, Colorado, 1976, p. 50.
18. Wilheit, T. T., "The Electrically Scanning Microwave Radiometer (ESMR) Experiment," *The Nimbus 6 User's Guide*, Landsat/Nimbus Project, Goddard Space Flight Center, 1975, pp. 87-108.
19. Wilheit, T. T., M. S. U. Rao, T. C. Chang, E. B. Rodgers, and J. S. Theon, *A Satellite Technique for Quantitatively Mapping Rainfall Rate Over the Oceans*, NASA TM X-70904, 1975, p. 28.
20. Sabatini, R. R., *Sea-Surface Wind Speed Estimates from the Nimbus 5 ESMR*, Final Report, EPRF Tech. Report 3-75, Earth Satellite Corp., Washington, D. C., 1975, p. 55.
21. Schmugge, T. J., A. Rango, L. J. Allison, and T. T. Wilheit, *Hydrologic Applications of Nimbus 5 ESMR Data*, NASA TM X-70614, 1974, p. 21.
22. Schmugge, T. J., P. Gloersen, T. T. Wilheit, and F. Geiger, "Remote Sensing of Soil Moisture with Microwave Radiometers," *Journal of Geoph. Res.*, **79**, (2), 1974, pp. 317-323.
23. Meneely, J. M., *Application of the Nimbus 5 ESMR to Rainfall Detection over Land Surfaces*, Final Report E/S No. 1008, Earth Satellite Corp., Washington, D.C., 1975, p. 48.

24. Poe, G., A. Stogryn, and A. T. Edgerton, *Determination of Soil Moisture Content Using Microwave Radiometry*, Final Report No. 1684 FR-1 for Department of Commerce Contract No. 0-35239, 1971.
25. Oberste-Lehn, D., *Phenomena and Properties of Geologic Materials Affecting Microwaves-A Review*, Stanford Remote Sensing Laboratory, TR 70-10, Stanford University, Stanford, California, 1970, p. 57.
26. Cihlar, J. and F. T. Ulaby, *Dielectric Properties of Soils as a Function of Moisture Content*, RSL Tech. Report 177-47, University of Kansas Center for Research, Lawrence, Kansas, 1974, p. 61.
27. Vickers, R. S. and G. C. Rose, *The Use of Complex Dielectric Constant as a Diagnostic Tool for the Remote Sensing of Terrestrial Materials*, AFCRL-71-0438, Colorado State University, Fort Collins, Colorado, 1971, p. 39.
28. McCulloch, A. W., "The Temperature-Humidity Infrared Radiometer (THIR) Subsystem," *Nimbus 5 User's Guide*, ERTS/Nimbus Project, Goddard Space Flight Center, 1972, pp. 11-47.
29. Said, R., *The Geology of Egypt*, Elsevier Publishing Company, Amsterdam, New York, 1962, p. 377.
30. Issawi, B., "Nubia Sandstone: Type Section," *Geological Notes* (the American Association of Petroleum Geologists Bulletin), **57** (4), 1973, pp. 741-745.
31. El Shazly, E. M., M. A. Abdel-Hady, M. A. El Ghawaby, and I. A. Kassas, "Geologic Interpretation of ERTS-1 Satellite Images for West Aswan Area, Egypt," 9th International Symposium on Remote Sensing of Environment, Ann Arbor, Mich., 1974, pp. 119-131.
32. El Shazly, E. M., M. A. Abdel-Hady, M. A. El Ghawaby, and I. A. Kassas, "Geologic Interpretation of ERTS-1 Satellite Images for East Aswan Area, Egypt," 9th International Symposium on Remote Sensing of Environment, Ann Arbor, Michigan, 1974, pp. 105-117.
33. Ulaby, F. T., L. F. Dellwig, and T. J. Schmugge, *Satellite Microwave Observations of the Utah Great Salt Lake Desert*, NASA TM X-71000, 1975, p. 36.
34. Tanner, H., "Debate Flares in Egypt over Aswan Dam," *New York Times*, May 4, 1975.
35. Edgerton, A. T. and D. T. Trexler, *Passive Microwave Techniques Applied to Geologic Problems*, Final Report 1361-R-1, Aerojet-General Corporation, El Monte, California, 1970, p. 100.

36. Kennedy, J. M., A. T. Edgerton, R. T. Sakamoto, and R. M. Mandl, *Passive Microwave Measurements of Snow and Soil*, Technical Report 2, Aerojet-General Corporation, El Monte, California, 1966.
37. Edgerton, A. T., F. Ruskey, D. Williams, A. Stogryn, G. Poe, D. Meeks, and O. Russell, *Microwave Emission Characteristics of Natural Materials and the Environment*, Final Report 9016R-8, Aerojet-General Corporation, Azusa, California, 1973, p. 110.
38. Peake, W. H., "The Microwave Radiometer as a Remote Sensing Instrument with Applications to Geology," Notes prepared for a short course on Geologic Remote Sensing, Stanford University, Stanford, California, Dec. 4-8, 1967, p. 34.
39. Campbell, M. J. and J. Ulrichs, "Electrical Properties of Rocks and their Significance for Lunar Radar Observations," *Journal of Geophysical Research*, **74**, (25), 1969, pp. 5867-5881.
40. Peake, W. H. and T. L. Oliver, "The Response of Terrestrial Surfaces at Microwave Frequencies," Ohio State University, Columbus, Ohio, Electroscience Laboratory Report 2440-7, 1971, p. 255.
41. Clark, S. P. (ed.), *Handbook of Physical Constants*, Geological Society of America, Memoir 97, 1966.
42. Ingersoll, L. R., *Heat Conduction with Engineering, Geological and other Applications*, University of Wisconsin Press, Madison, Wisconsin, 1954, p. 325.
43. Pohn, H. A., T. W. Offield, and K. Watson, "Thermal Inertia Mapping from Satellite-Discrimination of Geologic Units in Oman," *Journal of Research*, U.S. Geological Survey, **2**, (2), 1974, pp. 147-158.
44. Watson, K., L. C. Rowan, and T. W. Offield, "Application of Thermal Modeling in the Geological Interpretation of IR Images," 7th International Symposium on Remote Sensing of Environment, Ann Arbor, Michigan, University of Michigan, **3**, 1971, pp. 2017-2041.
45. Rowan, L. C., T. W. Offield, K. Watson, P. J. Cannon, and R. D. Watson, "Thermal Infrared Investigations, Arbuckle Mountains, Oklahoma," *Geological Society of America Bulletin*, **81**, 1970, pp. 3549-3562.
46. Watson, K., "Geologic Applications of Thermal Infrared Images," *Proceedings of the IEEE*, 1975, pp. 128-137.
47. Kahle, A. B., A. R. Gillespie, A. F. H. Goetz, and J. D. Addington, "Thermal Inertia Mapping," 10th International Symposium on Remote Sensing of Environment, Ann Arbor, Michigan, 1975, pp. 1-17.

48. Moore, R. K. (ed.), L. L. Chastant, L. J. Porcello, J. Stevenson, and F. T. Ulaby, "Microwave Remote Sensors," *Manual of Remote Sensing*, 1 (9), F. Janza, (ed), American Society of Photogrammetry, Falls Church, Virginia, 1975, pp. 399-537.
49. Hanter, G., "Contribution to the Origin of the Nile Delta," Paper No. 117 (B-3), 9th Arab Petroleum Congress of the Secretariat General League of Arab States, 1975, p. 13.
50. Smith, S. R. (ed.), "Applications Explorer Missions (AEM)," *Mission Planners Handbook*, Goddard Space Flight Center, 1974, p. 160.
51. Otterman, J. and R. S. Frazer, *Earth-Atmosphere System and Surface Reflectivities in Arid Regions from Landsat Multispectral Scanner Measurements*, NASA TM X-71164, 1976, p. 38.
52. Dickinson, L. G., S. E. Boselly, and W. S. Burgmann, *Defense Meteorological Satellite Program (DMSP) User's Guide*, Headquarters Air Weather Service, Scott AFB, Illinois, 1974, p. 109.
53. Powers, R. W., L. F. Ramirez, C. D. Redmond, and E. L. Elberg, Jr., "Geology of the Arabian Peninsula, Sedimentary Geology of Saudi Arabia, U.S. Geological Survey Professional Paper 560-D, 1966, p. 147.
54. Blodget, H. W., *A Comparative Geologic Study of Spacecraft and Aircraft Imagery*, NASA TM X-65594, 1971, p. 56.
55. McCaslin, J. (ed.), *International Petroleum Encyclopedia*, The Petroleum Publishing Co., Tulsa, Oklahoma, 1975, p. 480.



228 001 C1 U E 770311 S00903DS
DEPT OF THE AIR FORCE
AF WEAPONS LABORATORY
ATTN: TECHNICAL LIBRARY (SUL)
KIRTLAND AFB NM 87117

POSTMASTER: If Undeliverable (Section 158
Postal Manual) Do Not Return

"The aeronautical and space activities of the United States shall be conducted so as to contribute . . . to the expansion of human knowledge of phenomena in the atmosphere and space. The Administration shall provide for the widest practicable and appropriate dissemination of information concerning its activities and the results thereof."

—NATIONAL AERONAUTICS AND SPACE ACT OF 1958

NASA SCIENTIFIC AND TECHNICAL PUBLICATIONS

TECHNICAL REPORTS: Scientific and technical information considered important, complete, and a lasting contribution to existing knowledge.

TECHNICAL NOTES: Information less broad in scope but nevertheless of importance as a contribution to existing knowledge.

TECHNICAL MEMORANDUMS: Information receiving limited distribution because of preliminary data, security classification, or other reasons. Also includes conference proceedings with either limited or unlimited distribution.

CONTRACTOR REPORTS: Scientific and technical information generated under a NASA contract or grant and considered an important contribution to existing knowledge.

TECHNICAL TRANSLATIONS: Information published in a foreign language considered to merit NASA distribution in English.

SPECIAL PUBLICATIONS: Information derived from or of value to NASA activities. Publications include final reports of major projects, monographs, data compilations, handbooks, sourcebooks, and special bibliographies.

TECHNOLOGY UTILIZATION PUBLICATIONS: Information on technology used by NASA that may be of particular interest in commercial and other non-aerospace applications. Publications include Tech Briefs, Technology Utilization Reports and Technology Surveys.

Details on the availability of these publications may be obtained from:

SCIENTIFIC AND TECHNICAL INFORMATION OFFICE

NATIONAL AERONAUTICS AND SPACE ADMINISTRATION

Washington, D.C. 20546